Scour hole formation for lateral non-uniform flow in non-cohesive sediments

by
Batuhan Üşenti

in partial fulfilment of the requirements for the degree of

Master of Science
in Civil Engineering

at the Delft University of Technology
To be defended publicly on the 28th of August, 2019 at 15:45h.

Student number:	4129431	
Date:	August, 2019	
Thesis committee:	Prof. dr. ir. W. S. J. Uijttewaal,	TU Delft
	Ir. Y. B. Broekema,	TU Delft
	Ir. M. Muttray,	TU Delft
	Ir. A. Zoon	Van Oord

TU Delft Delft University of Technology

Van Oord Marine ingenuity

Preface

This thesis is written as conclusion of the Master's programme of Hydraulic Engineering at the Delft University of Technology. The thesis is performed with the cooperation of Van Oord and it is supervised by the thesis committee both from Van Oord and the Delft University of Technology.

First of all, I would like to thank my thesis committee for their guidance, knowledge and feedback on this work. W. Uijttewaal for your limited time and involvement, M. Muttray for your feedback and experience and A. Zoon for your daily supervising, guidance and answers to my questions. Most of all, I want to thank my daily supervisor at the university Y. Broekema for guiding me throughout this master thesis. You were always available for help and you were always available for my questions. Your positive feedback, your knowledge and your input helped me to finish my thesis.

Next to my committee, I would like to thank Van Oord as a company for giving me the opportunity for this graduation. Special thanks go out to Greg Smith who helped me at first to graduate by Van Oord.

I would also like to thank all the technical staff of the Waterlab. They helped with from day one till the end with the experimental setup, measurement devices and cooperation. My gratitude goes out to Sander de Vree, Jaap van Duin, Arno Doorn, Pieter Van der Graag, Ruben and Frank Kalkman.

Finally, I would like to thank my parents, my sister, my brother and my friends for their unconditional support throughout this thesis. Their attendance motivated and helped me to finish my thesis.

Summary

For a project in the province of Zeeland, The Netherlands, a culvert was installed trough a dike to restore the tidal flow. Shortly after commissioning of the facility a scour hole at the end of the bottom protection developed. Although the scour hole was anticipated in the design, the scour hole was developing more rapidly than predicted. Furthermore, the hydrodynamics of the tidal jet flow from the culvert were different than what was expected in the design. It is expected that the uncertainties in predicting the scour hole process lies probably the most in a lack of understanding of the flow conditions in the vicinity of scour holes.

The scour hole depths can be predicted by the Breusers empirical relations. The development of the scour process entirely depends on the flow velocity and the relative turbulence intensity at the transition of the fixed to the erodible bed. The empirical equations do not account for all the hydrodynamic processes in a scour hole. Furthermore, the scour studies are predominantly considering a two-dimensional vertical situation in which lateral uniform flow is assumed. However, in practice lateral non-uniform flow is the rule rather than the exception.

The objective of this master thesis is to research the scour development under laterally nonuniform flow and to obtain more fundamental understanding of the scour process. Physical experiments were conducted in order to investigate the influence of lateral non-uniformities in the flow field on the scour process. In the scale experiments, the lateral velocity differences originated from two parallel streams with different streamwise velocities.

The scour pattern under laterally nonuniform flow is different than the scour pattern under laterally uniform flow. The scour hole in laterally nonuniform flow is deeper and it develops faster compared to the scour hole development in laterally uniform flow under the same hydraulic conditions. Furthermore, the scour pattern under lateral non-uniform flow shows spatial variations in lateral direction. The larger maximum scour depths are not observed in the zone with high flow velocities, but in the mixing layers.

A horizontal contraction of the flow at the scour hole is observed for lateral non-uniform incoming flow, whereas the presence of the scour hole does not affect the horizontal structure of the flow for lateral uniform incoming flow. The vertical structure of the flow showed relatively high near-bed velocities in the scour hole indicating flow attachment to the bed for laterally nonuniform flow. In addition, the vertical structure of the flow appears to become more depth uniform in the scour hole. The vertical structure of the flow is important of the sediment transport in the scour hole. For vertically attached flow, it was indicated that sediment could not be transported from the scour hole in the direction of the bed protection.

Contents

List of Figures

List of Tables

Nomenclature

Abbreviations

Abbreviation	Description
2DCS	Two-Dimensional Coherent Structure
ADV	Acoustic Doppler Velocimetry
BFS	Backward Facing Step
ES-SSB	Eastern Scheldt Storm Surge Barrier
RMSE	Root Mean Square Error
SLE	Shallow Lateral Expansion
SML	Shallow Mixing Layer
TKE	Turbulent Kinetic Energy
UF	Uniform Flow
NUF	Non-Uniform Flow

Greek symbols

Symbol	Description	Unit
α	1. Slope angle	$[°]$
	2. Flow and turbulence coefficient	$[-]$
β	Upstream scour slope	$[°]$
γ	Coefficient	$[-]$
δ	Boundary layer thickness	$[m]$
Δ	Relative density	$[-]$
ϵ	Turbulent (eddy) viscosity	$[m^2/s]$
κ	Von Kármán constant	$[-]$
μ	Dynamic viscosity	$[kg/ms]$
ν	Kinematic viscosity	$[m^2/s]$
ν_t	Turbulent (eddy) viscosity	$[m^2/s]$
ρ_s	Density of sediment	$[kg/m^3]$
ρ_w	Density of water	$[kg/m^3]$
τ_0	Mean bed shear stress	$[N/m^2]$
τ_c	Critical mean bed shear stress	$[N/m^2]$

τ_{xy}	Reynolds shear stress	$[N/m^2]$
ψ	Shields parameter	$-$
ω	1. Turbulence coefficient	$-$
	2. Vorticity	$[s^{-1}]$
Ω_p	Potential vorticity	$[s^{-1}]$

Roman symbols

Symbol	Description	Unit
A	Area of cross-section	$[m^2]$
A_c	Conveyance area	$[m^2]$
b	Width of shear layer or plane jet	$[m]$
b_u	Thickness of the jet	$[m]$
b_0	Half width of outflow in plane jet	$[m]$
B	Half width of outflow in plane jet	$[m]$
c_f	Friction coefficient	$[-]$
C	Chézy roughness coefficient	$[m^{0.5}/s]$
C_0	Coefficient	$[m^{0.5}/s]$
d	Grain diameter	$[m]$
d_{50}	Median grain diameter	$[m]$
D	Height of sill or dam	$[m]$
f	Planetary vorticity/Coriolis parameter	$[s^{-1}]$
f_c	Roughness function	$[-]$
Fr	Froude number	$[-]$
g	Acceleration of gravity	$[m/s^2]$
h	Water depth	$[m]$
h_s	Scour depth in time	$[m]$
h_{se}	Equilibrium scour depth	$[m]$
h_t	Tailwater depth	$[m]$
h_0	Initial water depth (water	$[m]$
i_b	Bed slope	$[-]$
K	Coefficient	$[m^{2.3}/s^{4.3}]$
k_s	Equivalent sand roughness (equivalent roughness of Nikuradse)	$[m]$

L	1. Characteristic length	$[m]$
	2. Length scale	$[m]$
	3. Length of the bed protection	$[m]$
p	Pressure	$[N/m^2]$
Q	Discharge	$[m^3/s]$
r	Relative turbulence intensity	$[-]$
$\bar{r}$	Depth-averaged relative turbulence intensity	$[-]$
R	Hydraulic radius	$[m]$
Re	Reynolds number	$[-]$
S	Sediment transport	$[m^3/s]$
t	Time	$[s]$
t_1	Characteristic time at which the maximum scour depth equals h_0	$[s]$
T	Turbulence period (averaging period)	$[s]$
u	Flow velocity in x-direction	$[m/s]$
$\bar{u}$	1. Flow velocity averaged in time	$[m/s]$
	2. Depth-averaged flow velocity	$[m/s]$
$\bar{\bar{u}}$	Flow velocity averaged in time and over the water depth	$[m/s]$
u_c	Critical flow velocity	$[m/s]$
$\bar{u}_c$	Critical depth-averaged flow velocity	$[m/s]$
u_m	Maximum flow velocity	$[m/s]$
u_0	Outflow velocity of jets	$[m/s]$
u'	Turbulent velocity fluctuation in x-direction	$[m/s]$
u_*	Shear velocity	$[m/s]$
$u_{*,c}$	Critical shear velocity	$[m/s]$
U	1. Flow velocity averaged in time	$[m/s]$
	2. Velocity scale	
v	Flow velocity in y-direction	$[m/s]$
v'	Turbulent velocity fluctuation in y-direction	$[m/s]$
w	Flow velocity in z-direction	$[m/s]$
w'	Turbulent velocity fluctuation in z-direction	$[m/s]$
x	Distance along horizontal axis (in flow direction)	$[m]$
y	Distance along horizontal axis (perpendicular to flow direction)	$[m]$
z	Distance along vertical axis	$[m]$

y_m	Maximum scour depth at time t	$[m]$
$y_{m,e}$	Maximum scour depth at equilibrium	$[m]$

Subscripts

b	Bed
c	Critical
e	Equilibrium
m	Model or maximum
p	Prototype
0	Initial

1 Introduction

1.1 Background information

A natural area was closed off from the Eastern Scheldt inlet in the past. Rijkswaterstaat wanted to improve the quality of the nature reserve and compensate for the erosion of the intertidal areas in the Eastern Scheldt inlet. An outlet structure or culvert was installed through a dike to return the tidal flow in this area and to allow the recovery of the intertidal areas in the Eastern Scheldt inlet.

Van Oord was commissioned for this project in the province of Zeeland. They designed the outlet structure and the bottom protection. This hydraulic structure was constructed and the project was completed in December 2014. Figure 1.1 gives an aerial image of the outlet structure and it shows the location of the project. The culvert consisted of three rectangular sections each $3.5\ m$ wide by $2.1\ m$ high. The culvert was connected to the bottom protection by a transition slope of $1{:}10$. The initial bottom protection was 24 m long and it consisted of $10-60\ kg$ rock at NAP $-2.0\ m$. Figure 1.2 shows a longitudinal-section of the initial design of the outlet structure including the bed protection of 24-meters-long. The bed material consisted of fine sand of $d_{50} = 130\ \mu m$.

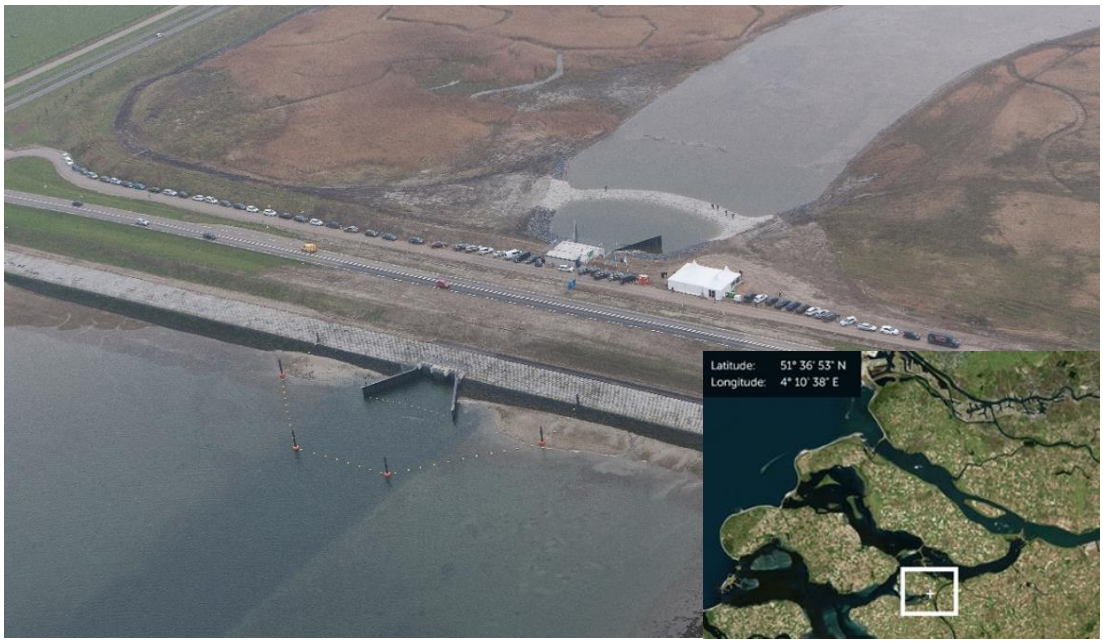

Figure 1.1: A aerial image of the outlet structure (left the Eastern Scheldt inlet and right the natural reserve) (Retrieved from Van Oord and https://www.satellietdataportaal.nl/).

Shortly after commissioning of the facility a scour hole at the end of the bottom protection developed. Although the scour hole was anticipated in the design, the development of the scour hole was more rapidly than predicted. Figure 1.3 gives the initial depth situation near the structure and Figure 1.4 gives the depth soundings after approximately two weeks. These and other depth measurements are found in Appendix A.

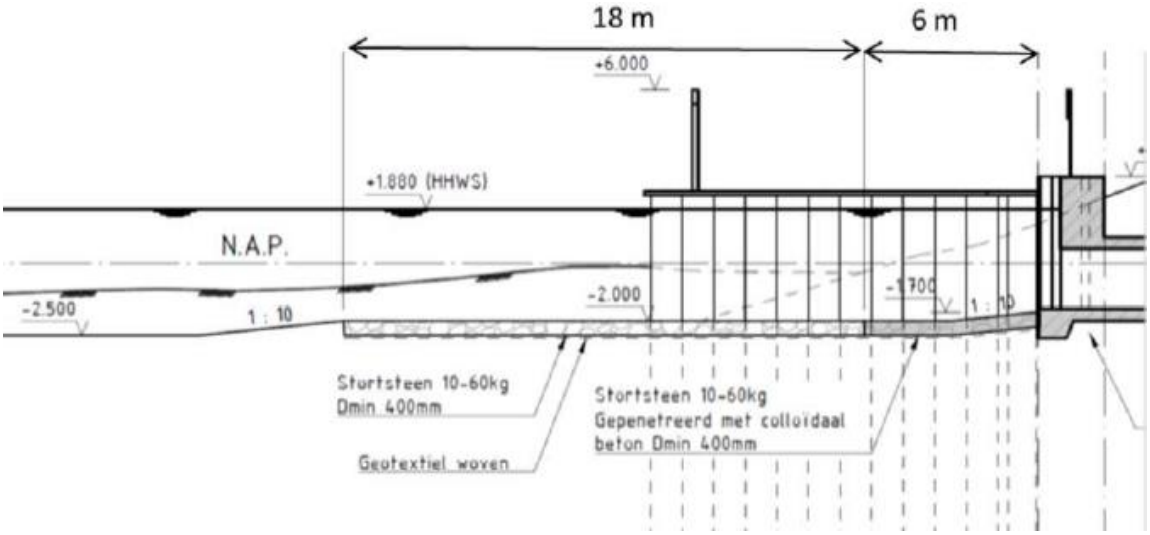

Figure 1.2: Longitudinal section of the outlet structure with a 24 m long bottom protection.

A scour hole of approximately $5\ m$ depth developed in a short period of 12 days, see Figure 1.4. The observed scour process could involve a potential risk to the structural stability of the hydraulic structure at the long term. To ensure the safety of the culvert the design was evaluated and the hydraulic structure and the bottom protection were redesigned.

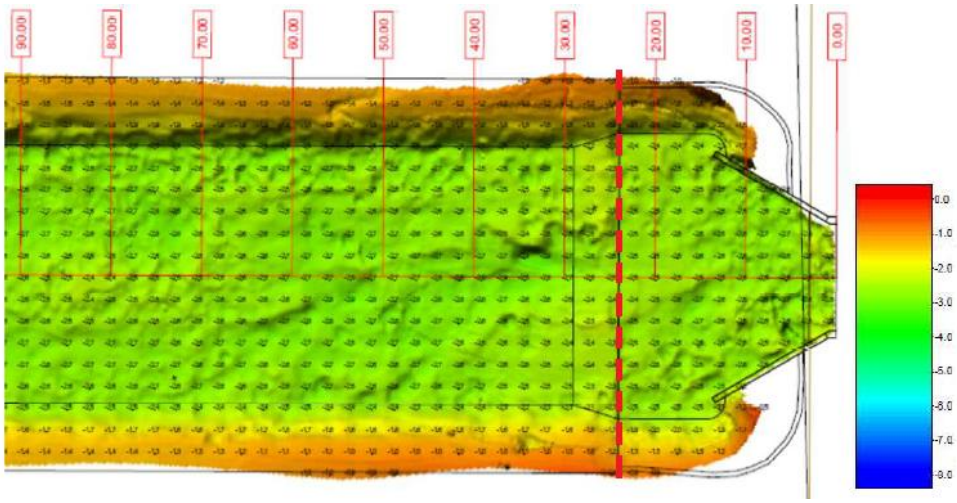

Figure 1.3: Initial bathymetry. The initial depth of the bed is approximately -2.5 m NAP. The red line indicates the edge of the bottom protection.

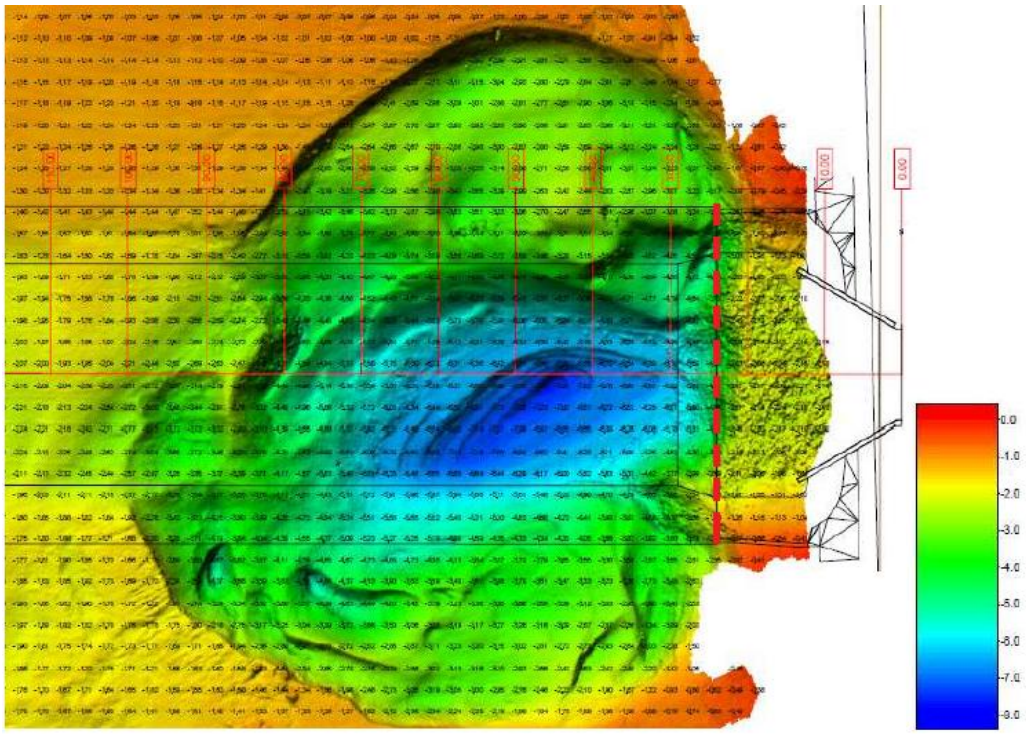

Figure 1.4: Bathymetry after 12 days with scour hole. The red line indicates the edge of the bottom protection. The maximum scour depth is approximately 5 m at a bed level around -7.5 m NAP.

The more rapidly development of the scour hole than initially predicted behind the bottom protection of the outlet structure indicates that the understanding of the scour process is still (partly) incomplete. Uncertainties in the predictions of the scour hole dimensions arise probably the most from a lack of understanding of the flow conditions. The observations of a different horizontal flow state during outflow of the culvert by Van Oord may strengthen the lack of knowledge concerning the flow conditions near a hydraulic structure in presence of a scour hole. An impression of the jet flow during ebb into the tidal inlet is shown in Figure 1.5. Van Oord observed that the jet flow downstream of the structure diverges less in the horizontal plane than what is known in common literature (Schiereck, 2012).

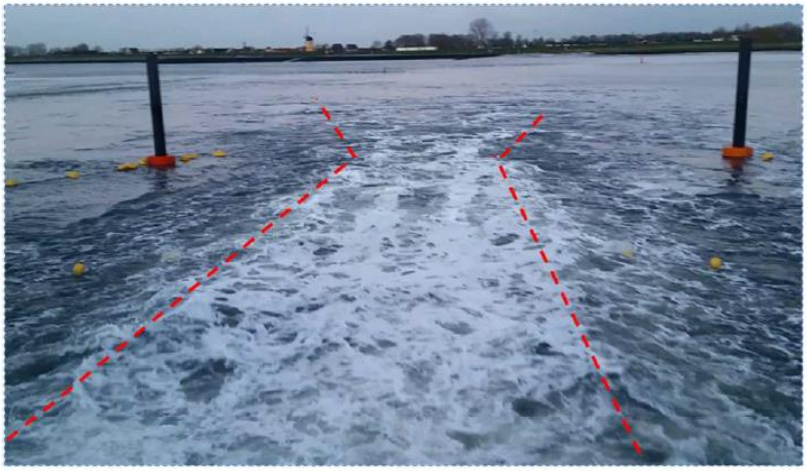

Figure 1.5: Photograph of the flow field downstream of the outlet structure. Jet during ebb flow into the tidal inlet. The jet flow is depicted in between the red dashed lines. The absence of foam in the region adjacent to the jet flow indicates a recirculation zone. The jet flow diverges behind the piles. The piles are located at 40 m from the culvert opening.

In literature (e.g., Hoffmans & Verheij, 1997), empirical equations have been suggested for predicting the scour hole dimensions. These empirical relations assume that the development of the scour process depends only on the flow velocity and turbulence intensity at the transition between fixed and erodible bed and do not account for the hydrodynamic processes in the scour hole (Hoffmans & Verheij, 1997). Furthermore, the scour studies predominantly consider a two-dimensional vertical situation in which the flow is assumed uniform in lateral direction (Hoffmans & Verheij, 1997).

The flow of the outlet structure can be classified as a tidal jet flow in which velocity differences are present along the width of the outlet structure. Broekema et al. (2018) have shown the importance of nonuniformity of the horizontal flow field in the scour process. Field observations near the storm surge barrier in the Eastern Scheldt estuary showed that the jet flow at the barrier contract towards the deepest part of the scour hole instead of spreading laterally and that a vertical recirculation zone on the upstream scour slope appeared periodically during a tidal cycle (Broekema et al., 2018). Flow velocity data in the scour hole have shown high near-bed flow velocities in the scour hole in case flow remains attached to the bed compared to moderate near-bed velocities in case of flow separation. The conducted physical experiments (Broekema, 2017; Van de Zande, 2018) to obtain more fundamental understanding of the flow patterns have shown that flow with lateral velocity differences contract at the location of the downward slope and when approaching a downward slope it can counteract vertical flow separation and suppress vertical recirculation zone on the downward slope.

The depth soundings behind the bottom protection of the outlet structure as depicted in Figure 1.4 shows a three-dimensional scour hole as a result of the presence of velocity differences along the width of the structure. The interaction of the horizontal and vertical flow states in laterally nonuniform flow may explain the more rapid scour development behind the bottom protection of the outlet structure. For a better understanding of the scour hole formation, improved insight in the flow patterns near and in scour holes are needed. The current empirical relations assume lateral uniform flow whereas in reality velocity differences in lateral direction can often not be neglected. Furthermore, the empirical formulations do not take into account the hydrodynamic processes whereas the observed flow patterns in three-dimensional scour holes under laterally nonuniform flow can be of importance in the scour hole process.

1.2 Problem definition

Due to a lack of fundamental knowledge behind scour hole formation, current predictions of the scour hole depths based on empirical formulations could be uncertain and inaccurate. The current empirical formulations do not account for all hydrodynamic processes in a scour hole. The flow pattern and the material transport in the scouring hole are not considered in the prediction of scour holes (Breusers, 1996). The development of the scour process depends entirely on the flow velocity and the relative turbulence intensity at the transition of the fixed to the erodible bed (Hoffmans & Verheij, 1997). Furthermore, these empirical relations predominantly assume lateral uniform flow for the approaching flow upstream of the scour hole. These scour studies have considered two-dimensional scour holes.

In many practical cases, however, velocity differences in lateral direction are present in the flow for example the tidal jet flow from the culvert in in which high velocities are in the center of the jet and low velocities are at the sides of the jet. These nonuniformities will cause three-dimensional scour holes. Recent observations and experiments have shown the importance of the nonuniformity in the horizontal flow in the scour process (Broekema, 2018; Van de Zande, 2018). For a better understanding of the development of three-dimensional scour holes more insight is needed in the fundamental hydrodynamic processes in the scour holes.

1.3 Research objective and research question

The objective of this master thesis is to obtain more fundamental understanding of three-dimensional scour hole development for laterally nonuniform flow. This thesis aims to investigate the effect of horizontal non-uniformities in the flow on the scour development behind a bed protection. The lateral velocity differences such as the tidal jet flow from the culvert may affect the scour hole development. Insight into the flow patterns in the scour hole could help for a better understanding of the scour phenomena and improve the current empirical equations that estimate scour near hydraulic structures. There is a value in finding the answer for the following main research question of this master thesis:

How may lateral non-uniform flow affect the scour hole development and what are the effects of this nonuniformity on the flow conditions in and near a scour hole?

The following sub questions are formulated:

1. How does the scour development in lateral non-uniform flow compare to the scour development in lateral uniform flow?

2. How does the presence of the scour hole affect the horizontal flow structure of the laterally nonuniform flow?

3. How does the presence of lateral nonuniformities in the flow field affect the vertical flow structure in the scour hole?

1.4 Methodology

In order to answer the main research question and the formulated sub-questions, first a review of the available literature on scour is presented. The current empirical relations for predicting the scour hole and a description of flow patterns in the two-dimensional scour hole is given. Second, the physical scale experiments are considered that are conducted in the Fluid Mechanics Laboratory at the Delft University of Technology.

The aim of the physical experiments is to obtain more detailed information on the scour hole formation under lateral nonuniform flow. Insight into the flow patterns in the three-dimensional scour hole could help to better understand the three-dimensional scour development and the influence of lateral non-uniformities in the flow field on the scour process. The planned experiments are a follow-up on previous experiments by Broekema et al. (2018) and Van de Zande (2018).

1.5 Report outline

Chapter 2 addresses the available literature on the scour phenomena. The current empirical formulations and the description of flow patterns in scour holes are presented. In addition, relevant literature about horizontal shear flows or laterally nonuniform flows and a short introduction on vertical flow separation is discussed. The chapter ends with a summary of the given literature study. Chapter 3 contains the experimental setup, the scaling and parameters space, the experimental cases and the used measurement techniques. Chapter 4 gives the results of the experiments. The obtained results are discussed in Chapter 5. The conclusions and recommendations for further research are given in Chapter 6.

2 Literature study

In this chapter, a review of the available literature and previous studies concerning scouring is given. Section 2.1 describes scour in general terms. Section 2.2 presents the theory behind scouring in the scope of previous studies. This section provides empirical relations to predict the scour hole. Section 2.3 discusses the flow patterns in two-dimensional and three-dimensional scour holes. The horizontal shear flows are considered in section 2.4, whereas the flow separation is treated in section 2.5. Section 2.6 summarizes the literature study.

2.1 Introduction

In general, local erosion or scour is a special case of sediment transport. Scour is the result of the difference in sediment transport and occurs when the local transport exceeds the supply from upstream. The difference in sediment transport can be due to a difference in velocity and/or turbulence. The general expression for mass conservation of sediment reads (Schiereck, 2012):

$$\frac{\partial z_b}{\partial t} + \frac{\partial S}{\partial x} = 0 \qquad (2.1)$$

in which: $z_b = position\ of\ the\ bed\ [m]$

$S = total\ sediment\ tranpsort\ per\ unit\ width\ [m^2/s]$

Figure 2.1 presents a general picture of local erosion or scour. Scouring is the lowering of the sea or river-bed as a result of non-equilibrium sediment transport conditions. Two possible cases for local scour are described in Schiereck (2012).

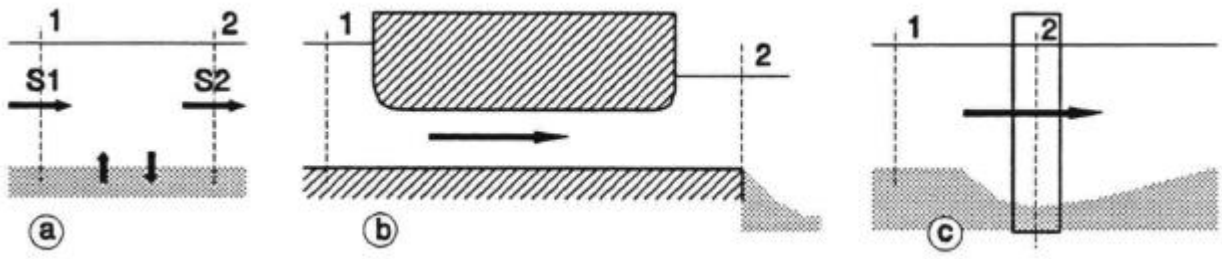

Figure 2.1: General picture of scour. (a) $S_2 = S_1 > 0$, dynamic equilibrium situation. (b) $S_2 > S_1 = 0$, non-equilibrium sediment transport. No sediment supply from upstream and scour in section 2. (c) $S_2 > S_1 > 0$, non-equilibrium in sediment transport. The erosion capacity is larger than the supply of sediment from upstream that results in a scour hole.

Clear-water scour. There is no sediment supply from upstream, while there is sediment transport downstream. Clear-water scour can result either from lack of transport capacity (the bed material in the natural flow is at rest) or from lack of erodible material upstream (the bed upstream of the scour hole is fixed).

Live-bed scour. Sediment supply from upstream is present but the sediment transport downstream is larger. The prediction of local scour plays an important role in the design of hydraulic structures. Excessive local scour can undermine the foundation and lead to the failure of the hydraulic structure. In general, the bed in the direct neighborhood of hydraulic structures is protected. Preventing scour is practically impossible. The main function of protections behind hydraulic structures is to keep the scour hole as far away as possible from the structure. It is stressed that the scour itself is not the problem, its threat to the stability of a structure is important.

The outflow of the culvert is protected by a bottom protection in order to keep the scour hole as far away as possible. Therefore, this research is focused on clear-water scour as the upstream bed is fixed and no sediment is supplied from upstream. Before section 2.2 will addresses the scour process in more detail, a short description on the initiation of motion for non-cohesive sediments is presented in order to complete this general introduction to scour.

Initiation of motion

Sediment transport is present as result of interaction between water and sediment. The initiation of motion of non-cohesive sediments in uniform flow is described by Schields (Schiereck, 2012). Movement of sediment depends on the ratio between force on grains and resistance of grains. The grain becomes unstable if the instantaneous bed shear stress exceeds the critical bed shear stress. As a result of the random shape, weight, placement and other aspects of the individual grains, a broad belt was drawn for the initiation of motion of grains as can be seen in Figure 2.2.

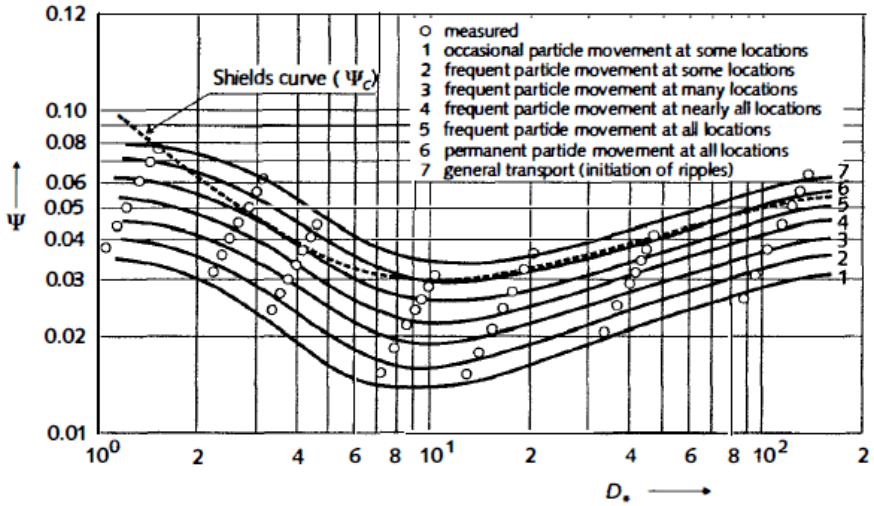

Figure 2.2: Modified Shields diagram (Hoffmans and Verheij, 1997).

Figure 2.2 gives the Shields graph together with the results of the investigation into the threshold of motion by Delft Hydraulics (1969) at which the grains start to move. The bed movement is divided into 7 stages. In many scour predictions a critical velocity is applied as the velocity for particle movement. This critical mean flow velocity is given by Hoffmans & Verheij (1997) and it reads:

$$\bar{u}_c = 2.5\sqrt{\Delta \Psi_c g d_{50}}\, ln\left(\frac{12h}{k_s}\right) \quad (2.2)$$

in which: $\bar{u}_c = critical\ mean\ flow\ velocity\ [m/s]$

$\Delta = relative\ density$

$\Psi_c = critical\ Shields\ parameter$

$g = gravitional\ acceleration\ [g = 9.81\, m/s^2]$

$d_{50} = median\ grain\ size\ [\mu m]$

$h = flow\ depth\ [m]$

$k_s = equivalent\ (effective)\ sand\ roughness\ [m]$

2.2 Scour holes

2.2.1 Scour development

The problem of local scour due to structures has got much attention in the past mostly as a consequence of the occurrence of severe damage (Breusers, 1966). Furthermore, the expected severe scour in the vicinity of the hydraulic structures of the Delta Works necessitated a better understanding of the scour process in particular. As a result, in the 1960s a systematical research (Delft Hydraulics, 1976) on local scour started in the Netherlands at Delft Hydraulics within the scope of the Delta Works.

Hoffmans and Verheij (1997) outlined the most important research on scour during recent decades. Although understanding of the underlying processes and the modelling of scour have made much progress in recent years, many scour problems are still not fully understood (Hoffmans & Verheij, 1997). Further research is needed in order to be able to describe the scour process in more detail and to optimize the design of hydraulic structures.Hydraulic structures cause disturbances in uniform flow, the flow will accelerate and decelerate. The increased flow rate and turbulence intensity downstream of a hydraulic structure result in an increase in the sediment transport. Consequently, a scour hole will develop downstream. A schematization of the scour process is shown in Figure 2.3 (De Graauw, 1981).

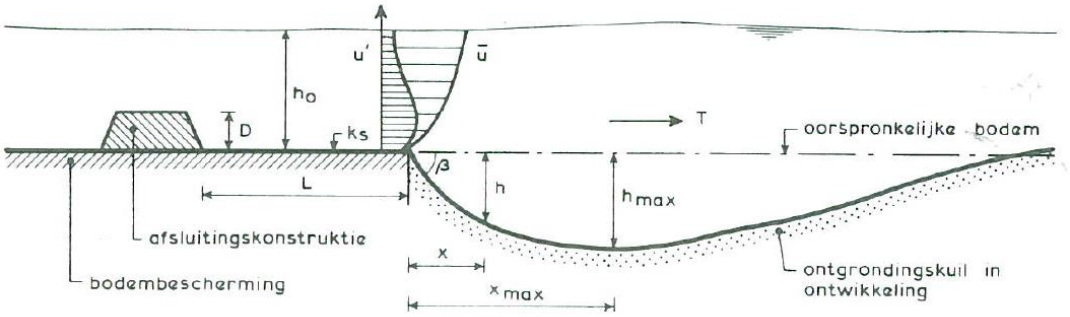

Figure 2.3: Schematization of the scour hole downstream of a structure and bottom protection (De Graauw, 1981).

Parameters of interest in the design of hydraulic structures and bed protections concerning a scour hole are the main dimensions of the scour hole and the rate of scouring. The main dimensions of the scour hole can be characterized roughly by the maximum scour depth y_m or h_{max} and by the upstream scour slope β. Figure 2.4 presents the schematization of a scour hole.

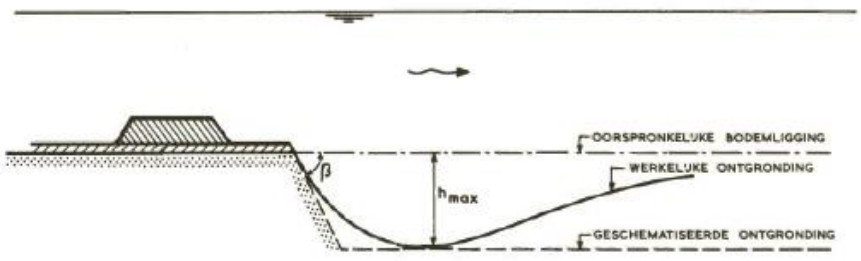

Figure 2.4: Schematization of scour hole with the maximum scour depth and upstream scour lope (Delft Hydraulics, 1976). Here, the maximum scour depth is indicated by h_{max}.

The formation of a scour hole takes time. The size and the shape of the scour hole are time dependent. The scour process is in the beginning very fast, in a later phase the progress is slower and eventually an equilibrium situation will be reached. Figure 2.5 presents the scour development in time.

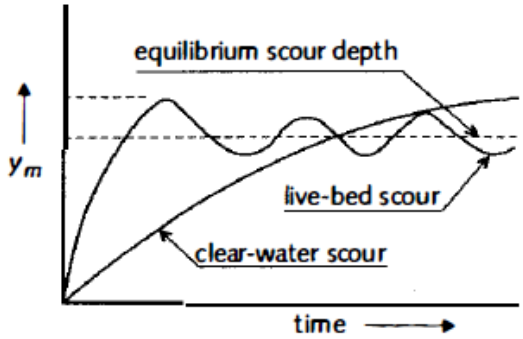

Figure 2.5: Scour depth as function of time (Hoffmans & Verheij, 1997).

Zanke (1978) differentiated four phases in the evolution of a scour hole based on clear-water scour experiments (Breusers, 1966; Dietz, 1969): an initial phase, a development phase, a stabilization phase, and an equilibrium phase (Hoffmans & Verheij, 1997). Figure 2.5 shows the development of the scour process in time with the four phases. Zanke (1978) distinguished four phases in the scouring process that is given below (Hoffmans &Verheij, 1997):

- Initial phase: This phase is the beginning of the scour hole development. The flow in the scour hole is nearly uniform over the approximately horizontal initial bed. A certain amount of bed material near the potential upstream slope goes into suspension and the scour hole starts to develop. The initial phase is the phase in which the erosion capacity of the scour process is the most severe.
- Development phase: The scour depth increases considerably and the shape of the scour hole remains the same during this phase. The ratio maximum scour depth and distance from the end of the bed to the point of maximum scour depth is more or less constant. The upper part of the upstream scour slope is in equilibrium, whereas the lower part is developing.
- Stabilization phase: The rate of development of the maximum scour depth decreases. The erosion capacity is very small at the maximum scour depth compared to capacity downstream of the point of reattachment. As a result, the dimensions of the scour hole increase more in stream wise direction than in the vertical direction. The maximum scour depth and the upstream scour slope are almost in equilibrium.
- Equilibrium phase: The dimensions of the scour hole do not change significantly. The maximum scour depth has approached a limit.

2.2.2 Empirical scour relations

For a description of the scouring process many laboratory experiments have been performed (e.g., Breusers, 1966; Delft Hydraulics 1976, 1979, Dietz, 1979). Some semi-empirical relations were obtained that describe the scour process in time (e.g., Breusers 1966). According to Breusers (1966), the development of the scour process depends on the flow velocity and turbulence intensity at the transition between fixed and the erodible bed. The Breusers method limits the prediction of the scour process to one computation and no information is needed concerning the near bed velocities and bed turbulence in the scour hole (Hoffmans & Verheij, 1997).

From the results and observations of several hundreds of experiments on local scour in loose sediments a relation of the scouring process as function of time and relations between the time-scale and scales for velocity, flow depth and material density were found (Hoffmans & Verheij, 1997).The scour depth as function of time can be predicted by the so-called Breusers-equilibrium method. This Breusers-equilibrium method can be considered as an expansion of the work of Breusers (1966) and it can be applied for all situations where local scour is expected (Hoffmans & Verheij, 1997). The scour process as function of time can be given with reasonable accuracy by the Breusers-equilibrium relation (Hoffmans & Verheij, 1997):

$$\frac{y_m}{y_{m,e}} = 1 - e^{ln\left(1-\frac{h_0}{y_{m,e}}\right)\left(\frac{t}{t_1}\right)^{\gamma}} \tag{2.3}$$

in which: $y_m = maximum\ scour\ depth$

$y_{m,e} = equilibrium\ scour\ depth$

$h_0 = initial\ waterdepth$

$t = time$

$t_1 = characteristic\ time\ of\ the\ scouring\ process\ in\ which\ h_{max} = h_0$

$\gamma = coefficient$

This Breusers-equilibrium relation describes the maximum scour depth as function of time including the equilibrium scour depth provided that that the equilibrium scour depth $y_{m,e}$ is greater than the initial flow depth h_0. The natural logarithm function in the Breusers-equilibrium relation is undefined for equilibrium scour depth $y_{m,e}$ smaller than the initial flow depth h_0. In the development phase of the scour process (i.e. $t < t_1$), the Breusers-equilibrium scour relation can be reduced to the original Breusers time-dependent expression (Hoffmans, & Verheij, 1997):

$$\frac{y_m}{h_0} = (\frac{t}{t_1})^{\gamma} \tag{2.4}$$

Breusers (1966) reported that for 2D scour the averaged value of the coefficient γ measured about 0.38 based on an extensive analysis at which the maximum scour depth was about $0.5 \cdot h_0$. Others have also done research on the coefficient γ. Table 2-1 shows the different studies and the different values of the coefficient γ (Hoffmans & Verheij, 1997). The value obtained by Breusers seems to be confirmed by the

other 2D cases, since the averaged value of $\gamma = 0.38$ lies within the range of $\gamma = 0.27 - 0.40$. Table 2-1 shows also that for 3D flow conditions, a higher value of coefficient γ should be used.

Investigator	γ	Flow condition
Breusers (1966)	0.38	Two-dimensional
Mosonyi & Schoppmann (1968)	0.27-0.35	Two-dimensional
Dietz (1969)	0.34-0.40	Two-dimensional
van der Meulen & Vinjé (1975)	0.4-0.8	Three-dimensional

Table 2-1: Coefficient γ (Hoffmans & Verheij, 1997).

The time scale of the scouring process is important as the scour process develops in time. The time at which the scour depth equals the initial flow depth is t_1. The dependence of the characteristic time on the hydraulic conditions and material characteristics has been investigated by several researchers (Breusers 1966, 1967; Dietz, 1969; van der Meulen & Vinjé, 1975). An expression for the characteristic time for steady flow derived from the model tests can be found in Hoffmans & Verheij (1997) and it reads:

$$t_1 = \frac{K \cdot {h_0}^2 \cdot \Delta^{1.7}}{(\alpha \bar{u} - \bar{u}_c)^{4.3}} \tag{2.5}$$

in which: $t_1 = characteristic\ time$

$K = coefficient$

$h_0 = initial\ waterdepth$

$\Delta = relative\ density$

$\alpha = flow\ and\ turbulence\ coefficient$

$\bar{u} = depth - averaged\ flow\ velocity$

$\bar{u}_c = critical\ mean\ flow\ velocity$

Three-dimensional scour

The characteristic time relation is equally applicable to two-dimensional scour as for three-dimensional scour (Hoffmans & Verheij, 1997, p.47). For three-dimensional scour however, the characteristic time is not constant at each cross-section. The three-dimensional scour hole development is determined by many longitudinal sections separately. The reader is referred to the work of Hoffmans & Verheij (1997) and Van der Meulen & Vinjé (1975) for more information on the characteristic time.

Van der Meulen & Vinjé (1975) have performed a systematic research on three-dimensional local scour in loose sediments. Van der Meulen & Vinjé (1975) have executed tests with a horizontal constriction in the flow introducing three-dimensional scour. The tests have been carried out in different geometries with a fixed abutment length of $b = 0.1\ B$ and variations in dam-height of $D/h_0 = 0.0, 0.3$ and 0.6. Both Figure 2.6 and Figure 2.7 show the three-dimensional scour test.

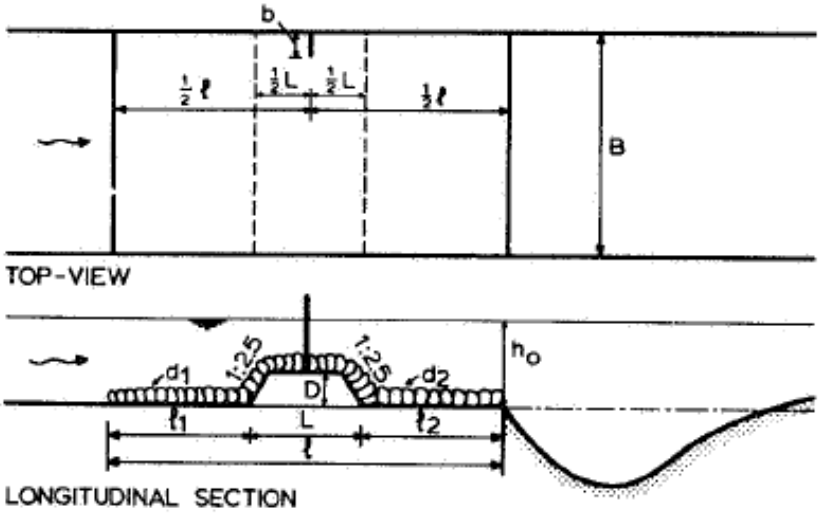

Figure 2.6: Top-view and longitudinal section of the three-dimensional test (Van der Meulen & Vinjé, 1975).

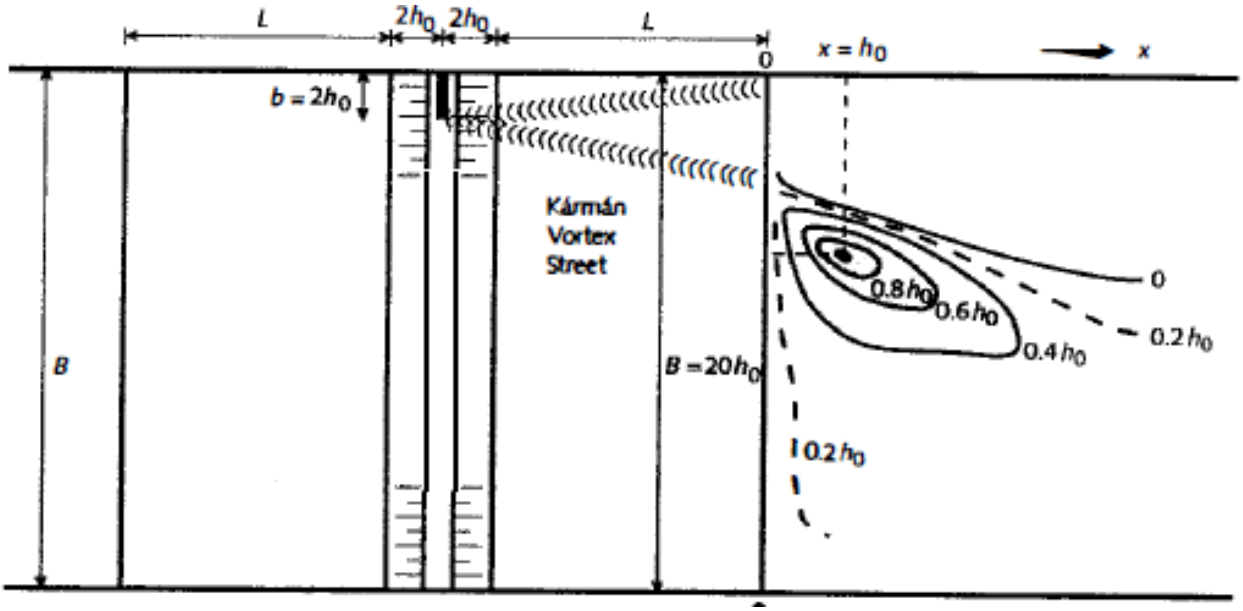

Figure 2.7: Three-dimensional scour test result of Van der Meulen & Vinjé (1975) (Hoffmans & Verheij, 1997).

Figure 2.8 presents the results of the tests form the systematic research of van der Meulen & Vinjé (1975) as a function of y_m/h_0 versus t/t_1 for the deepest point of the scour hole in the cross-section.

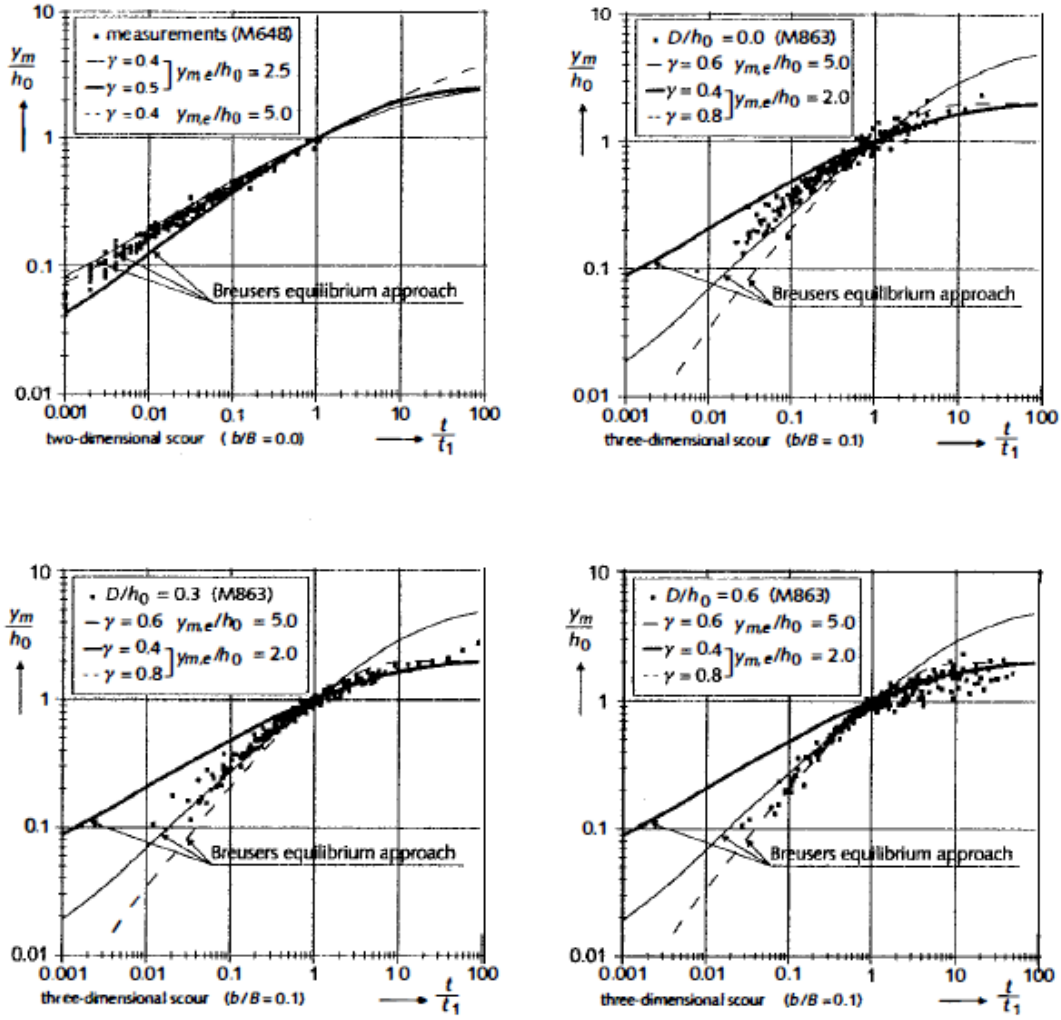

Figure 2.8: Maximum scour depth as function of time.

For two-dimensional scour the coefficient γ is measured to be approximately 0.38. However, for three-dimensional scour this coefficient γ required for the prediction of the maximum scour depth as function of time is dependent on the geometry (Hoffmans & Verheij, 1997). Figure 2.8 shows the range of values of the coefficient γ determined by these experiments. The experimental results of the three-dimensional local scour could be predicted with reasonable accuracy by the Breusers-equilibrium approach given that the equilibrium scour depth $(y_{m,e})$ is greater than the initial flow depth (h_0) and the coefficient $\gamma = 0.4 - 0.8$.

The characteristic time relation shows the influence of the various parameters on the scour process. The influence of the bed material is expressed in Δ and u_c, the influence of the water depth in h_0 and the influence of the flow in $\alpha\bar{u}$. The coefficient α is an amplification factor for the flow velocity and it is introduced to parameterize the impact of turbulence. The magnitude of the flow and turbulence coefficient α depends largely upon the upstream geometry. The reader is referred to Appendix B.2.1 for more insight into the flow and turbulence coefficient α. Appendix B.2.1 will present the influence of the definition of α and the important role of the length and roughness of the bed protection in determining this flow and turbulence coefficient α.

Several empirical expressions for α have been derived from two- and three-dimensional scour tests. A general relation for the local turbulence coefficient is given by Hoffmans & Booij (1993a). The three-dimensional scour process can be determined at any cross-section, provided that the local turbulence coefficient α and the local depth-averaged velocity $\bar{\bar{u}}$ are known.

$$\alpha_l = 1.5 + 4.4\,\bar{r}_0\,f_C; \tag{2.6}$$

where: $\bar{r}_0 = relative\ depth - averaged\ turbulence\ intensity$

$f_C = friction\ coefficient;\ f_C = \dfrac{C}{40}$

The empirical scour relations have mainly been based on the results and observations of physical model tests considering steady flow and no upstream sediment supply. The conditions of non-steady flow, such as tidal flow and the influence of upstream sediment supply can be taken into account with additional computations. The reader is referred to Appendix B.2 to see the extended equations to unsteady-flow conditions and the influence of upstream supply of sediment on the scour hole development.

Equilibrium scour

For most engineering situations, the equilibrium scour depth of a scour hole is the most important scour parameter (Hoffmans & Verheij, 1997). For permanent structures the equilibrium scour depth is relevant. The maximum scour depth approaches a limit during the life time of hydraulic structures. To obtain equilibrium conditions, a relatively long period of time is needed. In scale models the equilibrium situation was not always achieved, especially for experiments of low Froude numbers and clear-water scour (Delft Hydraulics, 1972). However, Dietz (1969) observed a tendency towards equilibrium in some of the tests. Dietz (1969) performed extensive research on two-dimensional scour downstream horizontal beds and low sills. Dietz (1969) derived the equilibrium scour based on experiments depth with no sediment from upstream and it is given by:

$$\frac{y_{m,e}}{h_0} = \frac{\omega\bar{u}_0 - \bar{u}_c}{\bar{u}_c} \tag{2.7}$$

in which: $\bar{u}_0 = depth - averaged\ flow\ velocity\ \ [m/s]$

$\bar{u}_c = critical\ mean\ flow\ velocity\ [m/s]$

$\omega = 1 + 3r_0$

Schiereck (2012) proposed an equivalent equilibrium scour depth relation, see Equation 2.7, in which the flow and turbulence factor α is used. According to Schiereck (2012), the equilibrium scour depth in the case of clear water is reached when the velocity in the scour hole multiplied by the flow and turbulence factor α is equal to the critical velocity $\bar{u}_c$. This will overestimate the equilibrium depth, because α is not defined in the hole but at the edge of the protection and it is not valid for the equilibrium phase. In practice, the value of the multiplication factor for the velocity is reduced by a factor of about 0.5 based on experiments (Schiereck, 2012). Figure 2.9 presents the schematization of the scour hole in predicting the equilibrium depth.

$$\frac{h_{se}}{h_0} = \frac{0.5\alpha\bar{u} - \bar{u}_c}{\bar{u}_c} \tag{2.8}$$

in which: $\alpha = turbulence\ factor\ [-]$

$\bar{u} = upstream\ depth - averaged\ flow\ velocity\ [m/s]$

$\bar{u}_c = critical\ flow\ velocity\ [m/s]$

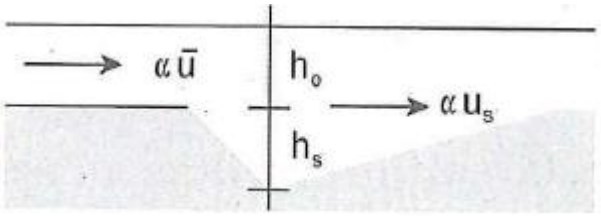

Figure 2.9: Schematization of scour hole for the computation (Schiereck, 2012).

Hoffmans (2012) analyzed the relation of the equilibrium scour depth again. Hoffmans' scour approach is based on the momentum equation. The scour hole is represented as a control volume with forces acting on it, see Figure 2.10. In the equilibrium phase the sum of forces acting on the control volume equals zero (Hoffmans, 2012).

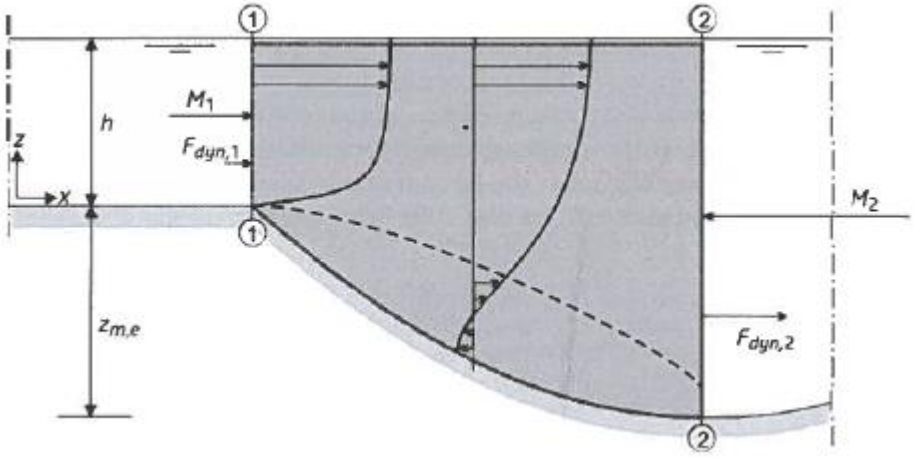

Figure 2.10: Forces acting on a control volume in a scour hole in the equilibrium phase. M_1 and M_2 are momentum fluxes at inflow and outflow section. $F_{dyn,1}$ and $F_{dyn,2}$ are dynamic forces at inflow and outflow section (Hoffmans, 2012).

$$\frac{z_{m,e}}{h_0} = \chi_e \cdot \left(\frac{U_0}{U_c}\right)^2 - 1 \qquad (2.9)$$

with:

$$\chi_e = \frac{1 + a_\chi {r_0}^2}{1 - a_\chi {r_{0,m}}^2}$$

in which: $z_{m,e} = equilibrium\ scour\ depth$

$h_0 = initial\ water\ depth\ [m]$

$U_c = critical\ depth - averaged\ flow\ velocity$

$U_0 = depth - averaged\ flow\ velocity$

$\chi_e = coefficient\ [-]$

$a_\chi = coefficient = 6.3\ [-]$

$r_0 = depth - averaged\ relative\ turbulence\ intensity$

$r_{0,m} = depth - averaged\ relative\ turbulence\ in\ maximum\ scour\ depth$

2.3 Flow patterns in scour holes

This section gives a description of the flow patterns in scour holes. For a better understanding of the scour process, insight in the hydrodynamic conditions in the scour hole is required. First, the flow patterns in two-dimensional scour holes is treated. It contains the analogy between the flow patterns downstream of a sill and in a scour hole (Hoffmans & Verheij, 1997). Second, the flow patterns in three-dimensional scour holes are discussed. This section addresses previous research on the flow structures inside scour holes with a three-dimensional geometry subjected to uniform flow (Koopmans, 2017; Stenfert, 2017) as well as the recent research on flow patterns by Broekema et al. (2018) and Van de Zande (2018).

2.3.1 Flow patterns in two-dimensional scour holes

Figure 2.11 present the flow patterns behind a sill. The deceleration of the flow due to a sudden increase in depth in the flow direction results in flow separation. The separated flow creates a vertical recirculation zone in which a reverse flow develops opposite to the main flow direction. As velocity gradients are present over the depth, a mixing layer is created. In both mixing layer and the recirculation zone, high turbulent intensities are present (Schiereck, 2012). Downstream form the point of reattachment point, a new-wall boundary develops and spreads into the relaxations zone.

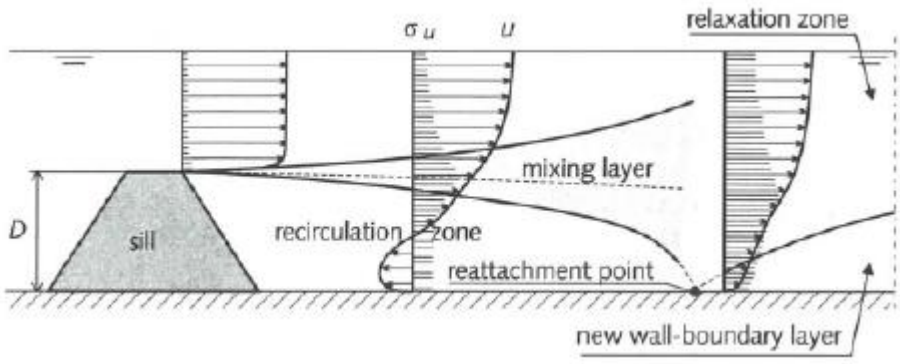

Figure 2.11: Schematization of flow zones behind sill (Hoffmans & Verheij, 1997).

Just behind the bottom protection, the flow will decelerate as a result of a sudden increase in depth in the flow direction. The forming of a scour hole will cause disturbances in the uniform flow. The flow in a scour hole is assumed to be more or less two-dimensional and it has a similar form as the flow pattern downstream of a hydraulic structure. It appears that the separated shear layer both in the scour hole as downstream of a hydraulic structure is similar to a simple plane mixing layer (Hoffmans & Verheij, 1997). Figure 2.12 shows the flow patterns in a two-dimensional scour hole. In analogy with the flow patterns behind a sill, Hoffmans (1992) have characterized the following flow zones in two-dimensional scour holes: a transient flow zone, a mixing layer, a recirculation zone, a relaxation zone and a new wall-boundary layer.

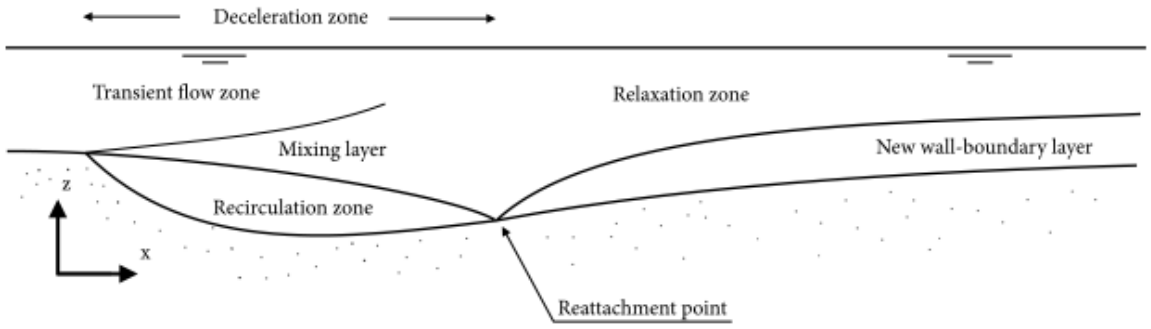

Figure 2.12: Schematization of the flow regions in a scour hole (Hoffmans, 1992).

Guan, Melville and Friedrich (2014) also performed an important study on the underlying flow patterns and turbulence structures in the scour hole. This study presents the results of an experimental study of flow patterns, bed shear stresses, and turbulence structures in the approach flow towards a submerged weir and in the resulting scour hole. Figure 2.13 shows the flow field in the equilibrium scour hole along the flume centerline in the longitudinal direction. The sudden change in the bed (scour hole) results in the separation of the boundary layer from the upstream slope of the scour hole. Important here are the recirculation zone and a flow reattachment region on the upstream scour slope. The maximum scour depth point is near the end of the reattachment region. Further downstream, the uniform flow is redeveloping again.

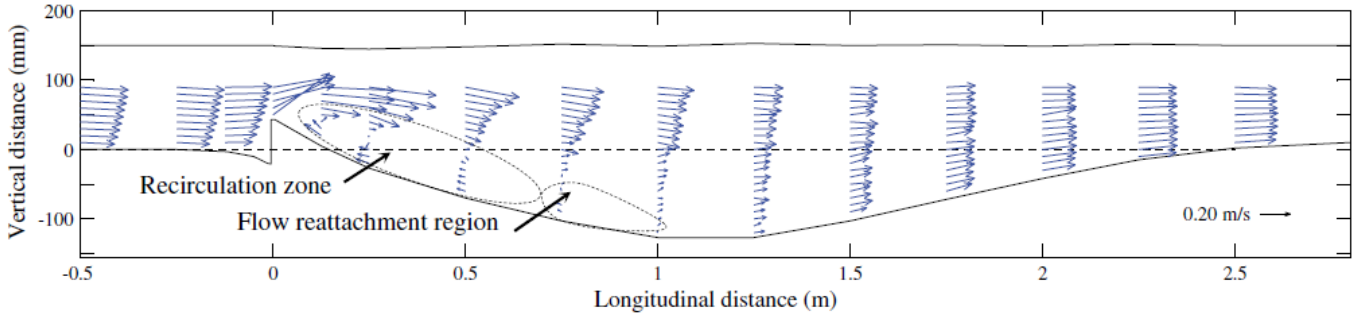

Figure 2.13: Velocity vector distribution in the centerline longitudinal section (Guan et al., 2014).

2.3.2 Flow patterns in three-dimensional scour holes

The flow pattern in three-dimensional scour holes can be characterized as more complex. How flow structures inside a scour hole contribute to the development of a three-dimensional scour hole geometry has been investigated in the past few years (Koopmans, 2017; Stenfert, 2017). The observed scour holes in the river bed the Rhine-Meuse delta were the motivation for research on the scour hole formation in heterogenous subsoil (Van Zuylen 2015; Koopmans, 2017; Stenfert, 2017, Blom, 2017). To improve knowledge on scour hole formation in heterogenous subsoil field data analysis, numerical simulation (Blom, 2017) and physical scale model experiments (Van Zuylen, 2015; Koopmans, 2017; Stenfert, 2017) are performed.

The investigated physical model tests (Koopmans, 2017; Stenfert, 2017) simulated the influence of a poorly erodible top layer on the scour development by exposing sand through an oval shaped opening in a concrete top layer. Figure 2.14 illustrates the experimental set-up of Stenfert (2017) as an example.

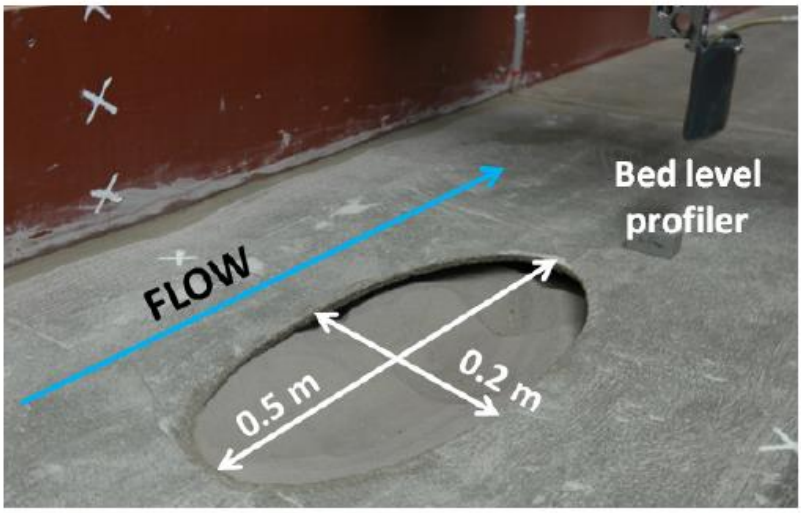

Figure 2.14: Physical experiments with a three-dimensional fixed scour hole geometry with a concrete top layer (Koopmans, 2017).

The experimental study by Uijttewaal et al. (2016), Koopmans (2017) and Stenfert (2017) concluded that three-dimensional scour geometry results in a deeper and faster growing scour hole compared to a two-dimensional scour hole geometry as experimentally observed by Van Zuylen (2015). From the work of Uijttewaal et al. (2016), Koopmans (2017), Stenfert (2017) and Bom (2017) several hydrodynamic processes that could play a role in the development of three-dimensional scour holes are considered. These hydrodynamic processes can be summarized as follows and are qualitatively depicted in Figure 2.15:

1. Recirculation zone on the upstream scour slope. All studies describe a recirculation zone at the upstream scour slope similar to the recirculation zone in two-dimensional scour holes. The size of the recirculation zone varies in time and in space according to Stenfert (2017).

2. Horse shoe shaped vortex. The flow starts to separate just downstream of the poorly erodible top layer. As a result of the three-dimensional geometry of the scour hole, a horse shoe shaped vortex develops (Figure 2.15). This vortex has a small transverse component to the center of the scour hole. The developed horse shoe shaped vortex contributes to the convergence of the streamlines.

This convergent flow towards the center of the scour hole most likely causes higher flow velocities towards the bed in the center of the scour hole. The vortex disintegrates into a less structures wake further downstream (Uijttewaal et al. 2016).

3. Contraction of the flow. The deepest point in the center of the scour hole is observed in the area of the converged flow. The contraction of the flow in the scour hole may be explained by two possible explanations (Blom, 2017): The streamlines converge as a result of the larger local discharge in the area above the scour hole by a redistribution of the momentum at the scour hole. Another possible explanation for the converging streamlines is given by the principle of conservation of the potential vorticity. Appendix B.1.6 gives more detail about this principle.

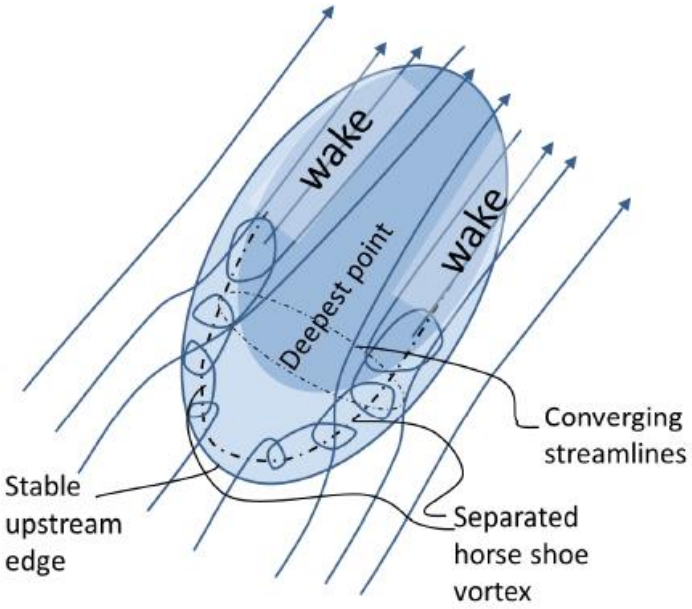

Figure 2.15: Qualitative sketch of the flow patterns in a three-dimensional scour geometry. The horseshoe shaped vortex, the converging of the streamlines and the deepest point in the area of the converged flow is depicted for an oval shaped hole (Uijttewaal et al. 2016).

It is important to note that the above studies the scour holes were subjected to a lateral uniform incoming flow. The three-dimensional scour hole development and the flow patterns are a result of the three-dimensional geometry of the scour hole. The above studies aimed to a better understanding of the scour hole development in heterogeneous subsoil and showed the effect of the three-dimensional scour hole geometry on the scour development. The topic of this thesis, however, is the scour development under lateral non-uniform incoming flow.

Broekema et al. (2018) and Van de Zande (2018) have studied the presence of lateral non-uniform incoming flow to the development of scour holes. The development of significant scour holes near the Eastern Scheldt Storm Surge Barrier were the motivation of their research. Field observations (Broekema et al., 2018) showed that during particular stages of the tidal cycle horizontal contraction of the tidal shallow jet flow at the barrier occurred instead of spreading in lateral direction as commonly observed in jet flow (e.g., Cohen, 2012), see for example Figure 2.16. If the upstream flow field is laterally uniform, horizontal contraction does not occur.

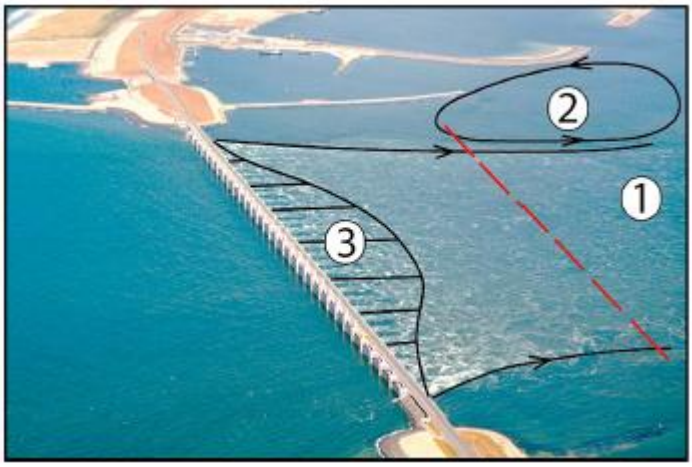

Figure 2.16: Aerial photograph of the flow at the Roompot inlet of the Eastern Scheldt Storm Surge Barrier. The red-dotted line denotes the edge of the bottom protection. (1) The flow is contracting towards the scour hole; (2) The presence of a horizontal recirculation zone; (3) The outflow from the barrier schematized as a jet (Broekema et al., 2018).

The horizontal contraction of the flow is attributed to the potential vorticity conservation by Broekema et al. (2018). Appendix B.1.6 gives more detail about the principle of conservation of potential vorticity. Due to the lateral contraction of the flow, boundary layer separation from the upstream scour slope can be suppressed and flow can stay attached to the bed. The vertical flow separation on a downward slope can be suppressed due to a reduction of the adverse pressure gradient responsible for separation of the boundary layer from the bed by the horizontal contraction of the flow. Vertical flow separation will be discussed in more detail in subsection 2.4.

Figure 2.17 presents the measurements of the vertical flow structures in the Eastern Scheldt Storm Surge Barrier for a longitudinal section during two stages in the tidal cycle. One can observe high near-bottom velocities during maximum flood (flow with large lateral velocity differences) in the lower panel, whereas in the upper panel one can observe a return flow at the upstream scour slope after slack tide (flow is relatively uniform in lateral direction). Broekema (2017) have performed laboratory experiments to investigate the development of flow with lateral velocity gradient over a sloping bed. It was shown that in case the lateral velocity gradient of the flow velocity upstream of the scour hole is sufficiently large, the flow can stay attached to the bed for relatively steep slopes. The two vertical flow structures on a downward slope as representation of the upstream scour slope is given in Figure 2.18. Figure 2.18a shows a flow with limited lateral velocity differences upstream the slope that will vertically separate. A vertical recirculation zone is formed and the velocities near the bed are relatively low. This flow pattern is similar to the flow pattern in two-dimensional scour holes as discussed in subsection 2.3.1. Figure 2.18b presents an incoming flow with large lateral velocity differences. The flow will converge in the horizontal plane and it will stay attached to the bed. The near-bed velocities are relatively high.

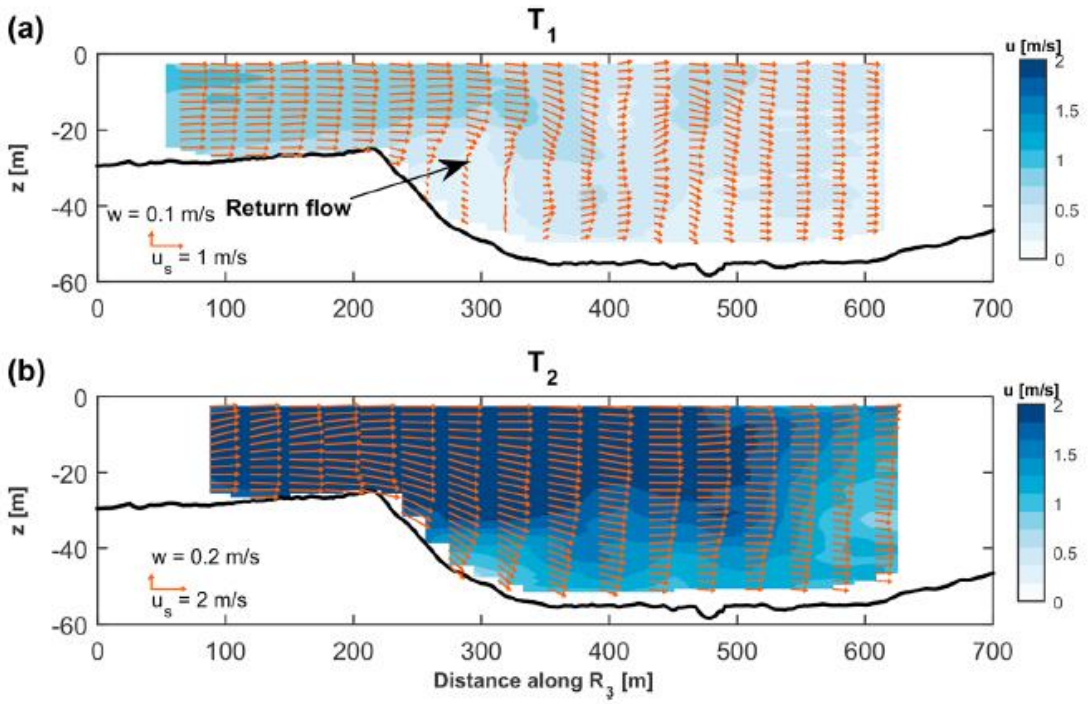

Figure 2.17: Velocity vectors along a longitudinal section named R_3 in the scour hole at Roompot. (a) Vertical flow separation and return flow; (b) The flow remains attached with high near bed flow velocities (Broekema et al., 2018).

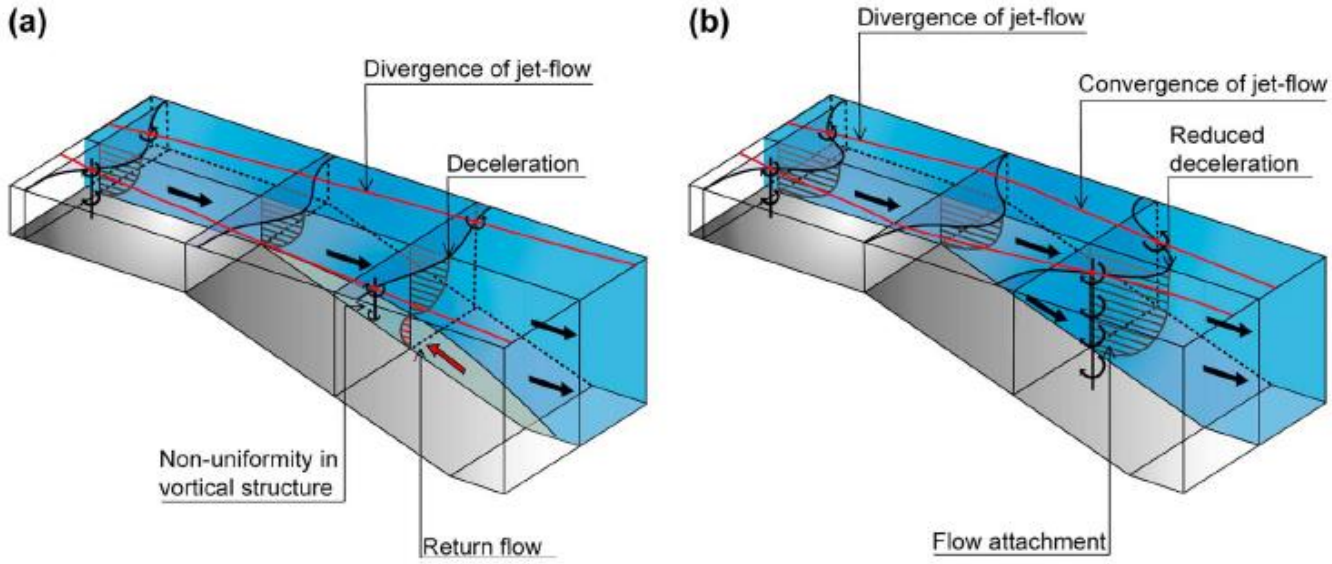

Figure 2.18: Conceptual sketch of the two different flow structures observed at the scour holes at the Eastern Scheldt Storm Surge Barrier. (a) flow with limited lateral velocity differences, vertical flow separation and divergence of jet-flow; (b) flow with large lateral velocity differences, vertical flow attachment and convergence of jet-flow (Broekema et al., 2018).

The experiment work of Van de Zande (2018) can be considered as an extension of the experiments of Broekema (2017). Unanswered form the work of Broekema (2017) was the effect of shallow flow conditions. Van de Zande (2018) have investigated the development of a shallow jet that experience a streamwise increase in depth. The study of Van de Zande (2018) aimed to obtain more fundamental understanding of the flow patterns in three-dimensional scour holes for laterally nonuniform flow. The scale experiments considered lateral velocity gradients by a lateral expansion, a local uniform depth increase modelling the upstream scour slope, relative shallowness and grid turbulence (Figure 2.19). The most relevant conclusions from the scale experiments are as follows:

Figure 2.19: An overview of the experimental setup with a lateral expansion, depth increase by a false bottom and grid elements (Van de Zande, 2018).

1. Vertical flow structure. Two types of vertical flow states were observed at the location of the downward slope in the performed experiments. Vertical flow attachment along the full width of the jet flow and vertical flow separation at the jet center with vertical flow attachment in the horizontal mixing layers. Van de Zande (2018) gave a schematic overview of these vertical flow structure as depicted in Figure 2.20.

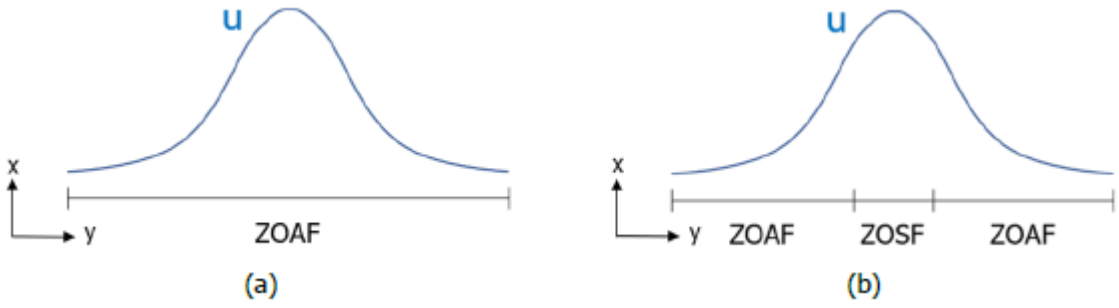

Figure 2.20: Schematic overview of the observed vertical flow states at the downward slope. (a) vertical flow attachment along the full width of the jet flow. (b) Vertical flow separation in the jet center and flow attachment in the horizontal mixing layers. ZOAF stands for Zone Of Attachment Flow and ZOSF means Zone Of Separated Flow (Van de Zande, 2018).

2. Geometric aspects. Mild bed slope steepness and a relatively low ratio of the upstream flow width over the lateral expansion contribute to vertical flow attachment.

3. Horizontal flow structure. A contraction of the flow at the downward slope has been observed by Van de Zande (2018), see Figure 2.21. Based on the experiments, however, it was shown that the convergence of the surface flow near the slope is not necessarily a characteristic for vertical flow attachment. The surface flow converged also in case of vertical flow separation of the jet center.

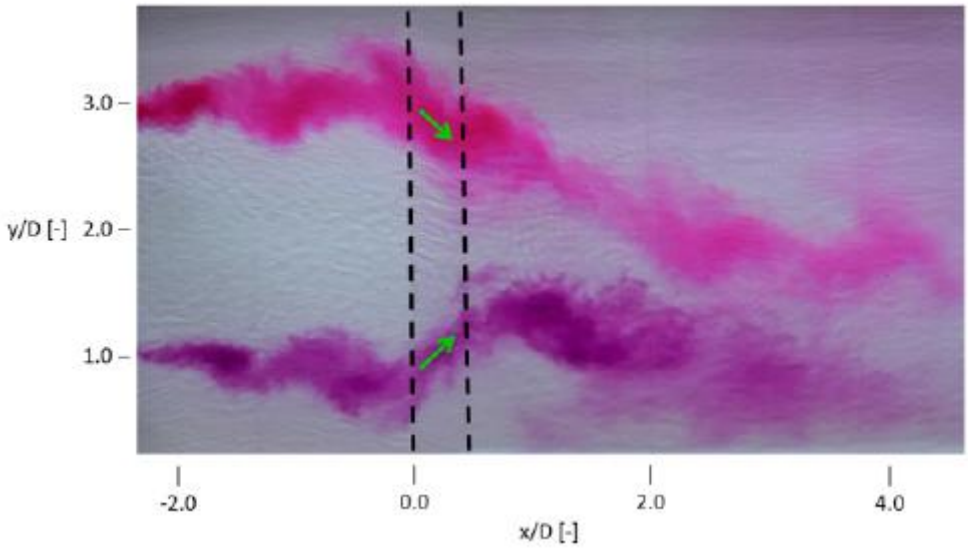

Figure 2.21: Contraction of flow at the downward slope. The black dashed lines show the location of the downward slope (Van de Zande, 2018).

4. Bed shear stresses. Higher bed shear stresses are observed for vertically attached flows compared to vertically separated flow. This strengthens that vertical flow attachment may enhance scour development in three-dimensional scour holes.

2.4 Horizontal shear flows

Horizontal shear flows are flows that are unidirectional and have a lateral gradient in the mean streamwise velocity. In most environmental horizontal shear flows such as a tidal inlet outflow from a culvert the horizontal dimensions are larger than the vertical dimensions. Horizontal shallow shear flows are predominantly flows with lateral gradients in the streamwise velocity and a water depth that is small with respect to the horizontal dimensions of the flow (Van Prooijen, 2004). The flow near the outlet structure can be characterized as a shallow flow as the horizontal dimension in the order of $O = 10\,m$ is larger than the local water depth in the order of $O = 1\,m$. As this thesis is concerned with the scour development under shallow flow with lateral velocity differences, this subsection discusses the most important properties of shallow jets and shallow mixing layers that have been described in literature. Appendix B.1.5 includes information on plane free shear flows.

2.4.1 Shallow jets

A jet is a flow into a large body of water with a very high velocity compared with the surrounding fluid. A shallow jet can be observed when a high-velocity is injected trough an opening (e.g., a slot, a channel or a nozzle) into a stagnant fluid in which the horizontal dimensions exceeds the water depth (Cohen, 2012). Figure 2.22 presents some properties of a plane turbulent jet flow.

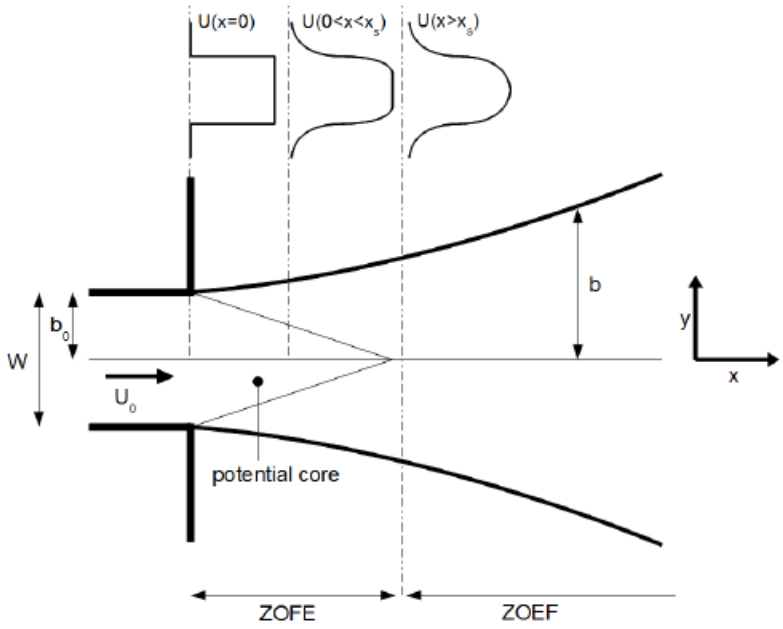

Figure 2.22: Definition sketch of plane turbulent jet (Cohen, 2012).

The jet can be divided into two distinct regions, the Zone of Flow Establishment (ZOFE) or flow development region and the Zone of Established Flow (ZOEF) or fully developed region. As the jets exits, a horizontal mixing layer develops on both sides of the jet in between the jet and the ambient fluid due to velocity differences. The jet accelerates the surrounding ambient fluid whereas the ambient decelerates the jet. Where the two mixing layers meet the potential core ends, the fully developed region starts. Beyond the

potential core, the flow velocity at the jet center falls below the velocity directly at outflow and the velocity profile approaches a self-similar Gaussian shape (Cohen, 2012). The mixing layers spread in lateral direction and it causes the growth of the jet with the distance (Cohen, 2012). Shallow water jets are influenced by the presence of bottom friction whereas there is no influence of a wall for free water jets (Van Prooijen, 2004). In shallow flows, neither the horizontal shear nor the bottom turbulence can be neglected (Van Prooijen, 2004).

Many researchers (e.g., Dracos et al. (1992); Jirka (1994); Cohen (2012)) have considered shallow water jets. Dracos et al. (1992) have studied the meandering of plane turbulent jets in shallow flows. The evolution of shallow jets in downstream direction is described by Dracos et al. (1992) as follows: In the near field $(x/h \leq 2)$ the jet is characterized by a regular development with significant influence of the boundaries. In the middle field $(2 \leq x/h \leq 10)$, the jet is dominated by secondary currents and the jet shows a strong three-dimensional velocity profile. In the far field $(x/h \geq 10)$, the secondary currents are damped out and the jet meanders around its center plane. It has been shown that the spreading of the jet is not significantly affected by the secondary currents and the meandering. Figure 2.23 illustrates the dye visualization of shallow jets in the experiments of Dracos et al. (1992).

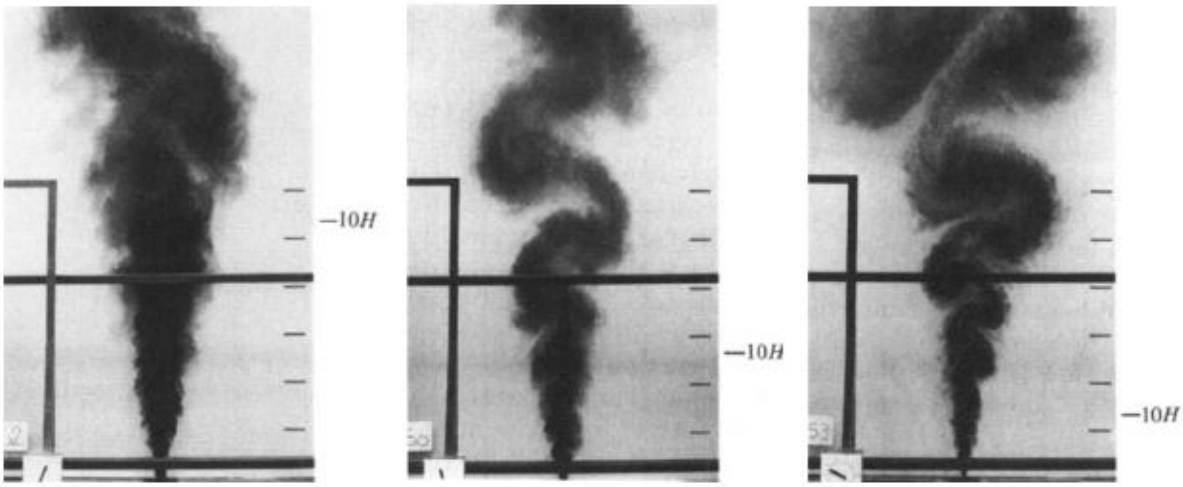

Figure 2.23: Photographs of the dye visualizations of shallow jets. The shallow jets with different water depth to exit width ratios: (a) $h/B = 16$; (b) $h/B = 8$; (c) $h/B = 4$. The solid bars are the support structure of the Laser Doppler Anemometry (LDA). The spacing between the marks on the figure equals $30\ cm$ (Dracos et al. (1992).

The considered shallow jets at the laboratory experiments of Dracos et al. (1992) had a high aspect ratio $(AR = depth/width)$ at the inflow, but after exit the horizontal dimensions were much greater than the depth. In most jet flows the aspect ratio is low as the aspect ratio of the shallow tidal jet from the culvert. The aspect ratio of the tidal shallow jet from the culvert is around $AR = 0.12$. Cohen (2012) have examined shallow jets with small aspect ratios that were shallow even in the near-field. The presented work aimed to improve knowledge of the dynamics and hydrodynamics of shallow water jets. The laboratory results have shown that shallowness influences the velocity field of the plane jet in particular the two-dimensional turbulence. For small AR, the velocity similarity profile change from a Gaussian profile into an increasingly squarer velocity profile.

2.4.2 Shallow mixing layers

A mixing layer develops at both sides of the jet. A mixing layer is a layer of flow where a gradient of shear or velocity exists. Talstra (2011) described the mixing layer as: “a region of lateral mixing and lateral shear, widening in downstream direction, containing a sequence of large-scale 2DCS that move downstream”. The abbreviation 2DCS refers to the large-scale turbulent structures (large scale quasi-2D coherent structures) in shallow flows (Talstra, 2011).

Two type of shallow flow geometries containing mixing layers have widely been studied. The Shallow Mixing Layer (SML) geometry that contains the confluence of two parallel streams experiencing a later velocity difference and the Shallow Lateral Expansion (SLE) geometry that involves an abrupt sideways widening of a uniform channel flow (Talstra, 2011). The laboratory experiments in this work are based on the SML geometry as given in section 3, therefore this subsection will continue with the SML geometry. For more detailed information about the SML geometry and in particular the SLE geometry, one is referred to for example Talstra (2011).

Figure 2.24 present a schematization of the SLE geometry including the most important flow features. The upstream velocity differences cause the formation of a shallow mixing layer. The lateral shear over the shallow mixing layer induces a sequence of large-scale 2DCS that move downstream. The 2DCS move downstream, grow in in size and eventually dissipate. The lateral shear decreases in downstream direction by streamwise transfer of momentum from the high toward the low velocity side due to momentum advection by 2DCS. The lateral gradient in mean streamwise velocity decreases dur to this turbulent mixing.

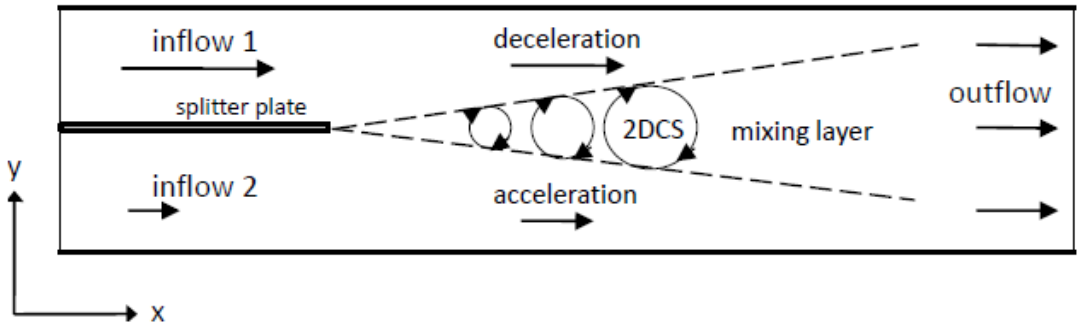

Figure 2.24: Top view on the Shallow Mixing Layer (SML) geometry including the most important flow features (Talstra, 2011).

Shallow mixing layer width

The development of large-scale coherent structures in a shallow mixing layer is analyzed by Van Prooijen & Uijttewaal (2004). The characteristic features of the downstream development of a shallow mixing layer flow are represented. The development of the mixing layer width $\delta(x)$ is given in the following expression (Van Prooijen & Uijttewaal, 2002):

$$\delta(x) = \alpha \frac{\Delta U_0}{U_c} \frac{h}{c_f} \left(1 - exp\left(-\frac{c_f}{h} x\right)\right) + \delta_0 \qquad (2.10)$$

in which: $\alpha = entrainment\ coeficicient \cong 0.085\ [-]$

$c_f = bed\ friction\ coefficient\ [-]$

$h = water\ depth\ [m]$

$\Delta U_0 = velocity\ difference\ at\ the\ inflow\ [m/s]$

$U_c = velocity\ in\ the\ center\ of\ the\ mixing\ layer\ [m/s]$

$x = the\ downstream\ position\ [m]$

$\delta_0 = initial\ mixing\ layer\ width \cong h\ [m]$

2.5 Vertical flow separation

As the formation of recirculation zones in the scour holes is expected to have a significant influence on the scour process, this subparagraph considers vertical flow separation. Schiereck (2012) describes that flow separation can be seen as the transition from wall flow to free flow. Flow separation occurs when a boundary layer loses contact with its wall as depicted in Figure 2.25. This is caused by an adverse pressure gradient, acting in the direction opposite to the local flow direction. This adverse pressure gradient can for instance be caused by a deceleration of the flow near a widening or deepening of the flow (Talstra, 2011).

The pressure gradient and the wall shear stress are the forcing terms that determine the boundary layer width. Normally along a solid wall, the pressure gradient and wall shear stress are the counteracting forces. Acceleration of flow as a result of a favorable pressure gradient (i.e. $\partial p/\partial x < 0$) tends to overcome the slowing down of the fluid particles caused by friction in the boundary layer. Deceleration of flow as a result of an adverse pressure gradient (i.e. $\partial p/\partial x > 0$) cause fluid particles in the boundary layer to slow down at a greater rate than only due to boundary layer friction. If the adverse pressure gradient is strong enough, fluid particles will be forced away from the body surface (flow separation) (Pritchard, 2011).

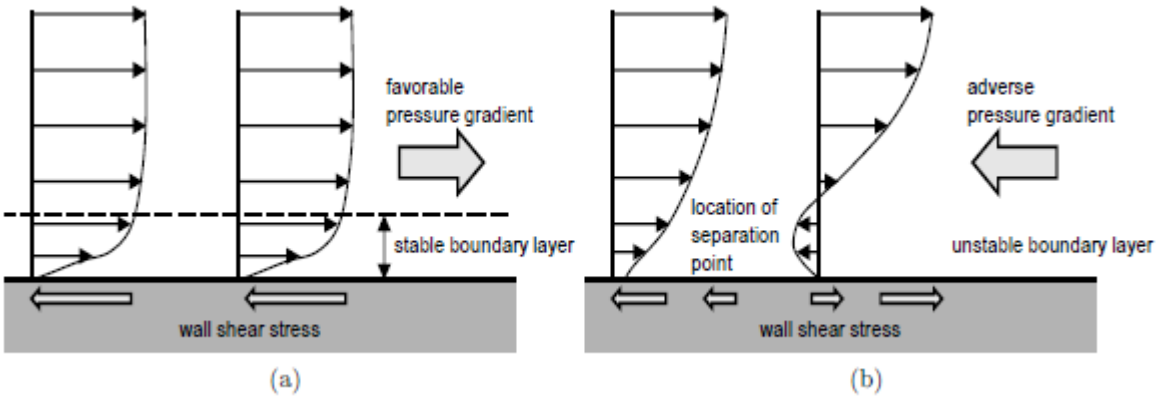

Figure 2.25: Principle of flow separation: the impact of the pressure gradient on a boundary layer equilibrium. (a) Favorable pressure gradient, stable boundary layer. (b) Adverse pressure gradient, separating boundary layer (Talstra, 2011).

2.6 Summary and discussion

This literature study has addressed the scour processes and the flow patterns in scour holes. Previous relevant work for this thesis is addressed. Furthermore, the theory of the horizontal shear flows is presented. A short introduction to the principle of vertical flow separation is given.

- The scour development in time is considered. Four different phases in the scour process are distinguished.

- The empirical relations for the prediction of scour holes are considered. According to Breusers (1966), the development of the scour process depends entirely on the flow velocity and turbulence intensity at the transition fixed to erodible bed. The hydrodynamic processes in a scour hole are not considered.

- Flow patterns in two-dimensional and three-dimensional scour holes are considered. The flow patterns in two-dimensional scour holes are similar to the flow patterns downstream of a sill. Flow patterns in three-dimensional scour holes can be different.

- The flow patterns in a three-dimensional scour hole geometry have been identified by scale experiments of Koopmans (2017), Stenfert (2017) and Uijttewaal et al. (2016).

- The work of Broekema (2017), Broekema et al. (2018) and Van de Zande (2018) has been discussed in more detail. The effect of incoming flow with lateral velocity differences on the flow patterns in scour holes have been presented. High near-bed velocities in the scour hole can be seen. The interaction between the horizontal structure and vertical structure could explain the three-dimensional scour development near hydraulic structures.

- Flow separation occurs when a boundary layer loses contact with its associated solid wall (Talsta, 2011). A favorable pressure gradient can suppress vertical flow separation.

In the next section, the laboratory experiments are presented in order to give more insight into the scour development for flow with lateral nonuniformities. The experiments can be considered as the extension of the experiments of Broekema (2017) and Van de Zande (2018). The development of flow with lateral velocity gradients over a sloping bed and the development of a shallow jet over a local uniform depth increase have focused only on the hydrodynamic processes. Experiments including a erodible bed was the next step in the ongoing research of the influence of lateral non-uniform flow on the scour process. development of flow with lateral velocity gradient over a sloping bed

3 Laboratory experiments

This chapter presents the laboratory experiments to investigate the scour development under lateral non-uniform flow. The influence of lateral gradients in the streamwise velocity on the spatial and temporal scour development will be studied. The experiments in this research will be part of the ongoing research on the behavior of these types of flows over a streamwise varying bathymetry and it will continue on the previous experiments by Broekema (2018) and Van de Zande (2018). The physical experiments that are conducted in a flume in the Fluid Mechanics Laboratory at the Delft University of Technology will help to answer the predefined research question and sub questions.

3.1 Experimental setup

The scale experiments were conducted to systematically investigate essential hydrodynamic processes near and in scour holes as observed in the field. The observed flow characteristics in the field were: a shallow jet with large horizontal velocity differences, a recirculation zone adjacent to the main flow, a less horizontal spreading of the jet-type flow in case of the culvert. In addition, the observations of the hydrodynamical processes in the scour hole nearby the ES-SSB has also been taken into account in the setup of the experiment. A horizontal contraction of the tidal jet towards the nearby scour hole and vertical flow attachment in the downstream scour hole during particular stages of the tidal cycle are regarded.

In order to investigate the most essential hydrodynamic processes, the scale experiment is simplified and includes a lateral velocity gradient in the flow and significantly large horizontal dimensions than vertical dimensions to simulate the effect of shallow flow conditions. To isolate the flow processes observed in the field, the following two important simplifications were made in the physical scale model:

- **Lateral velocity gradient;**
This thesis is concerned with shallow shear flows that contains the confluence of parallel streams with a lateral velocity difference. The lateral non-uniformity is generated by partially blocking the flow at the sides of the domain. This yields high flow velocities in the center of the domain and low flow velocities on the sides of the domain such that this flow shows similarities to a horizonal jet. This geometry is referred as Shallow Mixing Layer (SML). The shallow shear flows that have their virtual origin in flow separation are not chosen, because of the presence of horizontal recirculation cells. These shallow recirculation zones could have an impact on the development of the mixing layers (Talstra, 2011). Furthermore, in most laboratory experiments (e.g., Van de Zande, 2018; Bergsma & Bogaard, 2011) the horizontal recirculation cells influence the flow to move to one of the sidewalls. Despite the symmetry of the setup of the flow field, the flow often behaved asymmetrically. In conclusion, a SML geometry is chosen for the experiments in this work because no impact on the mixing layer as well as no asymmetrical flow is wanted.

- **Constant and unidirectional flow;**
A constant discharge was maintained in all the experimental runs. The flow was directed from the inlet section towards the outlet section of the flume. The influence of the tidal movement with the reversal of the flow direction was ignored.

The experiments work was conducted in a flume of $7\ m$ length, $1.2\ m$ width and $0.23\ m$ depth. To ensure that the flow was more or less uniform and that the streamlines were straight, the water entered the flume through a honeycomb flow straightener. The inlet section of the flume consisted of three parts separated by 1-m-long thin wooden plates. The sides of the inlet section were partially blocked with brick elements to establish a lateral velocity difference over the cross profile. Furthermore, floating foam boards were placed just downstream of the flow straightener in between the wooden plates to suppress surface waves. A rough steel plate with an inflow length of $2\ m$ was available to develop a more or less fully turbulent boundary layer at the start of the mobile bed. A sharp crested weir regulated the outflow at the downstream end of the flume. Figure 3.1 gives a top view and side view of the experimental setup.

Considering a maximum water depth of 10 cm and a sand bed height of 10 cm in the flume, the flow in the flume can be considered as shallow given a water depth-width ratio of 1:12 and water depth-length ratio of 1:70.

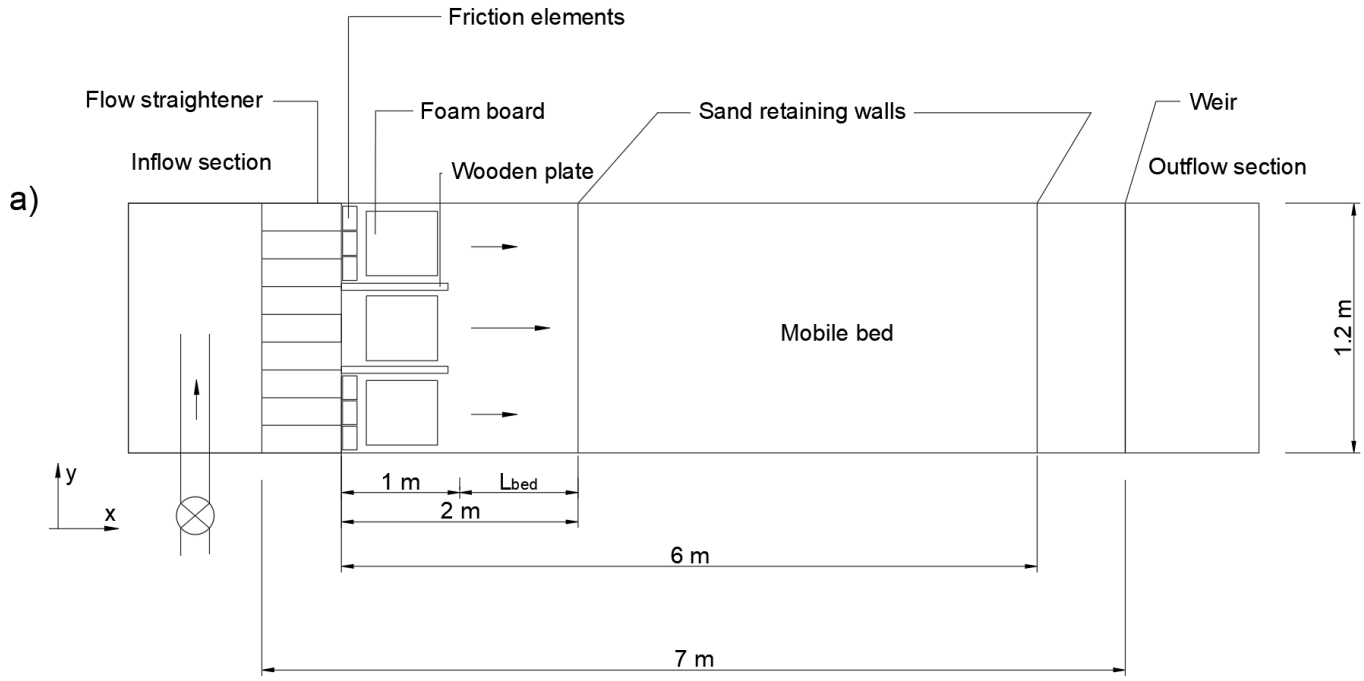

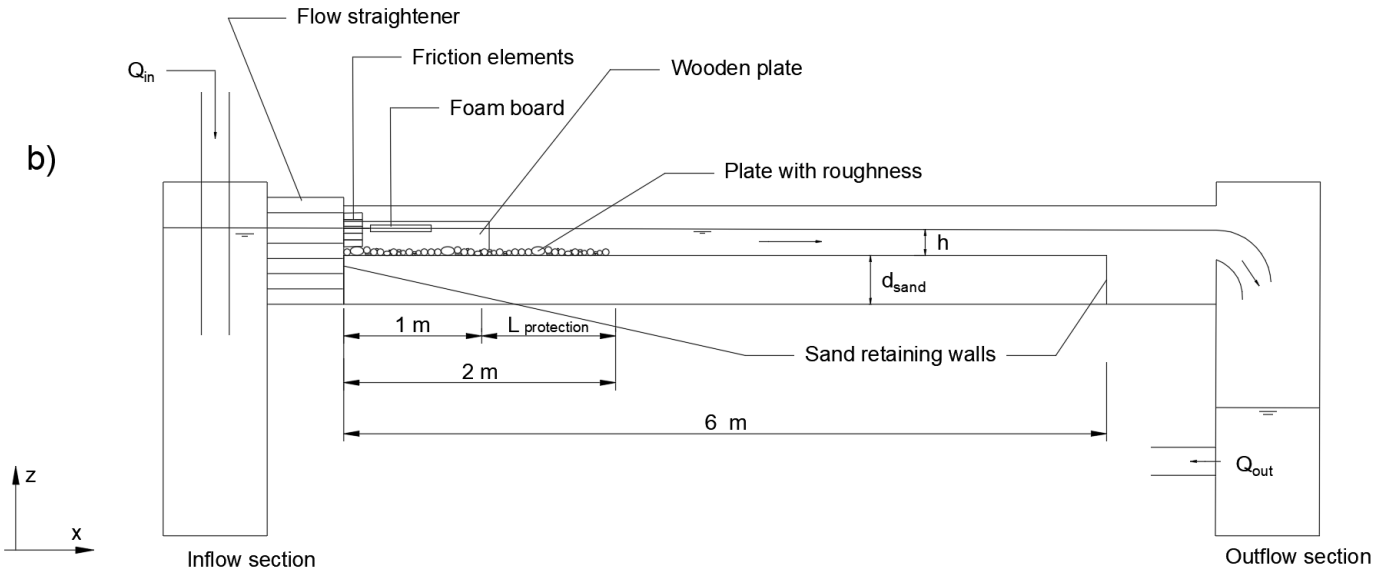

Figure 3.1: (a) Top view of the experimental setup including the main dimensions. (b) Longitudinal cross section of the experimental setup including the main dimensions.

3.2.1 Coordinate systems

Figure 3.2 presents the coordinate system used throughout the experiments. The x, y and z axes indicate the longitudinal, lateral and vertical direction. The origin of the coordinate system is chosen at the right sidewall at the end of the bed protection. Furthermore, the flow velocity components u, v and w are in agreement with the x, y and z-direction of the coordinate system.

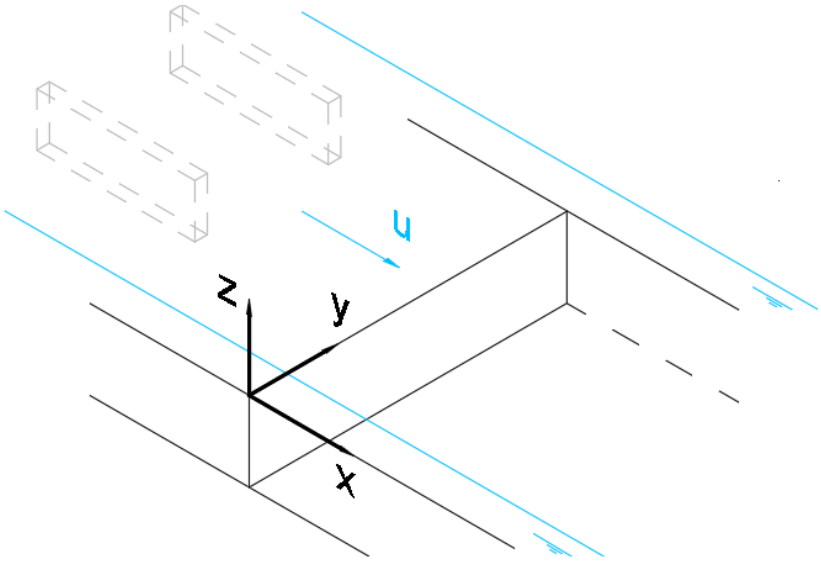

Figure 3.2: Definition of the coordinate system. The origin of the coordinate system is at the right sidewall at the end of the bed protection. The dashed rectangular shapes upstream indicate the wooden plates.

3.2 Scaling and parameter space

The fundamental condition to be satisfied in a model test is that the model must behave in a manner similar to the real scale, often referred as prototype or field. It should be note that the aim of the model test is to give insight into the scouring processes. The laboratory experiments were only intended to reproduce the most relevant processes in real scale and not to exactly scale the model test to a prototype. In the design of the model test, the outlet structure is considered as the prototype. The necessary scale of a model is chosen in such a manner that the most important conditions and structural parameters are reproduced to an adequate degree (Frostick, McLelland and Mercer, 2011). Scale means the relation between the value of some parameter in prototype and model, usually indicated as n. For example, for a certain quantity x the scale factor is:

$$n_x = \frac{x_p}{x_m} \tag{3.1}$$

in which: $n_x = scale\ factor\ [-]$

$x_p = quantity\ in\ prototype\ (subscript\ p)$

$x_m = quantity\ in\ model\ (subscript\ m)$

Similarity between prototype and model can be required in three general categories: geometric (shape), kinematic (velocities) and dynamic (forces) similarity. As the scale of down-scaled model differs from the scale of the prototype, it is not possible to simulate all relevant variables correctly and scale effects occur. In order to correctly scale the processes in the experiment well, geometric scaling and scaling laws for both the hydrodynamic and sediment dynamics are considered.

3.2.1 Geometric scaling

In this subsection, the length scales that are considered in the design of the experimental setup are discussed. The best geometrical scale has been chosen based on the most important processes in the prototype and the available laboratory flume.

- Water depth and scour depth;

The choice of the water depth in the model depended on the available flume height, a sufficient sand bed height for the scour development, a sufficient measurement accuracy and the intended flow velocities in the experiments. A water depth of $h_{model} = 0.08\ m$ was intended in the experimental setup. This water depth is large enough to have sufficient measurement accuracy (de Vries, 1982) and it is not too large to have a sufficient sand bed height for the scour development. A sand bed height of $d_{sand} = 0.12\ m$ was present for the scour development.

- Bottom protection;

The bed protection is represented as a part of the steel plates with roughness after the wooden plates, see Figure 3.1. In the experiments, the length of the bed protection is thus the distance from the end of the wooden plate to the sand bed. The length of the bed protection is important, because this length determines

the widening of the horizontal mixing layers in the horizontal plane. The bed protection length discerns the flow development region and the fully developed flow region of a jet flow. In case of the culvert, the initial bed protection length $L_{b,p}$ over the width W_p is $L_{b,p}\ /W_p = 2.3$. The length of the bed protection in the experimental setup is fixed and it is taken as $1\ m$. The ratio of bed protection length over the width is chosen to be a variable in the experiments. In this present work, two different ratios of the length of the bed protection over the inflow length are considered. Namely, a ratio of $L_{b,m}/B_m = 2.5$ and a ratio of $L_{b,m}/B_m = 5$ are regarded in the model tests.

As mentioned, the bed protection was simulated by steel plates ($5\ mm$ thick) with glued grains (medium gravel). These plates with roughness were available in the laboratory. The Chézy value of the bed protection was approximated on $C = 33.1\ \sqrt{m}/s$ by taking the hydraulic radius $R\ \approx h = 0.08\ m$ and the equivalent roughness of Nikuradse $k_s = 2 \cdot 7 \cdot 10^{-3}\ m$.

$$C = \frac{\sqrt{g}}{\kappa}\ln\left(\frac{12R}{k_s}\right) \tag{3.2}$$

in which: $\kappa = \ constant\ of\ Von\ Kármán, 0.4[-]$

$R\ = hydraulic\ radius\ [m]$

$k_s\ = equivalent\ roughness\ of\ Nikuradse\ [m]$

- Width of the jet;

It was intended to have no influence of the sidewalls on the widening of the shallow mixing layer at the end of the bed protection. Therefore, the mixing layer region should not touch any sidewall. The shallow mixing layer width by Van Prooijen (2004) is considered for the choice of the width of the jet. Based on the literature study the development of the width of the mixing layer can be estimated, see subsection 2.4.2. The theoretical expression for the shallow mixing layer width of a SML geometry based on the model approach by Van Prooijen & Uijttewaal (2002) reads:

$$\delta(x) = \ \alpha\frac{\Delta U_0}{U_c}\frac{h}{c_f}\left(1 - exp\left(-\frac{c_f}{h}x\right)\right) + \delta_0 \tag{3.3}$$

The width of the mixing layer at the edge of the bed protection is determined on $\delta(x = 1\ m) = \ 16\ cm$ based on the entrainment coefficient $\alpha \approx 0.085$, the bed friction $c_f = g/C^2 = 0.0095$, the water depth $h = 0.08\ m$, the velocity difference at inflow $\Delta U_0 = U_1(x_0) - U_2(x_0) = 0.45 - 0.15 = 0.3\ m/s$, the velocity in the center of the mixing layer $U_c = 1/2 \cdot \left(U_1(x_0) + U_2(x_0)\right) = 0.3\ m/s$. It was expected that the mixing layers do not touch the sidewalls at the edge of the bottom protection even taking into account a lateral shift of the mixing layer toward the low velocity zone. Based on the previous and taking the ratio of the width of inflow over water depth in the prototype of $B_p\ /h_p = 6.2$, the width of the jet or the distance of the wooden plates was chosen to be $B_{jet} = 40\ cm$ and $B_{jet} = 20\ cm$.

3.2.2 Hydrodynamics

It is expected that Froude-scaling is dominant in reproducing hydrodynamics of free-surface flows (Frostick, McLelland and Mercer, 2011). The Froude number expresses the ratio of the inertia force over the gravitational force and is given by:

$$Fr = \frac{U}{\sqrt{gh}} \tag{3.4}$$

where: $U = velocity\ scale\ [m/s]$

$g = gravitional\ acceleration\ [g = 9.81\, m/s^2]$

$L = length\ scale\ [m]$

The maximum in field Froude number corresponding to the flow at the location of the bed protection can be characterized as sub-critical. The Froude number in the field at the end of the bed protection is $Fr = 0{,}7$ for maximum flow conditions. In addition, the Froude number in the experiments should be sufficiently low $(Fr < 0.5)$ to minimize the effects of surface disturbances (van Prooijen & Uijttewaal, 2002). These surface disturbances were undesired as they could affect the bed. These small surface waves may result in bedforms that might contribute in less clear scour depth measurements. For these experiments, a flow velocity of $\bar{u}_{model} = 0.45\ m/s$ is considered. Based on a water depth of $h_{model} = 0.08\ m$, the Froude number in the small-scale model is $Fr = 0{,}45$.

The second flow scaling parameter that is considered is the Reynolds number. The Reynolds number is used to express the ratio of the inertial force over the viscous force and it is reads:

$$Re = \frac{UL}{\nu} \tag{3.5}$$

where: $U = velocity\ scale\ [m/s]$

$L = length\ scale\ [m]$

$\nu = kinematic\ viscosity\ [m^2/s]$

The Reynolds number in the field is in the order of 10^6 for maximum flow conditions. It is not possible to have this order of the Reynolds number in the down-scaled model. Reynolds similarity require an increase of the flow velocities in the model compared to the prototype. In the experiments however, a lower flow velocity is considered. As a consequence, a lower Reynolds number is maintained in the experiment. The Reynolds number in the model, based on the velocity and water depth, is in the order of 10^4. The corresponding Reynolds number in the experiment is considered to be sufficiently high to ensure the flow to be turbulent $(Re > 4000)$ (van Prooijen & Uijttewaal, 2002). The viscous effects will be more pronounced in the model than in the prototype due to a lower Reynolds number in the model.

3.2.3 Sediment dynamics

For the experiments in this present work, silica sand M32 is used as the “model” sediment. Silica M32 is chosen based on theoretical as well as practical reasons. Ideally, the sediment in the model should be chosen in such a way that the ratio of the flow velocities and critical velocities are (nearly) the same in the field and in the model. Breursers & Raudkivi (1991) characterizes the similarity of sediment transport as:

$$n_u = n_{u_c}$$

However, it is impossible to fulfill this criterion for fine sediments as present in the field. For example, sand with a nominal diameter of $d_{50} = 125 - 200\ \mu m$ as present near the outlet structure scaled at the ideal velocity scale would have a model grain diameter corresponding to silt or clay. The model sediment would not be representative anymore for the prototype sand, because the behavior of the model sediment would be dominated by electro-chemical forces (Frostick, McLelland and Mercer, 2011). The use of materials with lower specific weight such as for example bakelite or polystene as “model” sediment could be considered, however the use of light-weight sediments would make it more complex. Therefore, silica M32 is chosen as model sediment in this present work and Table 3-1 shows the most important properties and calculated parameters of this sediment type.

Sand	$\boldsymbol{d_{50}}$ $[\boldsymbol{\mu m}]$	$\boldsymbol{D_*}$ $[-]$	$\boldsymbol{\Psi_c}$ $[-]$	$\boldsymbol{\bar{u}_c}$ $[\boldsymbol{m/s}]$
Silica M32	260	6.58	$0.015 - 0.04$	$0.15 - 0.24$

Table 3-1: Sediment characteristics.

As mentioned, silica M32 is also chosen based on practical reasons. A practical reason to consider silica M32 is the grain diameter in combination with the critical mean flow velocity. The value of the critical velocity further on is assumed to be $\bar{u}_c = 0.24\ m/s$, see section 2.1. Stenfert (2017) illustrates that the critical mean flow velocity for sand with a smaller grain size and silica M32 is more or less equal. Therefore, the silica M32 is more advantageous in terms of filtering. The larger the sediment, the easier the filtering process. Another important practical reason to use silica M32 for the experiments is that this type of sediment type is used in previous investigations on scour development in the Fluid Mechanics Laboratory by for example Van Zuylen (2015). The present experiments could be compared with previous investigations, since scale effects of sediments are similar in both experiments.

3.2.3 Scaling of prototype-model

Table 3-2 gives an overview of the scaling factor between prototype and the model. The outlet structure is indicated as field.

Parameter	Unit	Symbol	Field	Model	Scale factor
Froude number	$[-]$	Fr	0.7	0.45	1.6
Reynolds number	$[-]$	Re	$5 \cdot 10^6$	$2.8 \cdot 10^4$	180
Width	$[m]$	B	10.5	0.40	26
Length protection	$[m]$	$L_{bed\ protection}$	24	1	24
Water depth	$[m]$	h	1.7	0.08	21
Velocity	$[m/s]$	u	1.5	0.45	3.3
Critical velocity	$[m/s]$	u_c	0.3	0.24	1.25
Relative density	$[-]$	Δ	1.65	1.65	1
Diameter sand	$[\mu m]$	d_{50}	130	260	0.5
Shields parameter	$[-]$	Ψ	0.06	0.04	1.5
Chézy coefficient (sand bed)	$[m^{1/2}/s]$	C	88.2	58.9	1.4

Table 3-2: Overview of parameters prototype and model.

3.3 Experimental cases

Here, the laboratory experiments to investigate the influence of lateral non-uniformities in the flow on scour development are presented. Three different cases are investigated. Figure 3.3 presents the different geometries that are tested. The cases are referred to as case 1, 2 and 3.

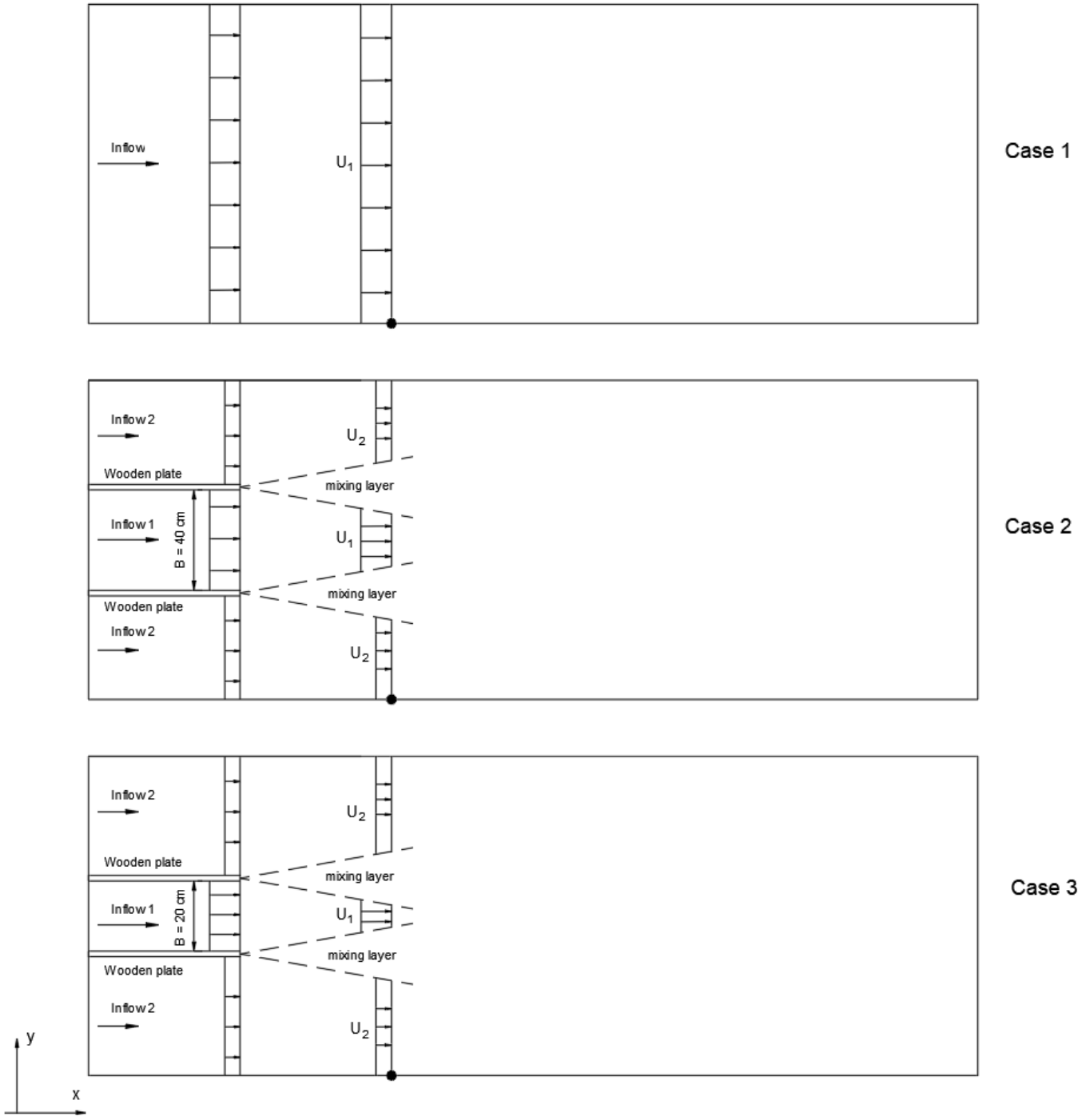

Figure 3.3: Overview of the three test cases. The dashed lines indicate the shallow mixing layers. The solid dot indicates the origin of the reference frame ($x = y = 0$).

First, the scour development under lateral uniform flow will be studied. The first test will be a reference case and the results will be compared with previous results (e.g., Breusers, 1966; Van Zuylen, 2015) in order to validate the experimental set-up. The scour development should be described well with the 2DV empirical relations. The influence of the lateral gradients in the streamwise velocity of the flow on the scour development will be investigated in the second and third experimental case. Experimental case 2 as well as experimental case 3 contain the confluence of three parallel streams with different velocities. The outer streams both have a velocity of U_2 and the inner stream a velocity of U_1, with $U_1 > U_2$. Both case 2 and 3 include a shallow mixing layer. The shallow mixing layer will grow between the high flow velocity and low flow velocity. The difference between experimental case 2 and 3 is the width at the inflow. By varying the upstream boundary condition through the inflow width, the jet characteristics could be changed.

The flow in experimental case 2 and case 3 shows similarities to a horizontal jet and it is considered to be comparable to the flow at the outlet structure and the Eastern Scheldt Storm Surge Barrier. The three-dimensional scour development in case 2 and case 3 will be compared both to reference case 1 as to the three-dimensional scour experiments in literature (e.g., Van der Meulen & Vinjé, 1975). The presence of lateral velocity gradients introducing three-dimensional scour are shared. Therefore, it is expected that the scour development of the three-dimensional scour in this present work is comparable with the three-dimensional local scour development by Van der Meulen & Vinjé (1975).

3.3.1 Description of the experimental runs

An overview of the experimental runs is given in Table 1:

Run	Water depth, $h_0[cm]$	Velocity $[m/s]$		Width, B_{jet} $[cm]$
1	7.4	$\bar{u}_1 = 0{,}48$	$\bar{u}_2 = 0{,}51$	-
2	7.8	$\bar{u}_1 = 0{,}49$	$\bar{u}_2 = 0{,}13$	40
3	7.8	$\bar{u}_1 = 0{,}46$	$\bar{u}_2 = 0{,}07$	20

Table 3-3: The conditions of the experimental cases. The water depth is measured at the transitions between the fixed bed and erodible bed, x_0. The velocities are measured in time and the values of the high velocity $\bar{u}_1$ and the low velocity $\bar{u}_2$ in the table are the averages of these measured time-averaged flow velocities in time. The time-averaged flow velocities are measured in the water column at the transition between the fixed bed and erodible bed at approximately half the initial water depth h_0. The high velocity $\bar{u}_1$ is measured at the centerline and the low velocity $\bar{u}_2$ is measured at $10\ cm$ (run 2 and run 3) and at $20\ cm$ (run 1) from the sidewall of the flume ($y = 10\ cm, y = 20\ cm$).

In order to compare the different experimental cases with each other, the imposed boundary conditions through the water depth h_0 and the time-averaged high velocity $\bar{u}_1$ are more or less equal.

3.4 Measurements techniques

Several measurement techniques have been used to measure the scour hole development in time and to qualitatively and quantitatively describe the flow field in the scour hole.

3.4.1 Laser

The scour hole depth in time and subsequently the bed profiles are measured by a laser. The laser was placed in a small boat with a transparent bottom to measure under water. The laser equipment was connected to a cart above the flume that could change its position in longitudinal direction by rolling over a track on the side of the flume. The cart was connected to a trigger wheel that could track its position in the longitudinal direction. In addition to the movement of the laser in the longitudinal direction, the laser could also move in the lateral direction by sliding the laser over the cart. Figure 3.4 illustrates the setup of the laser measurement in this present work.

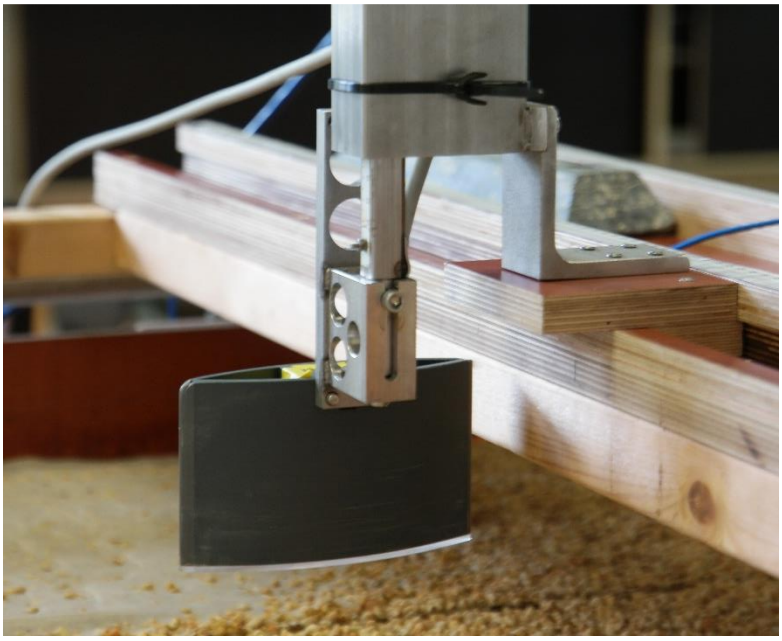

Figure 3.4: Laser measurement setup.

The laser is used to measure the bed in time and in space. As initially the development of the scour is fast, the bed is measured more regularly at the beginning of the experiment than later on. Figure 3.5 shows the transects over which the laser measured the bed profile in time for the different experimental cases. As the spatial variability of the scour process is more important for the lateral non-uniform cases, more measurements are done across the flume. The bed measurements were taken along three transects under lateral uniform flow, whereas the laser measurements were along eleven transects under the lateral non-uniform cases.

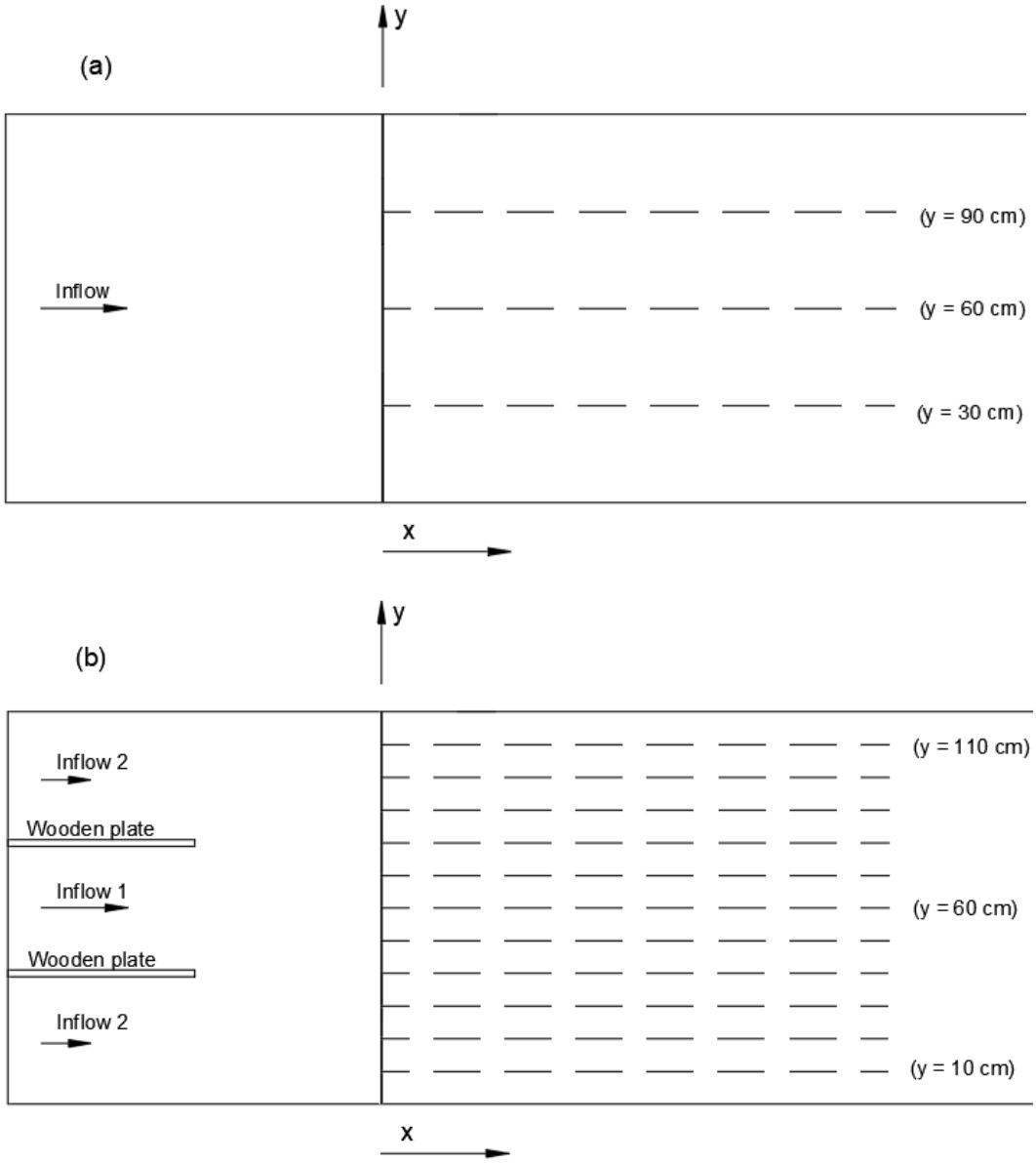

Figure 3.5: Laser measurements along transects; (a) lateral uniform flow (b) lateral non-uniform flow.

Calibration

Before the experiments, the laser instrument is calibrated. The output of the laser is a certain voltage between 2 and $10\ V$. In air, this corresponds to a distance of 6 and $26\ cm$ with a linear change in between. Whereas in water, this corresponds to a distance of 7.8 and $33.8\ cm$ due to a different refraction index. The laser in the submerged boat used to measure the bed profiles is calibrated through measuring the difference between a flat bottom and a known size of a block in water. It is determined that $1V$ corresponded to an average of $3{,}3\ cm$. Furthermore, the laser has a measurement accuracy of around $0.001\ V$.

3.4.2 Visualization of the flow

Colored dye injections in the flow helped to identify some flow characteristics in the water flow at various locations in the flume. These qualitative measurements was focused on the horizontal flow structure of the flow at the surface and it helped to identify flow characteristics such as the lateral flow velocity difference, the widening of the shallow mixing layer in downstream direction, the sequence of 2DCS in the shallow mixing layers, the growth of these eddies in the shallow mixing layer, the direction of the shallow mixing layers or jet flow and the turbulent mixing. Figure 3.6 illustrates some flow characteristic identified by dye injection.

(a)

(b)

Figure 3.6: Dye injection. Flow is from top to bottom. (a) lateral flow velocity difference, high velocity in the middle and low velocity at the sidewall. (b) the 2DCS in and the widening of the shallow mixing layer.

3.4.3 Acoustic Doppler Velocimetry

An Acoustic Doppler Velocimetry (ADV) is a measurement technique that can be used to determine full three-dimensional velocity vector at a single point in the flow. Figure 3.7 gives a schematized view of this single point method. An ADV is based on the Doppler shift effect of emitted acoustic signals after reflection by small sound-scattering particles in the flow (Nortek AS, User Guide Vectrino velocimeter). The Doppler shift in the frequency of the scattered sound is proportional to the flow velocity assuming that these small particles in the fluid have the same velocity as the flow velocity (Uijttewaal, 2017).

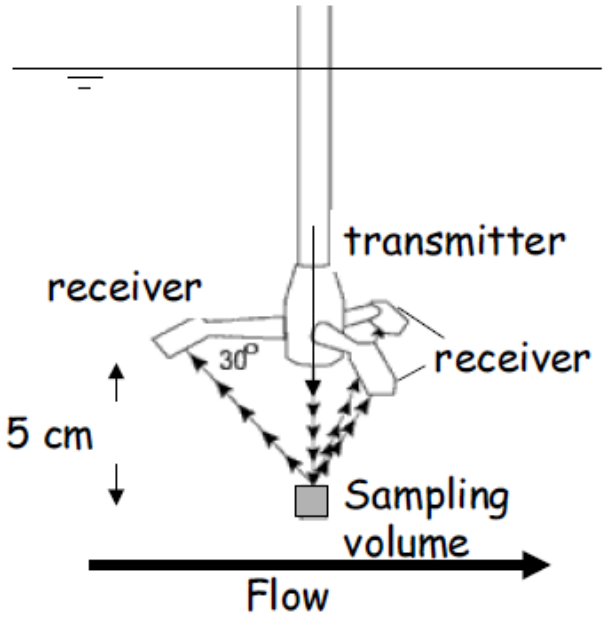

Figure 3.7: The velocimeter operating principle (Uijttewaal, 2017).

A Vectrino 2D-3D Sidelooking, fixed stem of Nortek was used to perform the ADV measurement. The device has a sampling volume with a diameter of $6\ mm$ that is located at $50\ mm$ from the probe. A maximum sampling rate of 25 Hz was used. For the measurements with the ADV, oxygen bubbles were used as sound-scattering particles in the flow. This method involved the placement of a frame with thin platinum wire in the flow before the ADV instrument and the placement of a metal bar in the flow. The thin wire acted as a cathode and the metal bar acted as an anode in an electrical circuit. The oxygen bubbles were generated by electrolyzing the water. Figure 3.8 illustrates the Vectrino ADV and the bubble frame in the experiment.

Figure 3.8: Measuring the velocities using ADV and bubble frame.

Data acquisition

The ADV measurements were performed to quantitatively describe the horizontal as well as the vertical flow structure nearby and in the scour hole. In order to describe the horizontal flow structure, the ADV measurements were conducted in time along longitudinal transects at the end of the bed protection and in the scour hole nearly at the deepest point. The measurements were taken at $t = 0, 90, 180$ and $360\ min$. It is assumed that this flow velocity is representative to describe the horizontal flow structure in the flow. The ADV measurements were taken in the xy-plane for the x-coordinates at the transition between fixed and mobile bed and approximately at the deepest point in the scour hole and for the y-coordinates at $y = 10, 30, 40$ and $60\ cm$. For the lateral uniform case, the measurements were taken at the y-coordinates $y = 20$ and $60\ cm$. In addition, the ADV measurements were taken at a fixed position of $4\ cm$ from the water level surface in the xz-plane. As an example, Figure 3.9 shows the locations of the ADV measurement points for the geometry of $B_{jet} = 40\ cm$. Based on symmetry, the ADV measurements were taken only at half width.

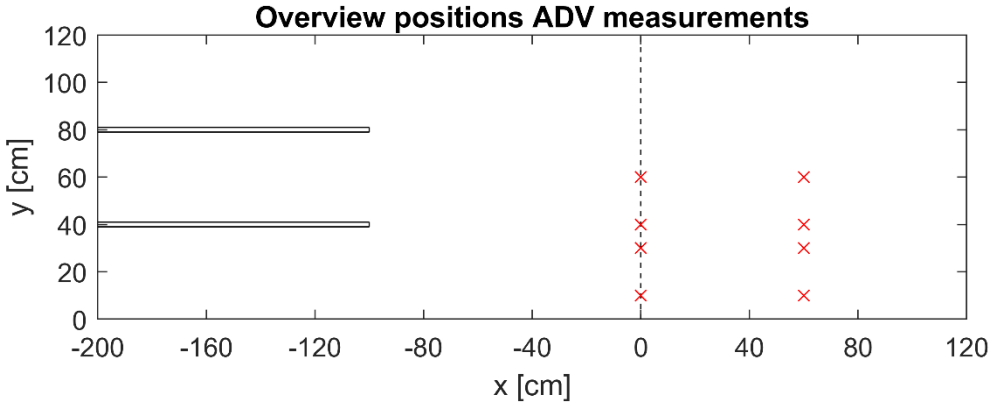

Figure 3.9: Overview of the positions of the ADV measurements for the horizontal flow structure for example the geometry $B_{jet} = 40\ cm$. The ADV measurement points are indicated as red markers. Only the x positions of the ADV measurement at the deepest point of the scour hole are not fixed due to the movement of the deepest point in time. In this subplot, the x position of the deepest point is set on $x = 60\ cm$ as an example.

In order to describe the vertical flow structure in the experiments, the ADV measurements were conducted along a longitudinal transect in the centerline of the flume at the end of the experimental run. The ADV measurements were taken just before the bed protection, approximately halfway the upstream slope of the scour hole and approximately at the deepest point of the scour hole. These ADV measurement were taken at five different locations in the water column, namely: one at the bed, two points slightly above the bed, one point in the middle of the water column and one point near the water surface. As an example, Figure 3.10 shows the locations of the ADV measurements in a schematic view for one of the experimental runs. Furthermore, the ADV measurement were collected for time-series of three minutes per data-point. This is assumed to be sufficient for a statistical analysis.

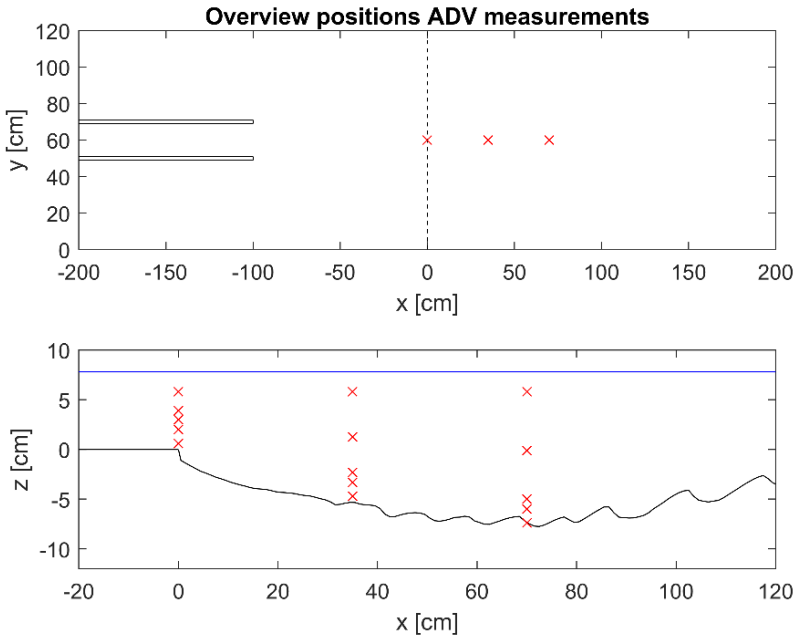

Figure 3.10: Overview of the ADV measurements for example the geometry of $B_{jet} = 20\ cm$. The measurement points are indicated as red markers. The top view is indicating the xy positions of the measurement points. The end of the bed protection indicated by the black dashed line. The side view is showing the xz locations of the measurement points between the bottom profile indicated by the black line and the water level indicated by the blue line.

Data post-processing

ADV signal outputs not only include turbulent velocity fluctuations, but also disturbances. ADV velocity data should therefore not be used without adequate postprocessing (Garcia et al. 2005). The contaminated ADV signal output was filtered by a two-step filter to a clean ADV signal. The outliers in the ADV data were detected and removed by the inbuilt Hampel filter of MATLAB and by the phase-space filter algorithm of Goring and Nikora (2002). The Hampel-function uses a half-width window size DX and a threshold value T to filter the ADV data. In the data-post processing, a half-width window of ten data points and a threshold parameter of 3 were used to filter the ADV data. The phase-space filter considers the first and the second derivatives of the ADV time series signal and excludes the outliers using the phase-space threshold method. The reader is referred to Goring and Nikora (2002) for more information of about this method. Figure 3.11 depicts a “raw” ADV signal and a filtered “clean” ADV signal for one measurement point.

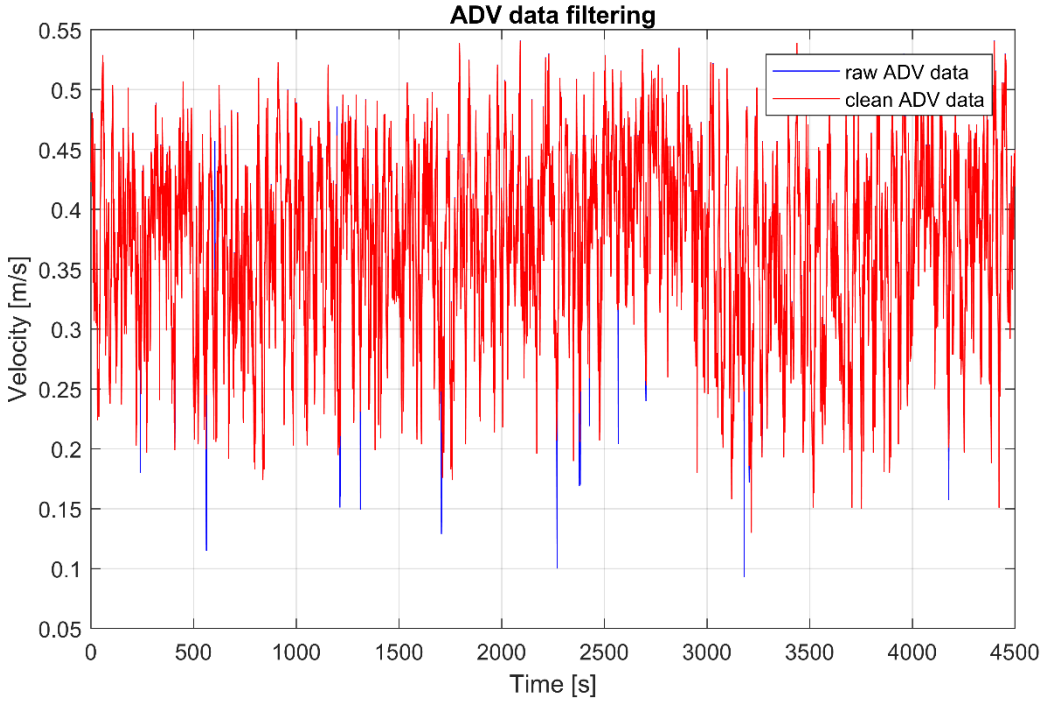

Figure 3.11: Data filtering for measurement point $(x, y, z) = (35, 60, 5.8)$ for 3D scour $B_{jet} = 20\ cm$.

Measurement inaccuracy

The measurement inaccuracies of the ADV measurement technique resulted mostly from:

1. Disturbances of the flow by the measurement device and the frame of the wire mesh;

2. The tiny air bubbles that are generated by the wire mesh could not correctly follow the movement of the water. The tiny air bubbles move towards the water surface.

3.5 Discussion

The previous section analyzed the experimental setup, the scale effects and the measurement techniques concerning the laboratory experiments. Also, the calibration of the laser instrument and the measurement inaccuracies of the ADV measurements are regarded. In order to complete this section, here the limitations of the scale experiments and the most important laboratory errors are discussed. The reader should be aware of the most important experimental errors in the performed tests.

Limitations of the scale experiments

1. *Lateral velocity gradients*. This thesis is concerned with shallow shear flows that contains the confluence of parallel streams with a lateral velocity difference. This geometry is referred as Shallow Mixing Layer (SML). However, the lateral velocity differences in the field are the result of flow separation with the presence of horizontal recirculation cells.
2. *Constant and unidirectional flow.* In the scale experiments, the tidal influence on the scour development is completely ignored.
3. *Clear water scour.* The tests are considered as clear water scour. In practice, there is some upstream material supply. The influence of the upstream sediment supply has been neglected in the scale experiments.

Most important laboratory errors

First the inaccuracy in the experimental setup is regarded. Second, the velocity measurement inaccuracy to quantify the vertical flow structure in the scour hole during the test for the geometry of $B_{jet} = 40\ cm$ is considered.

One pipe is used to supply water from the recirculating pump system in the laboratory. As discussed in the experimental setup, the pipe supplies water in the inlet section, the water enters the flume through a flow straightener and it flows further downstream. However, the pipe is placed asymmetrically and the water does not enter the flume from the center. The pipe is placed more to the left side wall. The flow velocities were therefore relatively larger to the left side wall than elsewhere in the flume. These high flow velocities resulted in relatively larger scour depths to the left side wall. Nevertheless, it is stated that this experimental artifact has a minor impact on the results and conclusions in this present work. This experimental artifact is also minimal due to the fact that under lateral uniform flow the center of the flow is considered for the measurements. The asymmetry of the pipe is considered in Appendix C.

The velocity measurements to quantify the vertical flow state in the scour hole during the test for the geometry of $B_{jet} = 40\ cm$ are inaccurate. The vertical velocity profile should include measurements from one at the bed, two near the bed, one in the middle of the water column and one near the water surface. These positions were wrongly determined for the geometry $B_{jet} = 40\ cm$. The near bed velocities could not be determined properly. However, an indication of the vertical flow structure in the scour hole can be observed. One can compare the near-bed velocities in the scour holes for the other two geometries. Therefore, it is stated that the incorrect velocity measurements for one of the laterally nonuniformgeometries have a minimally affect the results and conclusions.

4 Results

This chapter presents the main results that were obtained from the laboratory experiments conducted in the Fluid Mechanics Laboratory at Delft University of Technology. First, the morphological results are shown. The bed measurements will include the presentation of the scour hole profile in time under lateral uniform flow and non-uniform flow. Furthermore, it will include the comparison between the obtained two-dimensional and three-dimensional scour results and computations based on the Breusers relation. Second, the flow velocity data is presented. By taking the local velocities and the turbulence into account, a better understanding of the underlying fundamental physical processes of the scour process could be achieved.

4.1 Scour

The scour development in time under lateral uniform and lateral non-uniform flow is presented. Figure 4.1 illustrates pictures of the experimental results. A review on the observed scour hole in the experiments are given further on in this section.

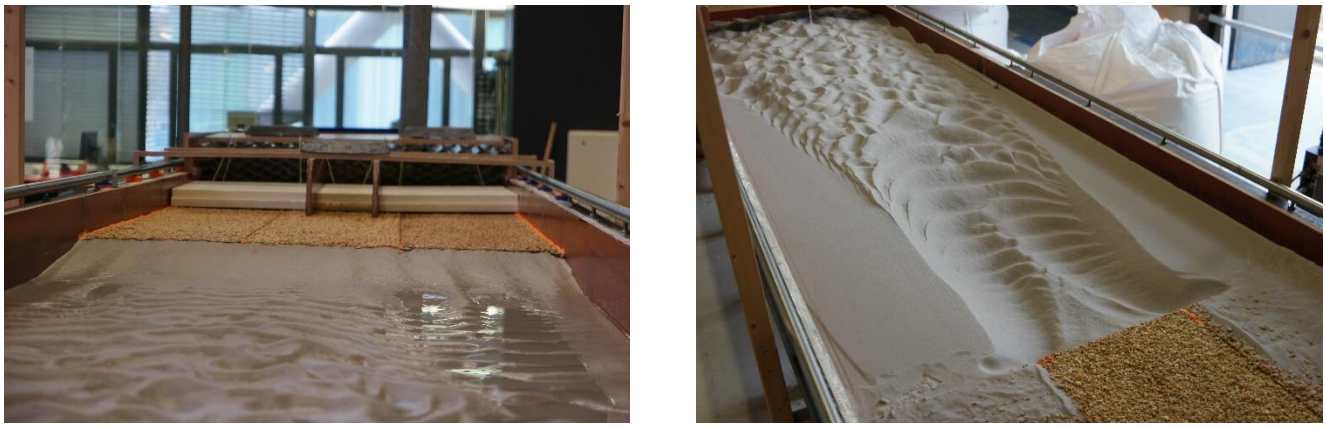

(a) (b)

Figure 4.1: Picture of experimental scour results. (a) Picture of scour hole for laterally uniform flow. (b) Picture of scour hole for laterally nonuniform flow.

Figure 4.2 shows the scour development under lateral uniform flow (case UF), whereas in Figure 4.6 and Figure 4.7 the scour development under lateral non-uniform flow (case NUF40 and NUF20) is presented. It should be mentioned that the figures concerning the scour hole profiles in time are averaged over $1\ cm$ for a smooth visualization of the noisy laser output signal.

Figure 4.2: Scour under lateral uniform flow.

In Figure 4.2 the development of the scour hole as function of time is given along the centerline. Figure 4.2 shows not only the scour hole depth increase in time, but also the movement of the point where the scour hole is at its maximum in downward direction in time. One can observe that the shape of the scour hole does not change in time. The ratio between the maximum scour depth and the distance from the end of the bed protection to the deepest point of the scour hole is more or less constant. Both the scour depth increase in time and the constant shape of the scour hole is in accordance with the development of a scour hole in the development phase as explained by for example Hoffmans & Verheij (1997). Furthermore, one can see that the bed profile is not always regular. Bedforms are clearly observed that mainly occur downstream of the scour hole. These bedforms are not only observed in the two-dimensional scour hole, but they are also observed in the three-dimensional scour holes, see Figure 4.6 and Figure 4.7. The bedforms are present in the area of interest, especially in the scour hole profile in laterally nonuniform flow. However, these bedforms are said to be not important in the context of this present scour research. These bedforms have not a significant influence in answering the research question concerning the comparison of the scour development under lateral uniform and lateral non-uniform flow. The maximum scour hole depths are determined. The determination of the maximum scour depth is discussed further in this subsection. The presence of bedforms could be important for other experimental research.

Before the scour development in time for the cases NUF40 and NUF20 is presented, Figure 4.3 illustrate the spatial bathymetry plot of the final situation. Both figures illustrate a surface plot of the bed elevation of case NUF40 and case NUF20 respectively in which (x, y) represent the spatial coordinates and z denotes the bed elevation. The surface plots present the bed elevation in space resulting from a bilinear interpolation based on the measured bed elevations along the predefined transects.

(a)

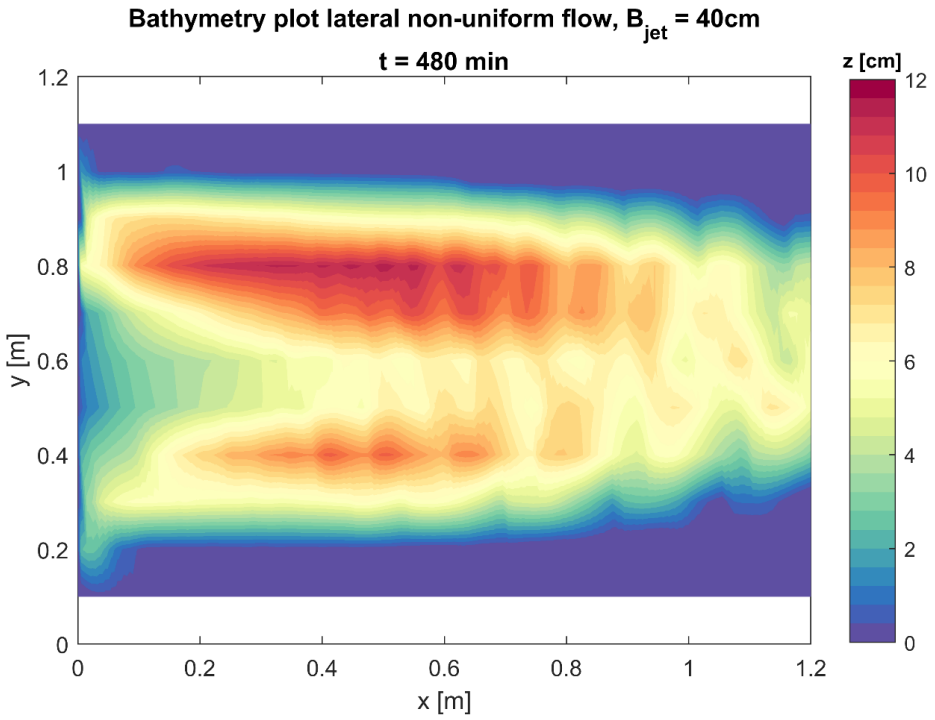

(b)

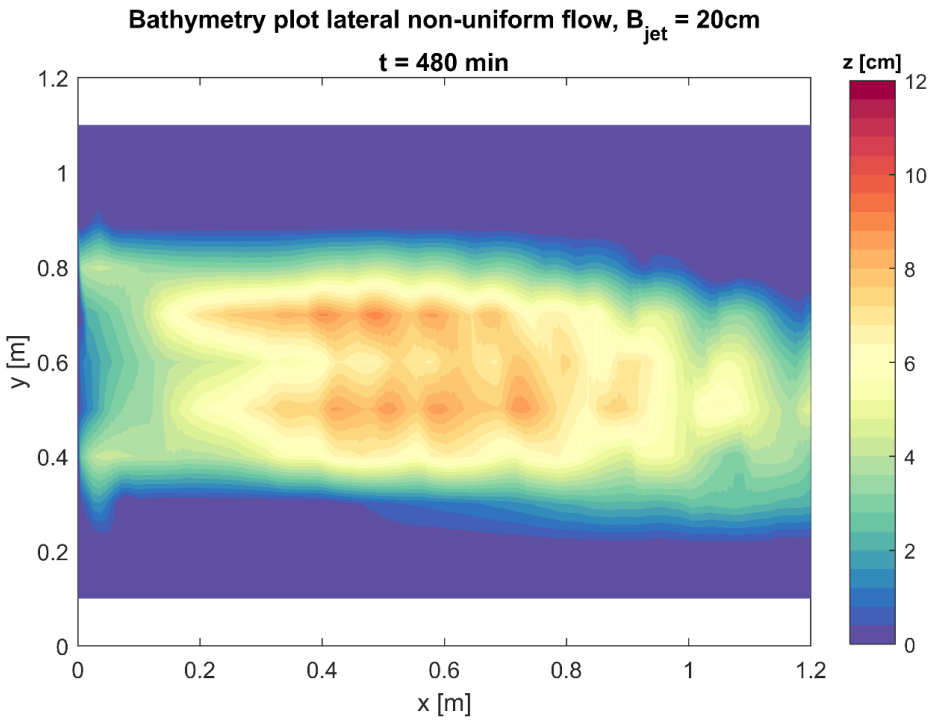

Figure 4.3: Scour under lateral non-uniform flow (a) $B_{jet} = 40\ cm$, the origin of the mixing layer lies on the transect $y = 40\ cm$ and $y = 80\ cm$ at $x = -1\ m$. (b) $B_{jet} = 20\ cm$. The origin of the mixing layer lies on the transect $y = 50\ cm$ and $y = 70\ cm$ at $x = -1\ m$.

The spatial plots of the three-dimensional scour in time are at least as important as the final situation. The spatial plots can give additional insight into the time development of the scour process. One can observe

that the maximum scour depth is more severe in the mixing layer region in the final situation for both the laterally nonuniform cases. Figure 4.4 illustrates that the maximum scour depth in time for case NUF40 is at the first measurements onwards larger in the mixing layers. However, Figure 4.5 shows for case NUF20 it seems that the maximum scour depth is initially larger in the main flow. After $t = 60\ min$, the larger maximum scour depths are clearly observed in the mixing layers. The difference in the initial scour pattern for the two laterally nonuniform flow cases cannot be explained. The additional surface plot results are given in Appendix D.

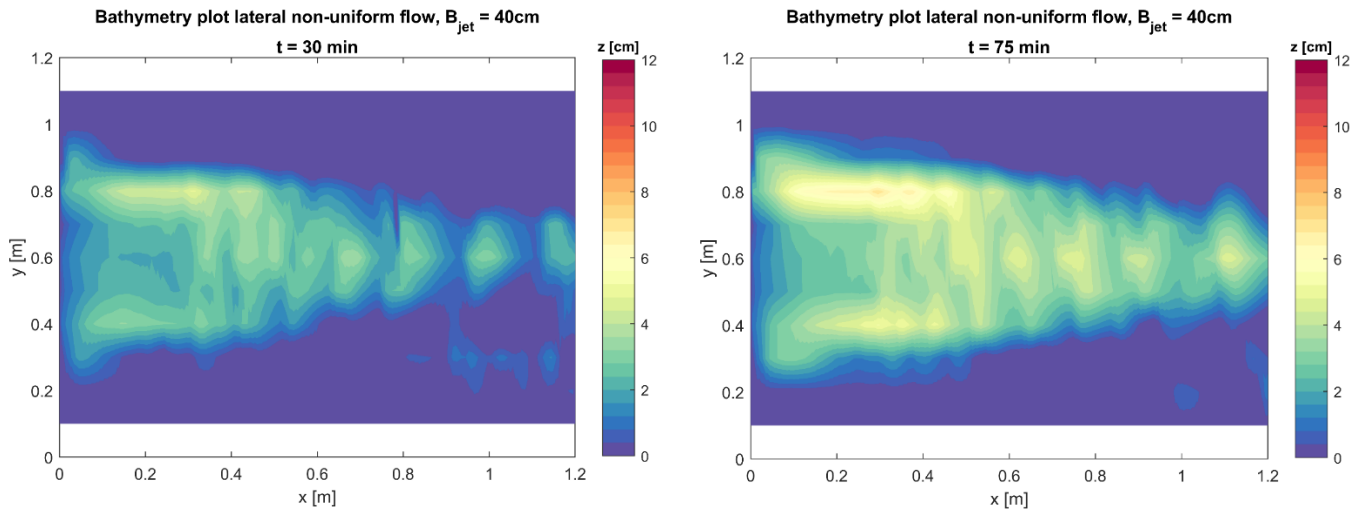

Figure 4.4: Scour under lateral non-uniform flow $B_{jet} = 40\ cm$ for $t = 30, 75\ min$.

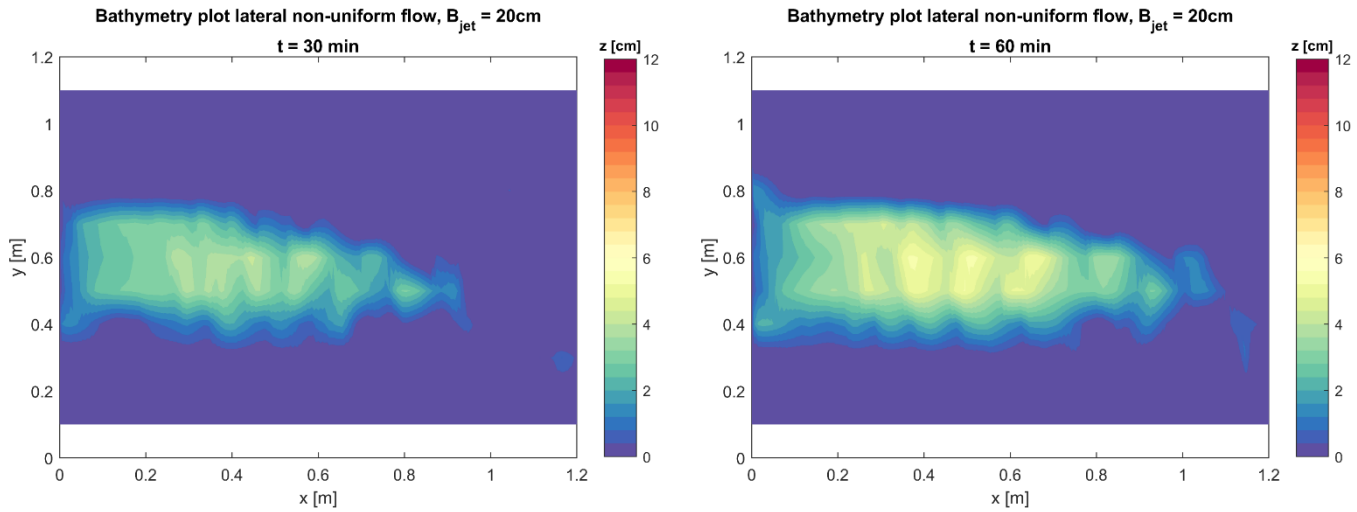

Figure 4.5: Scour under lateral non-uniform flow $B_{jet} = 20\ cm$ for $t = 30, 60\ min$.

These bathymetry plots help to interpret the three-dimensional scour development in time given in Figure 4.6 and Figure 4.7.

The described flow conditions have resulted in the formation two scour holes (or one scour hole with two maximum scour depths over the cross-section). Figure 4.3 show that the scour depths are more significant under the mixing layers than in the main flow (or in the centerline), despite the fact that the flow velocities were higher in the main flow. The most obvious reason for the aforementioned is the turbulence, as the other hydraulic boundary conditions were more or less the same. One is referred to section 4.2 including the velocity and turbulence measurements in this present work for the understanding of the presented scour pattern. Furthermore, one can observe that the most severe scour in both cases are along the transects of the origin of the mixing layers. For the case NUF40, the origin of the mixing layers as well as the most severe scour depths are along the transect $y = 40\ cm$ and $y = 80\ cm$. For the case NUF20, the origin of the mixing layers as well as the most severe scour depths are along the transects $y = 50\ cm$ and $y = 70\ cm$. In like manner, one is referred to the velocity and the turbulence measurements in section 4.2 for the understanding of the spatial variability of the scour development.

Figure 4.3 show not only similarities of the two lateral non-uniform cases as mentioned above, but also differences compared to each other. The maximum scour depths are different for the two lateral non-uniform cases for example. The maximum scour depths are more severe for the NUF40 case than for the NUF20 case. In addition, one can observe that the scour pattern in case NUF20 is more symmetrical compared to the unsymmetrical scour pattern in case NUF40. Figure 4.3 shows that the maximum scour depth in the left mixing layer $(y = 80\ cm)$ is more severe compared to the maximum scour depth in the right mixing layer $(y = 40\ cm)$. The unsymmetrical scour pattern in case NUF40 is probably the result of an unsymmetrical flow. The flow velocity at the left low velocity zone was apparently unequal to the flow velocity in the right low velocity zone during the experiment. The velocity differences over the left mixing were presumably different to the velocity differences over the right mixing layer.

Figure 4.6 and Figure 4.7 presents the scour development as function of time along three characteristic transects, namely along the two mixing layers and the centerline. One can observe that in general the presented scour hole profiles are more irregular compared to the two-dimensional bed profile. Bedforms are clearly observed and they do not occur only downstream the scour hole in contrast to Figure 4.2. The bed forms occur at the upstream scour slope and even at the deepest points of the scour hole. The maximum scour depths for the two- and three-dimensional scour are presented in subsection 4.1.1.

It should be note that the scour hole profile in time for the NUF40 case for transect $y = 80\ cm$ is interesting because, the scour hole profile in time for the NUF40 case for transect $y = 80\ cm$ shows a different behavior concerning the movement of the deepest point. The deepest point of the scour hole does not move in downstream direction. One can notice that the deepest point of the scour hole actually moves in upstream direction towards the bed protection in time. Eventually, the maximum scour depth in the case NUF40 on transect $y = 80\ cm$ is closer to the bed protection. Neither the scour hole profile on the other transects in case NUF40 or the scour hole profile in case NUF20 does not show the movement of the maximum scour depth in upstream direction. One can say that the maximum scour hole depth in case NUF20 and in case NUF40 on transect $y = 40\ cm$ and $y = 60\ cm$ moves also in downstream direction similar as in case UF. It is not clear why the deepest point of the scour hole moves in the direction of the bottom protection in the case NUF40 on transect $y = 80\ cm$.

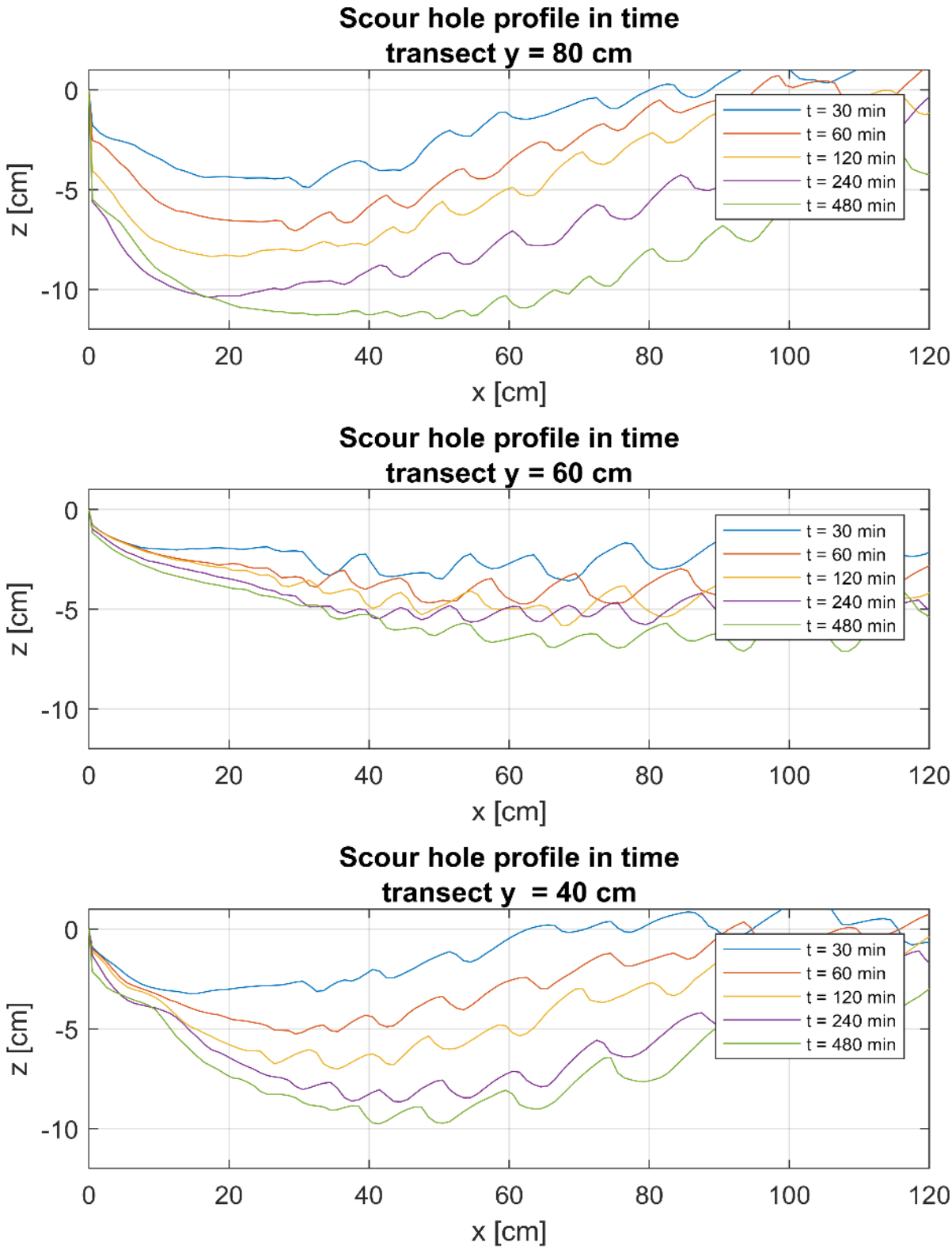

Figure 4.6: Scour development in time for case NUF40 along the center of the mixing layer (transect $y = 40\ cm, y = 80\ cm$) and along the centerline ($y = 40\ cm$).

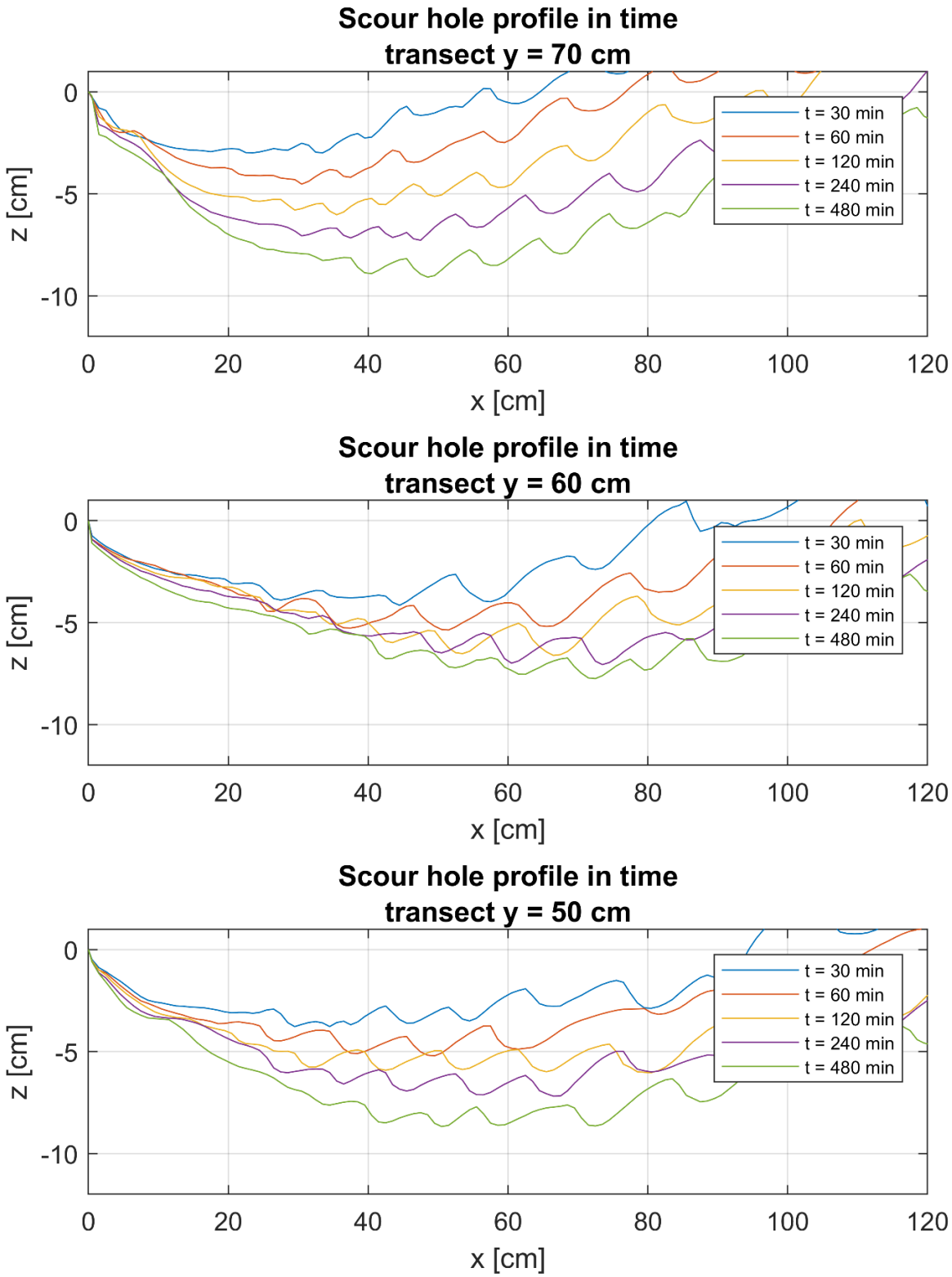

Figure 4.7: Scour development in time for case NUF20 along the center of the mixing layer (transect $y = 40\ cm,\ y = 80\ cm$) and along the centerline ($y = 40\ cm$).

As one could see in Figure 4.6 and Figure 4.7, it is not always possible to measure one maximum scour depth for the three-dimensional scour along the different cross-sections as mentioned before. The shape of the three-dimensional scour hole is not regular in some cases due to the bedforms. In order to have one value for the maximum scour depth in time, the bedforms are visually averaged. It is stated that the determination of the maximum scour depth in this way is sufficient. Figure 4.8 presents the three-dimensional scour hole profile along a cross-section with the determined maximum scour depth values for two different times as the averaged value of the bedforms as an example.

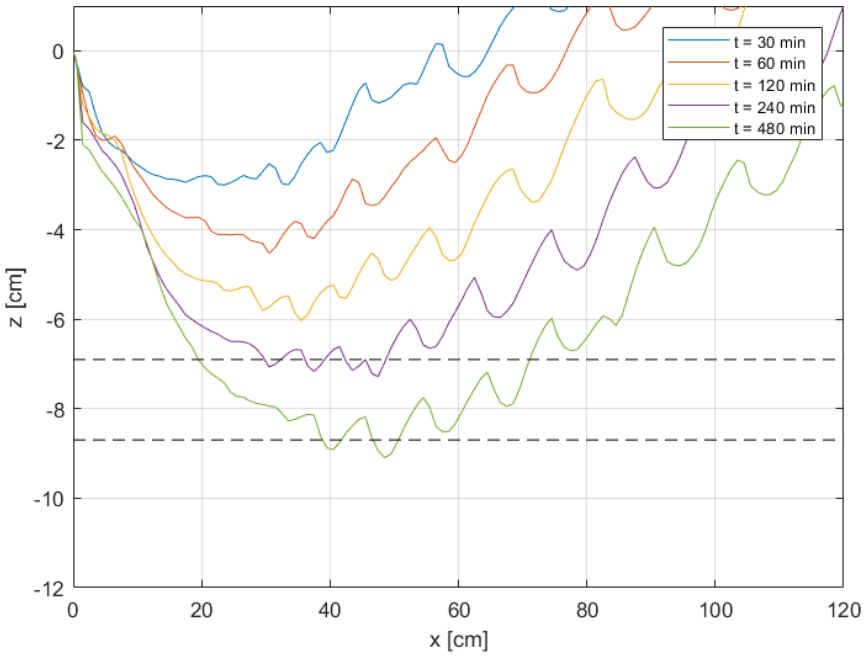

Figure 4.8: Scour hole profile in time with the determined maximum scour depth; as example scour hole profile, $B_{jet} = 20\ cm$ on $y = 70\ cm$.

4.1.1 The maximum scour depths

Figure 4.9 presents both the two-dimensional and the three-dimensional experimental maximum scour results as function of time. Table 4-1 shows the numerical value of the measured scour depths. Two different geometries were tested as three-dimensional scour, namely the geometry in which the width of the jet is $B_{jet} = 40\ cm$ and in which the width of the jet is $B_{jet} = 20\ cm$. The locations of the maximum scour depths along the cross-section were different for these two geometries. The maximum scour depths along the characteristic transects are given both in Figure 4.9 and Table 4-1.

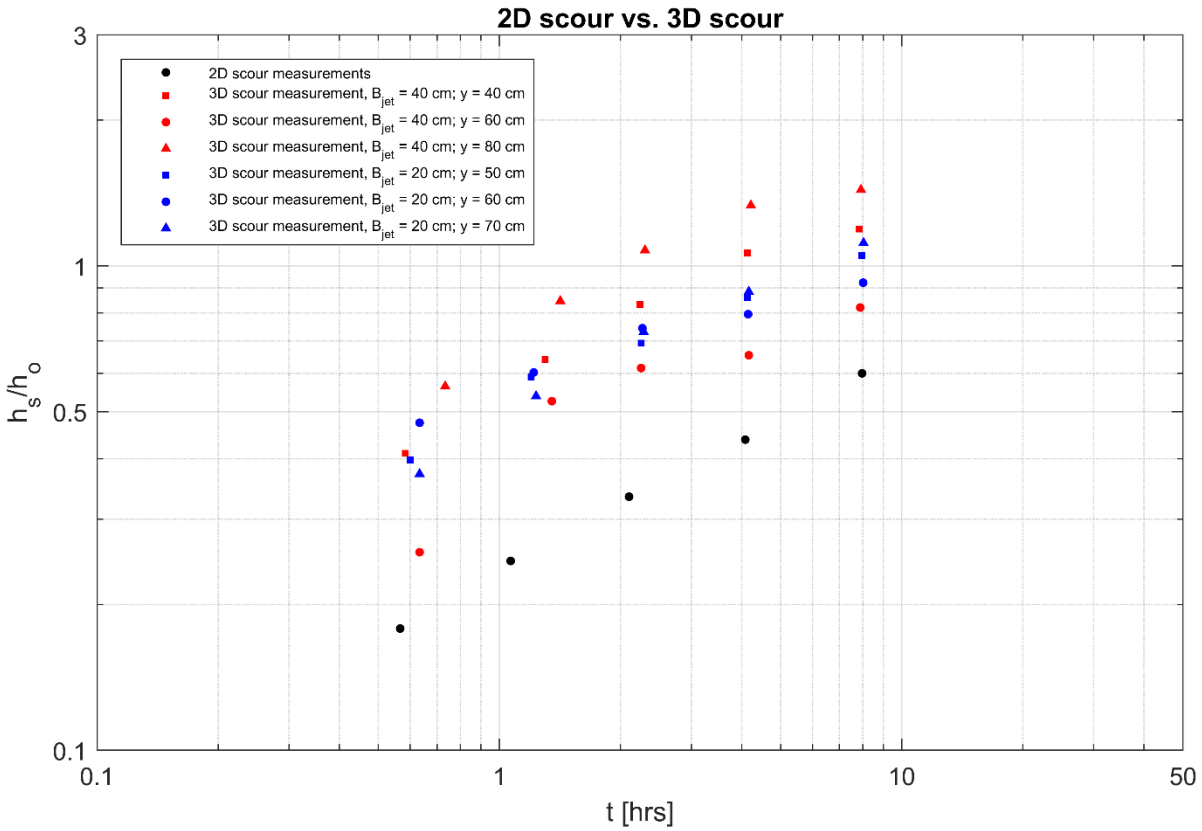

Figure 4.9: The scour measurements as function of time.

The maximum scour depths of the two-dimensional scour in time are given on the centerline, whereas the maximum scour depths of the three- dimensional scour in time is presented on three transects. For NUF40, the maximum scour depths on the transects $y = 40, 60 \text{ and } 80\ cm$ and for NUF20 on the transects $y = 40, 50 \text{ and } 70\ cm$ are presented. It can clearly be observed that the three-dimensional scour is more severe than the two-dimensional scour. The experiments showed that the maximum scour hole depth under non-uniform flow conditions at some locations in the cross-section were two to three times the maximum scour depth under uniform flow conditions.

2D scour		
	$y = 60\ cm$	
	$h_s\ (t = 30\ min) = 1{,}3\ cm$	
	$h_s\ (t = 60\ min) = 1{,}8\ cm$	
	$h_s\ (t = 120\ min) = 2{,}5\ cm$	
	$h_s\ (t = 240\ min) = 3{,}2\ cm$	
	$h_s\ (t = 480\ min) = 4{,}4\ cm$	
3D scour, $B_{jet} = 40\ cm$		
$y = 40\ cm$	$y = 60\ cm$	$y = 80\ cm$
$h_s\ (t = 30\ min) = 3{,}2\ cm$	$h_s\ (t = 30\ min) = 2{,}0\ cm$	$h_s\ (t = 30\ min) = 4{,}4\ cm$
$h_s\ (t = 60\ min) = 5{,}0\ cm$	$h_s\ (t = 75\ min) = 4{,}1\ cm$	$h_s\ (t = 60\ min) = 6{,}6\ cm$
$h_s\ (t = 120\ min) = 6{,}5\ cm$	$h_s\ (t = 120\ min) = 4{,}8\ cm$	$h_s\ (t = 120\ min) = 8{,}4\ cm$
$h_s\ (t = 240\ min) = 8{,}2\ cm$	$h_s\ (t = 240\ min) = 5{,}1\ cm$	$h_s\ (t = 240\ min) = 10{,}4\ cm$
$h_s\ (t = 480\ min) = 9{,}3\ cm$	$h_s\ (t = 480\ min) = 6{,}4\ cm$	$h_s\ (t = 480\ min) = 11{,}2cm$
3D scour, $B_{jet} = 20\ cm$		
$y = 50\ cm$	$y = 60\ cm$	$y = 70\ cm$
$h_s\ (t = 30\ min) = 3{,}1\ cm$	$h_s\ (t = 30\ min) = 3{,}7\ cm$	$h_s\ (t = 30\ min) = 2{,}9\ cm$
$h_s\ (t = 60\ min) = 4{,}6\ cm$	$h_s\ (t = 60\ min) = 4{,}7\ cm$	$h_s\ (t = 60\ min) = 4{,}2cm$
$h_s\ (t = 120\ min) = 5{,}4\ cm$	$h_s\ (t = 120\ min) = 5{,}8\ cm$	$h_s\ (t = 120\ min) = 5{,}7\ cm$
$h_s\ (t = 240\ min) = 6{,}7\ cm$	$h_s\ (t = 240\ min) = 6{,}2\ cm$	$h_s\ (t = 240\ min) = 6{,}9\ cm$
$h_s\ (t = 480\ min) = 8{,}2\ cm$	$h_s\ (t = 480\ min) = 7{,}2\ cm$	$h_s\ (t = 480\ min) = 8{,}7\ cm$

Table 4-1: Table with numerical values of maximum scour depths.

4.1.2 Characteristic time scale

As discussed in section 2.2, the characteristic time is equally applicable to two-dimensional scour as for three-dimensional scour. However, the characteristic time is not constant at each cross-section for three-dimensional scour (Hoffmans & Verheij, 1997). The characteristic time t_1 has been determined as the time scale in which the scour hole depth equals the water depth. The line of best fit which is based on the smallest root mean square error (RMSE) between fit and experimental data have resulted in a characteristic time t_1 for the two-dimensional scour and for the three-dimensional scour at different transects. Table 4-2 gives the characteristic time t_1 based on the intersection of the line of best fit with $y_m/h_0 = 1$ of the scour measurements in Figure 4.9. The characteristic time t_1 can also be determined by Equation 2.5 based on the velocity measurements. The calculated characteristic time t_1 is also been presented in Table 4-2.

	2D scour	**3D scour, $B_{jet} = 40\ cm$**			**3D scour, $B_{jet} = 20\ cm$**		
	$y = 60\ cm$	$y = 40\ cm$	$y = 60\ cm$	$y = 80\ cm$	$y = 50\ cm$	$y = 60\ cm$	$y = 70\ cm$
$\boldsymbol{t_1}$ [measured]	$26.3\ hrs$	$3.1\ hrs$	$13.2\ hrs$	$1.9\ hrs$	$6.1\ hrs$	$10.4\ hrs$	$5.2\ hrs$
$\boldsymbol{t_1}$[calculated]	$42.9\ hrs$	-	$88.5\ hrs$	-	-	$44.3\ hrs$	-

Table 4-2: Characteristic time in present work.

In this present work, only the characteristic time for the two-dimensional scour and the three-dimensional scour in the centerline can be calculated based on the measurements on top of the bed protection. The depth-averaged velocities and depth-averaged turbulence were only measured in the centerline and not along different transects. Therefore, no characteristic time t_1 other than in the centerline could have been determined. Table 4-2 demonstrates lower values for the measured characteristic time than for all the calculated characteristic times. The characteristic time of the two-dimensional scour and three-dimensional scour in the centerline of $t_1 = 43\ hrs, t_1 = 88\ hrs$ and $t_1 = 42\ hrs$ respectively has been calculated based on the material characteristics, the hydraulic conditions and the measured depth-averaged values presented in Table 3-1, Table 3-3 and Table 4-3 respectively. The calculated characteristic times for two-dimensional scour as for three-dimensional scour in the center are significantly higher than the measured characteristic times. It can be concluded that in this present work the calculated characteristic time based on Equation 2.5 overestimates the characteristic time based on the measurement data. It can also be concluded that the predictability of the time scale of scour development is difficult. Note that the degree of the degree of turbulence and the flow velocities determine the characteristic time scale to a large extent.

4.1.3 Coefficient γ

The maximum scour depth as function of time can be described by the Breusers method (Hoffmans & Verheij, 1997). Figure 4.10 shows the measured maximum scour depths of the two-dimensional scour including a curve fit through the data points. As for the determination of the time scale, the line of the best fit is based on the smallest RMSE between the fit and the experimental data. Furthermore, it should be mentioned that the line of the best fit is based on the experimental data for $t/t_1 < 1$ and $y_m/h_0 < 1$. Figure 4.10 presents the maximum scour depth over the initial water depth as function of the time over the characteristic time. One can determine the coefficient γ based on the measured maximum scour depths for $t < t_1$ as the slope of the fitted line in the log-log graph. The depth measurements are fitted by a power function of the form $f(x) = a \cdot x^{\,b}$. The exponent in the power function is at the same time the slope of this line in a log-log graph. So, the determined exponent is the coefficient γ of the Breusers-time dependent scour relation. In this present work, the value of the coefficient γ is approximately $\gamma = 0.4$ for the two-dimensional scour.

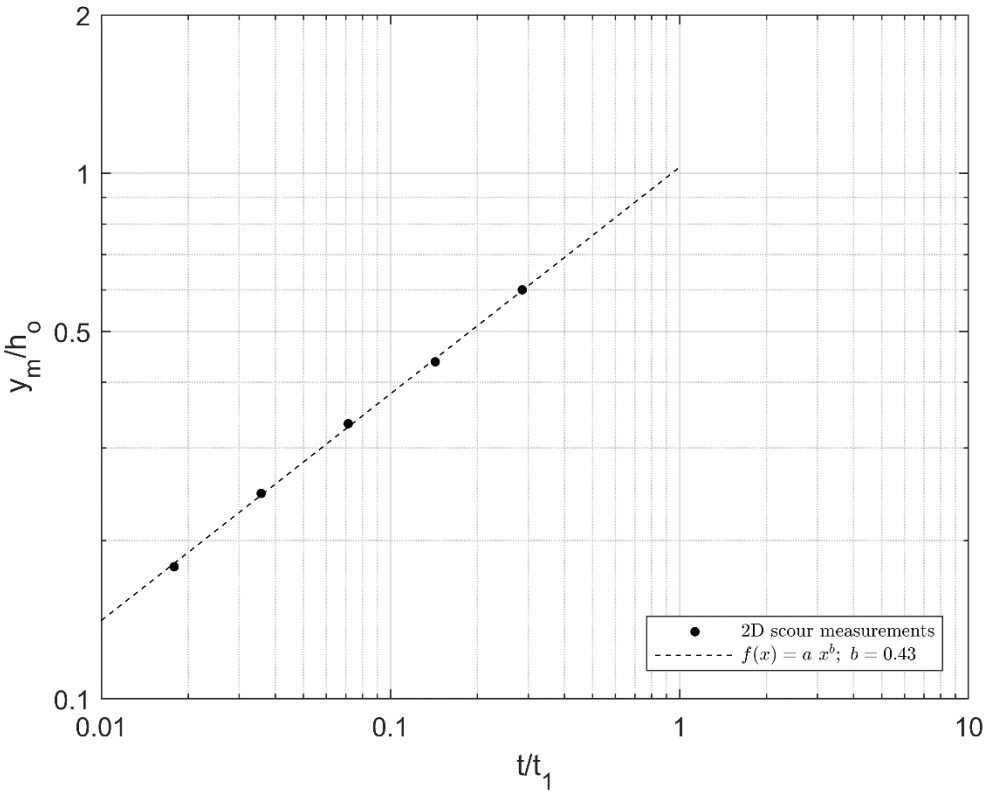

Figure 4.10: 2D scour measurement vs. gamma values

Similarly, the measured maximum scour depths of the three-dimensional scour are presented against the empirical scour relation of Breusers. The maximum scour depths over the initial water depth as function of the time over the characteristic time are presented. As the flow conditions are more or less the same in the right and left mixing layers, the maximum scour depths are considered in one graph. Both Figure 4.11 and Figure 4.12 present the measurements and Breusers time-dependent relation for case NUF40. Figure 4.11 presents the measurements in the centerline in which the coefficient is $\gamma = 0.34$, while Figure 4.12 presents the measurement in the mixing layers in which $\gamma = 0.45$. Figure 4.13 and Figure 4.14 present the measurements of the case NUF20. The measurements in the center give a coefficient of $\gamma = 0.24$ and the measurements in the mixing layers give a coefficient $y = 0.40$.

As far as is known, the geometry in this present work has not been discussed elsewhere yet. The experimentally determined values of the coefficient γ in this present work is more or less in agreement with the different studies on the value of the coefficient γ for the prediction of the maximum scour depth as function of time for $t < t_1$ (Hoffmans & Verheij, 1997). In literature it is stated that the coefficient γ should be in the range $\gamma = 0.27 - 0.4$ for two-dimensional flow conditions and $\gamma = 0.4 - 0.8$ for three-dimensional flow conditions. The values of $\gamma = 0.4$, $\gamma = 0.24$ and $\gamma = 0.34$ respectively for the two-dimensional scour and the three-dimensional scour $B_{jet} = 40\ cm$ and $B_{jet} = 20\ cm$ both in the centerline corresponds reasonably with the range $\gamma = 0.27 - 0.4$ for two-dimensional flow conditions. The values of $\gamma = 0.54$ and $\gamma = 0.4$ based on the scour development in the mixing layers for both NUF40 and NUF20 case are in the range $\gamma = 0.4 - 0.8$ for three-dimensional flow conditions.

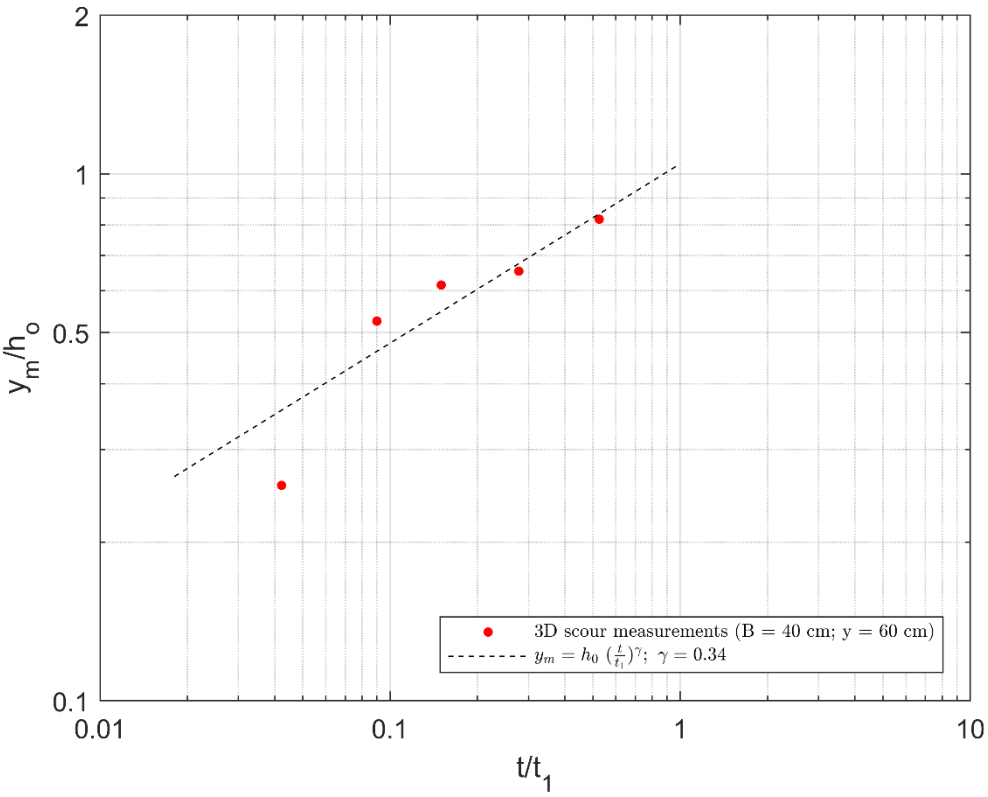

Figure 4.11: Measurements of 3D scour geometry $B_{jet} = 40\ cm$ on $y = 60\ cm$ and the Breusers time-dependent relation

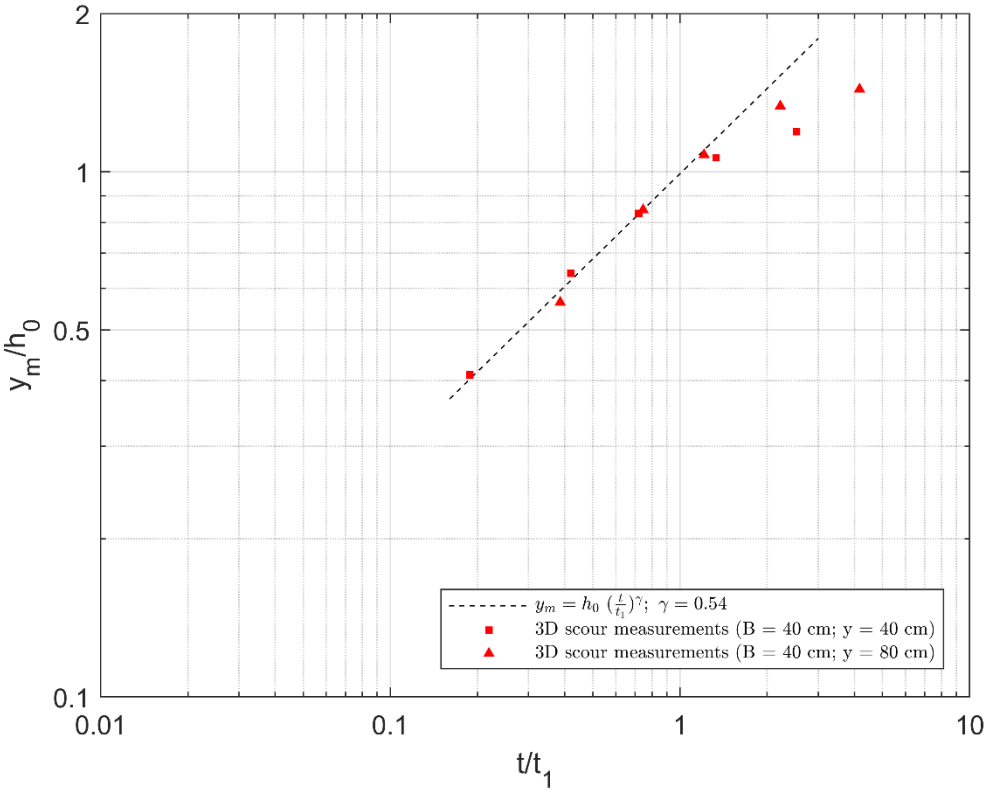

Figure 4.12: Measurements of 3D scour geometry $B_{jet} = 40\ cm$ on $y = 40, 80\ cm$ and the Breusers time-dependent relation.

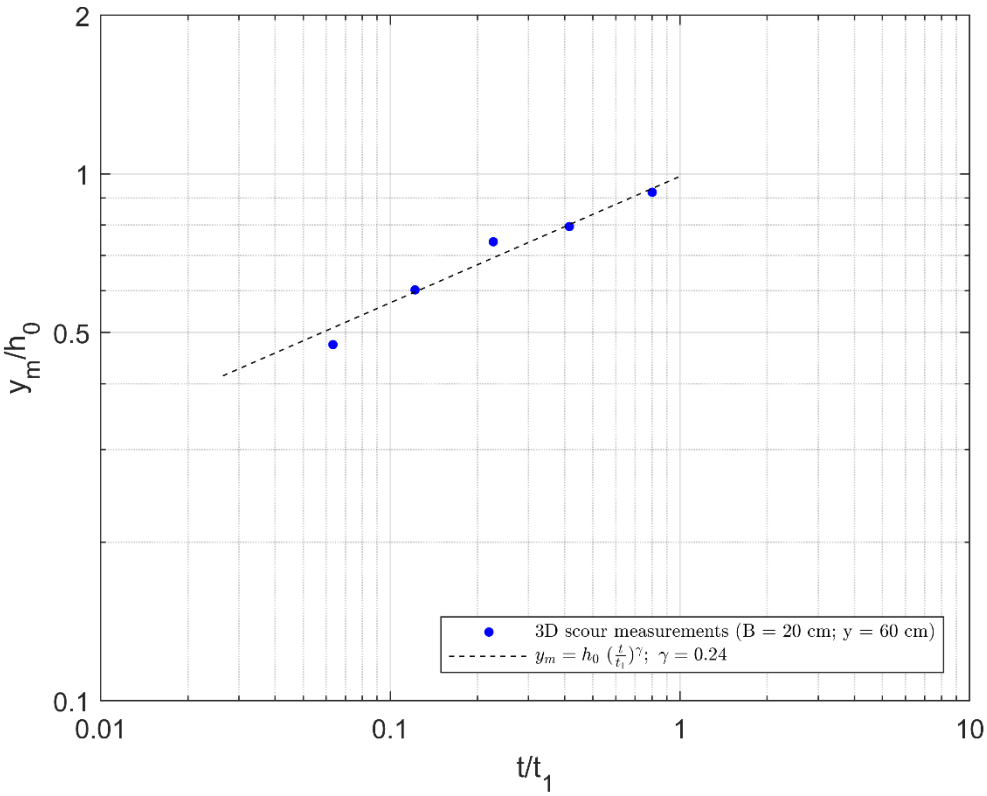

Figure 4.13: Measurements of 3D scour geometry $B_{jet} = 20\ cm$ on $y = 60\ cm$ and the Breusers time-dependent relation.

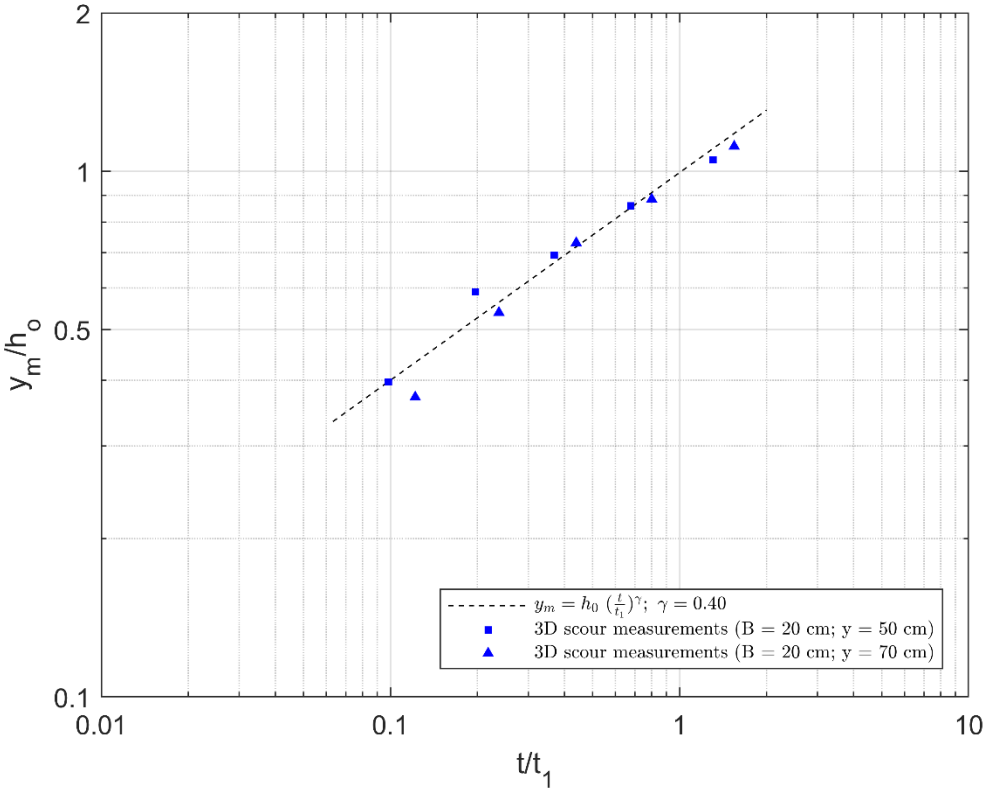

Figure 4.14: Measurements of 3D scour geometry $B_{jet} = 20\ cm$ on $y = 50,70\ cm$ and the Breusers time-dependent relation.

Furthermore, one can observe from Figure 4.12 and Figure 4.14 the decrease in the rate of development of the maximum scour depths in time for $t > t_1$. The decrease in rate of the development of the maximum scour depths is clearly be observed in Figure 4.12. The maximum scour depths in the mixing layers start to deviate from the empirical Breusers-time dependent line. The Breusers-time dependent relation cannot predict the maximum scour depths in the stabilization and equilibrium phase as discussed in the literature study.

4.1.4 Application of Breusers formula

For predicting the scour development in time, the Breusers formula is used. This section demonstrates the applicability of the Breusers empirical relation on the scour measurements. The experimental data is presented together with the calculated and fitted Breusers empirical relation. Two fits of the Breusers equation are included in each figure. One fit uses the γ coefficient and the calculated characteristic time t_1. The other fit uses both the γ coefficient and the measured characteristic time t_1 as the fitting constants.

Formula for scour development in development phase

Figure 4.15 presents the experimental data of the lateral uniform case with the calculated and fitted scour development. Figure 4.16 and Figure 4.17 shows the experimental data of the non-uniform cases with the calculated and fitted Breusers equation. It is possible to fit the scour measurements in time to the time-development of the scour process given by Breusers (1966).

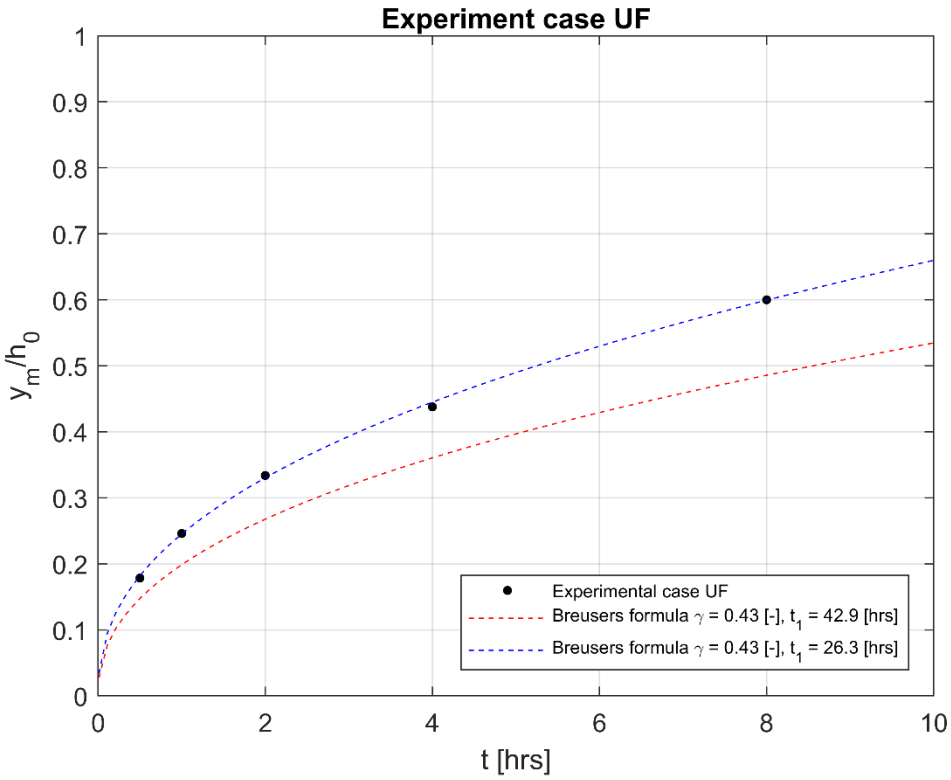

Figure 4.15: The Breusers formula on scour development in test lateral uniform flow with one and two fitting constants. The blue dashed line is the Breusers formula with to fitting constants.

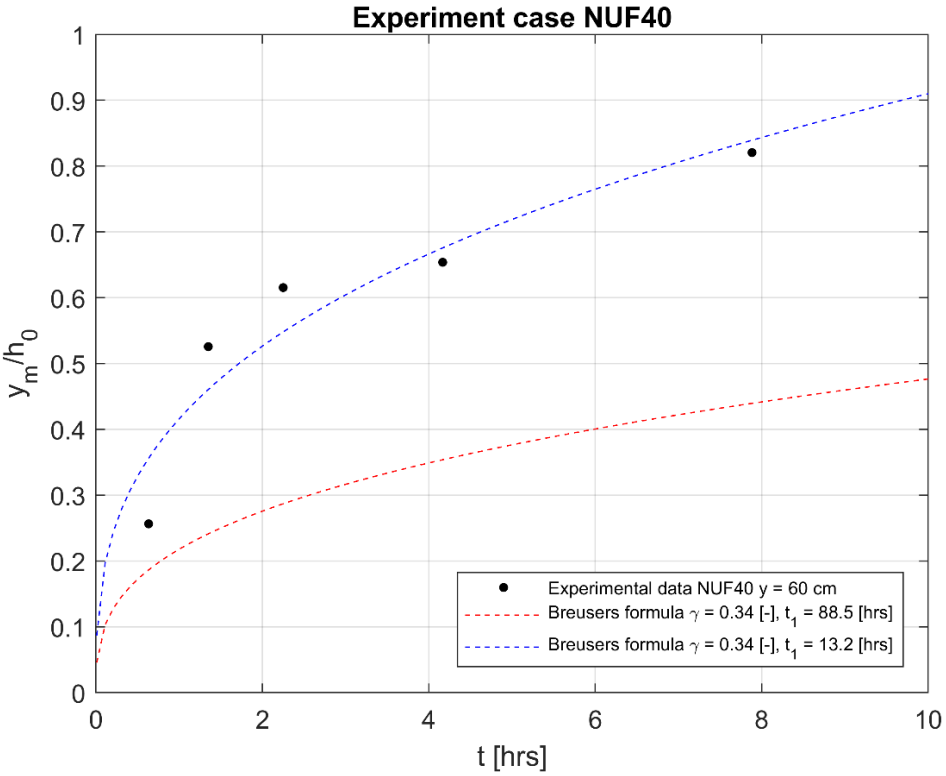

Figure 4.16: The Breusers formula on scour development in test lateral non-uniform flow $B_{jet} = 40\ cm$ with one and two fitting constants. The blue dashed line is the Breusers formula with to fitting constants.

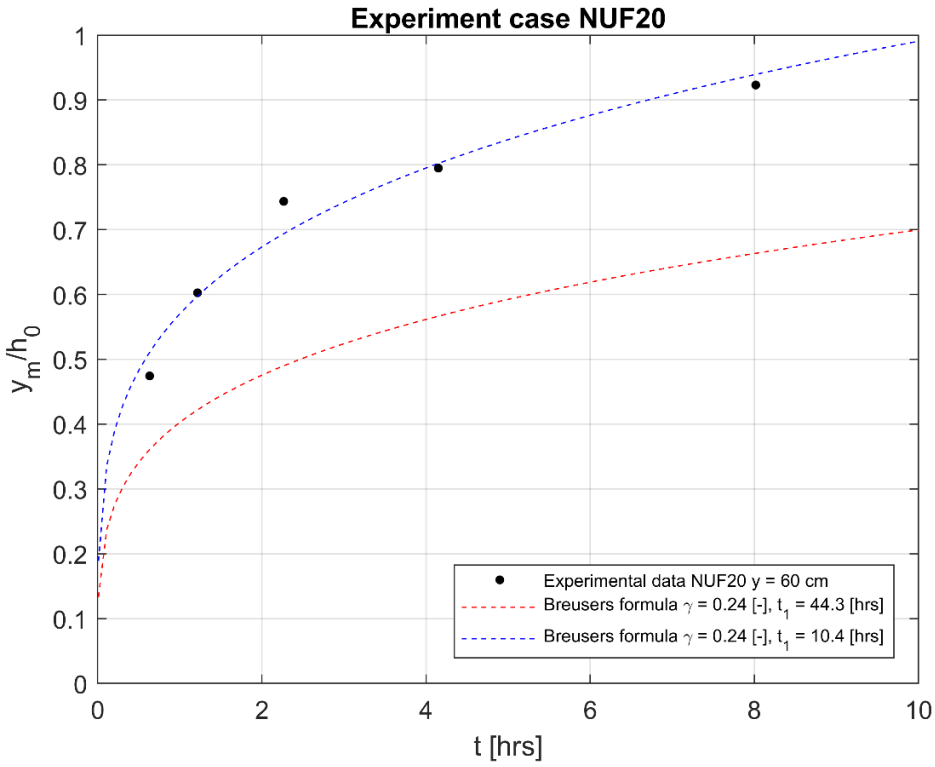

Figure 4.17: The Breusers formula on scour development in test lateral non-uniform flow $B_{jet} = 20\ cm$ with one and two fitting constants. The blue dashed line is the Breusers formula with to fitting constants.

4.2 Horizontal flow structure

The effect of horizontal non-uniformities in the approaching flow upstream of a scour hole on the hydrodynamic conditions in a scour hole is discussed in coming sections. Knowledge of these hydrodynamic conditions will contribute to the understanding of the fundamental processes in the development of scour holes under lateral non-uniform flows. The effect of the presence of lateral streamwise velocity differences on the horizontal structure of the flow at a location of a scour hole is presented in section 4.2. In section 4.3, the effect of the presence of lateral streamwise velocity differences on the vertical flow structure in the scour hole will be presented.

In order for a better understanding of the fundamental processes of the scour development and to explain the different scour pattern under lateral non-uniform flow, qualitative and quantitative measurements are performed. First, the visualization of the horizontal flow structures by injecting colored dye are shown. Second, the results of the velocity measurements are presented. The time-average flow velocity along different cross-sections in time and the depth-averaged flow velocity results in the jet center are considered.

4.2.1 Dye visualization

Dye visualization was used to reveal the horizontal flow structure at the location of the scour hole as a first step. The effect of the presence of lateral streamwise velocity differences on the horizontal flow structure can be observed. Figure 4.18 illustrates the flow for laterally uniform flow at different lateral locations near the start of the experiment and near the end of the experiment. As one can observe from Figure 4.18, the scour hole at the end of the experiment does not have an influence on the horizontal flow structure.

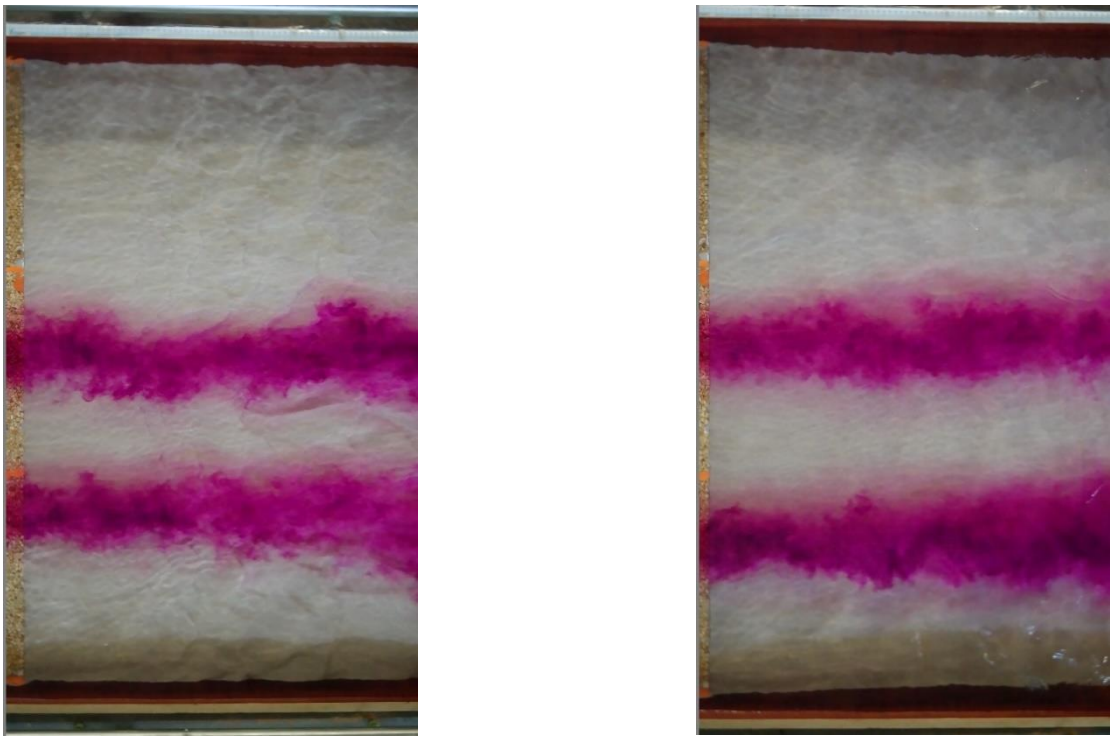

(a) (b)

Figure 4.18: Flow visualization for laterally uniform flow. (a) Dye injection near the start of the experiment. (b) Dye injection near the end of the experiment with a developed scour hole at the end of the bottom protection. The flow is from left to right.

Whereas inspection with dye shows a deflection of the horizontal mixing layer to the center of the flow for laterally nonuniformincoming flow in Figure 4.19. It shows dye injection in the center and in the right mixing layer. In addition, Figure 4.20 shows dye injection in both mixing layers, where one can observe the horizontal contraction of the flow in the scour hole.

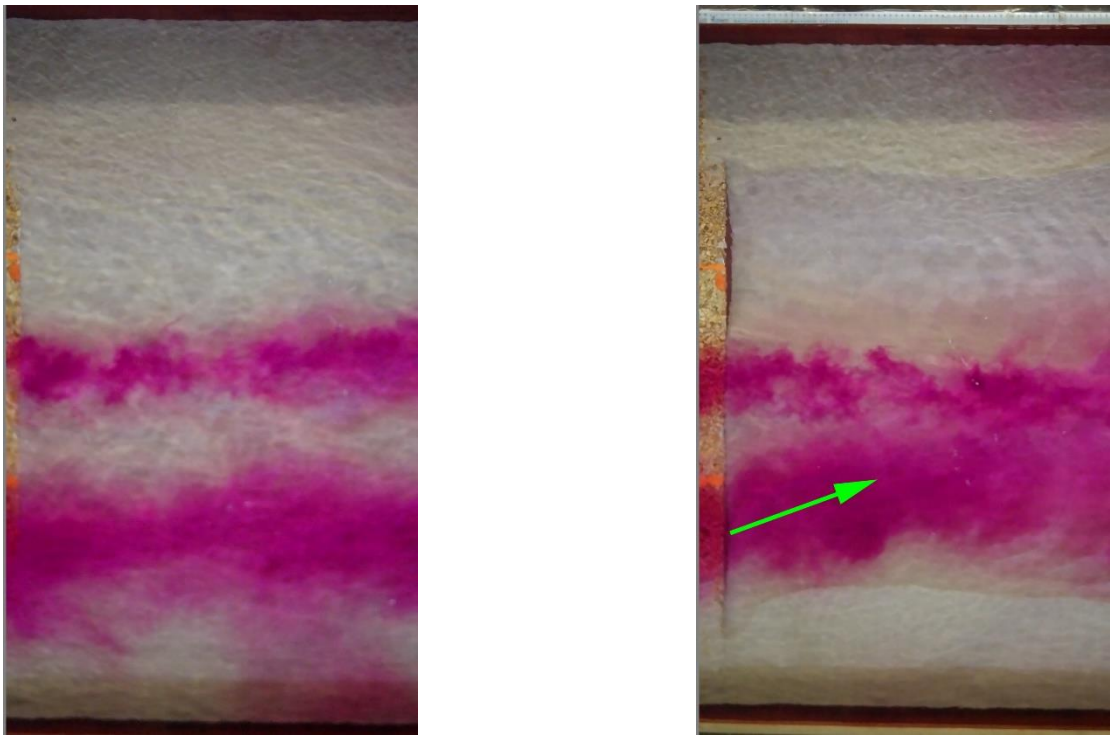

(a) (b)

Figure 4.19: Flow visualization for laterally nonuniform flow case NUF40. (a) Dye injection near the start of the experiment. (b) Dye injection near the end of the experiment with a developed scour hole. The flow is from left to right. The green arrow shows the deflection to the center of the jet.

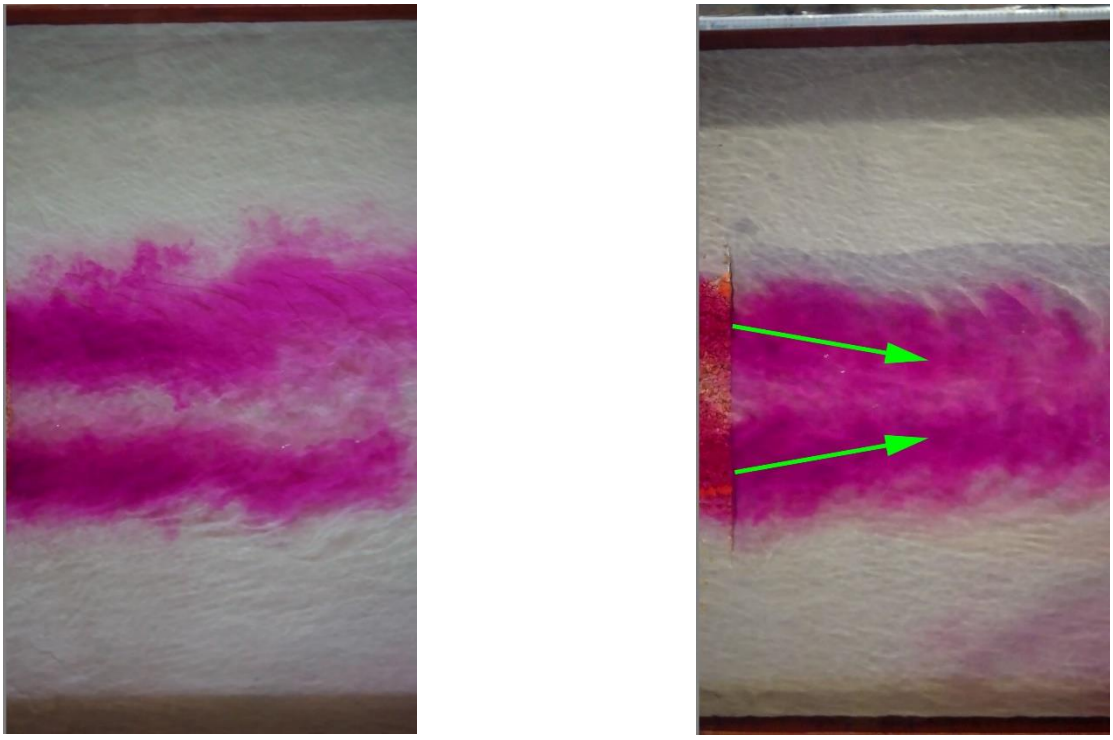

(a) (b)

Figure 4.20: Flow visualization for laterally uniform flow case NUF20. (a) Dye injection near the start of the experiment. (b) Dye injection near the end of the experiment with a developed scour hole. The flow is from left to right. The green arrows show a horizontal contraction of the flow in the scour hole.

4.2.2 Time-averaged flow velocities

Figure 4.21 presents the overview of the positions of the ADV measurements in the experiments. As discussed in subsection 3.4.3 the velocity measurements are only considered at half width based on symmetry. In addition, more velocity measurements are conducted along the cross-section for the laterally nonuniformcases because of the lateral streamwise velocity differences.

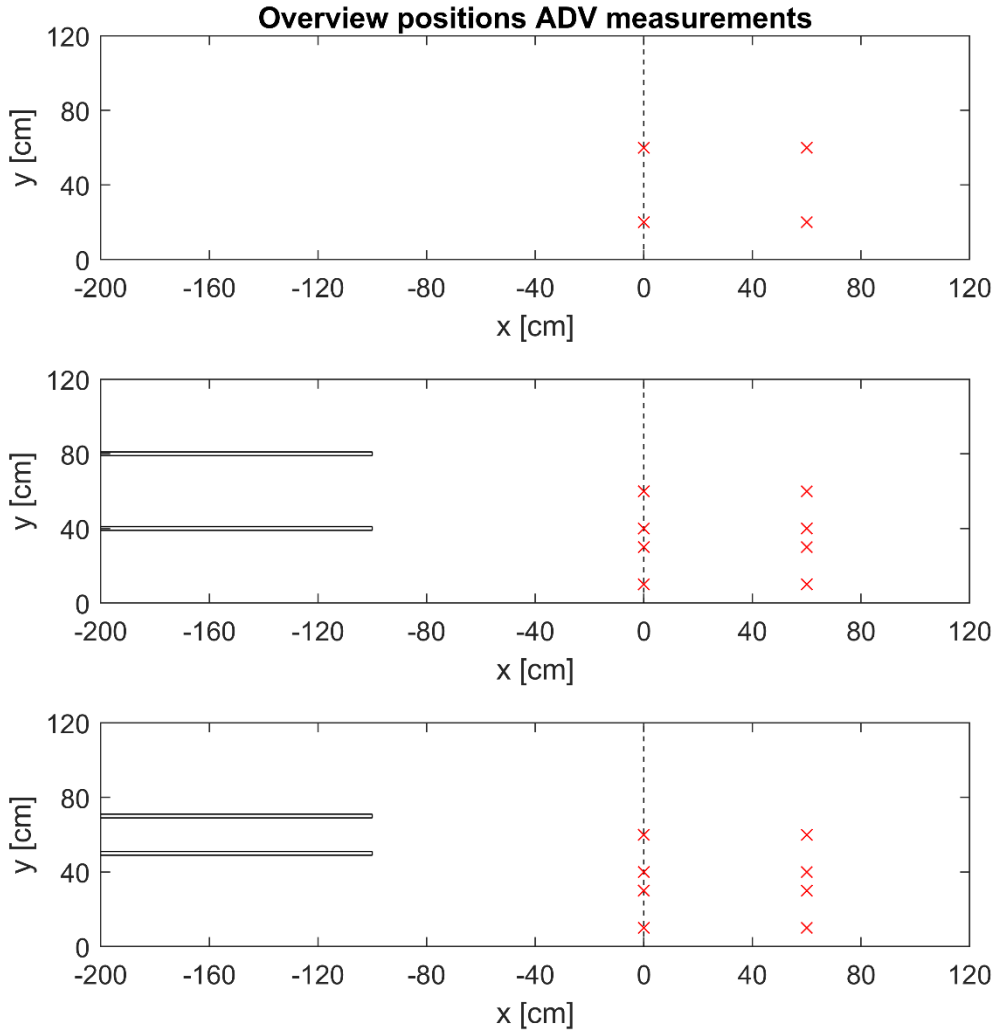

Figure 4.21: Overview of the positions of the ADV measurements for the horizontal flow structure. The ADV measurement points are indicated as red markers. The velocities are measured in time for $t = 0, 90, 180, 270\ min$. The x locations are at the transition of fixed bed and erodible bed and near the deepest point in the scour hole in time. The y locations are at $y = 20, 60\ cm$ for uniform flow and $y = 10, 30, 40, 60\ cm$ for non-uniform flow. The z location is at mid-depth of the initial water depth h_0. Note that the deepest point moves in x-direction, therefore the x locations of the measurements near the deepest point are not fixed in x coordinates. In this subplot, the x position of the deepest point is set on $x = 60\ cm$ as an example.

Figure 4.22 illustrates the time-averaged streamwise flow velocities in time. The following observations could be made from Figure 4.22:

1. The velocities near the right-side wall are higher than the velocities in the center under lateral uniform flow. This is probably related to an experimental artifact. This effect is minimal and it is stated that there are nearly lateral velocity differences across the uniform flow. The approach flow is more or less lateral uniform.

2. A significant decrease of the time-averaged flow velocity in the scour hole for $t = 360\ min$ as a result of the depth-increase in the laterally nonuniform flow $B_{jet} = 40\ cm$ compared to $B_{jet} = 20\ cm$. Furthermore, one can observe a decreased time-averaged flow velocity for $t = 360\ min$ at $x = 0$ in the laterally nonuniform flow $B_{jet} = 40\ cm$.

3. The time-averaged flow velocities for the laterally nonuniform flow at the sides are below the critical flow velocity. As presented in section 4, there is no erosion at the sides of the domain under laterally nonuniform flow as intended.

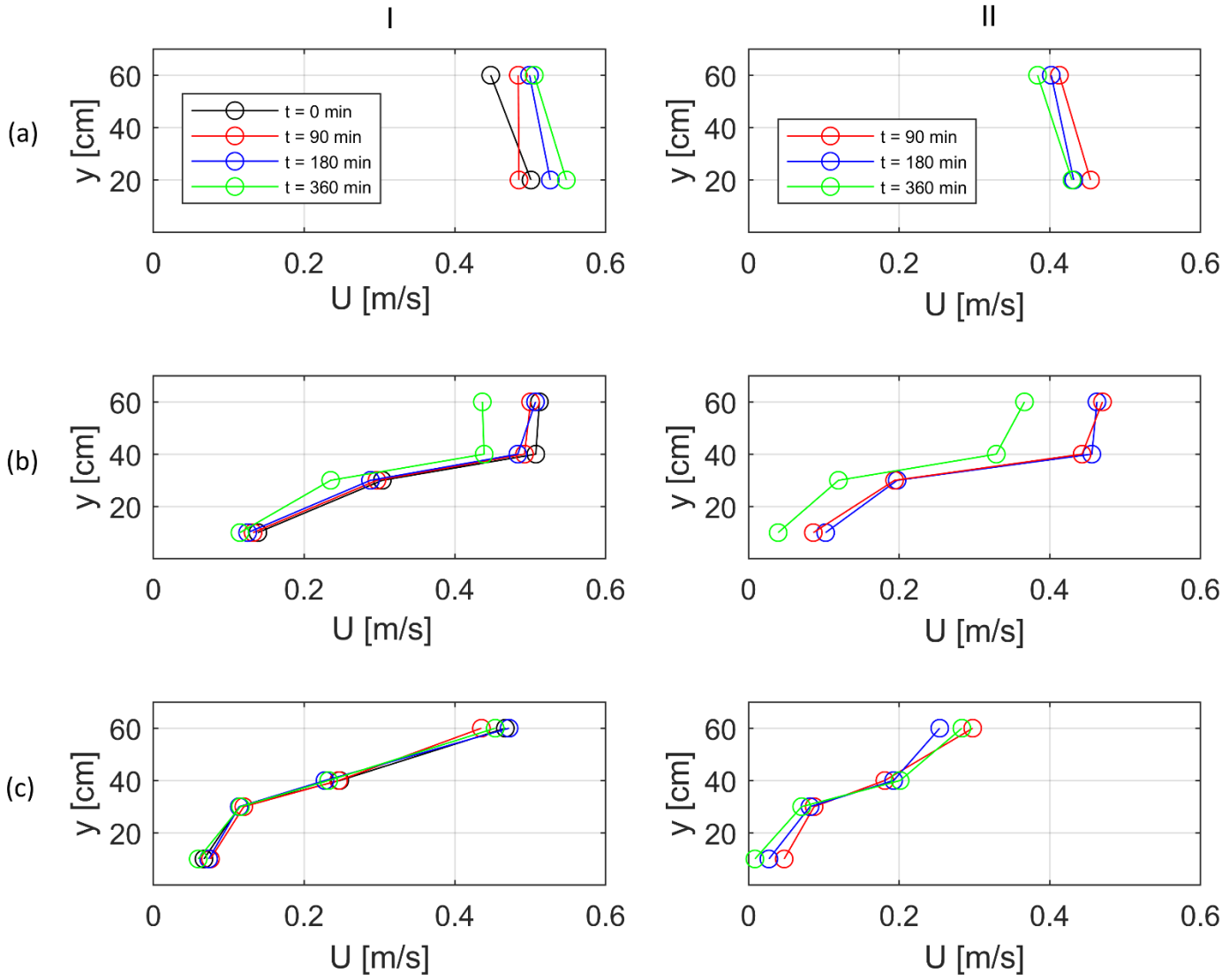

Figure 4.22: Profiles of the time-averaged streamwise velocities. The letters on the left side of the subplots represent the different flow conditions: (a) laterally uniform flow. (b) laterally nonuniform flow $B_{jet} = 40\ cm$. (c) laterally nonuniform flow $B_{jet} = 20\ cm$. The numbers above the subplots represent the x-coordinates: (I) at the transition between fixed and erodible bed, $x = 0$. (II) near the deepest point of the scour hole

Figure 4.22 shows also the important fact that although the highest flow velocities are observed in the main flow, the maximum scour depths under lateral non-uniform flow conditions are observed in the mixing layers as discussed in section 4. The time-averaged flow velocities could not explain the deeper maximum scour depths in the mixing layers under laterally nonuniform flow. Therefore, the turbulence is considered. The intense shear (turbulence) in the mixing layer might explain the maximum scour depths in the mixing layer and the spatial variability of the scour depths along the different transects. The reader is referred to Appendix B.1.3 for more detail about Reynolds shear stresses.

Figure 4.23 shows the horizontal Reynolds shear stresses τ_{xy} for uniform and non-uniform flow conditions at the bed protection ($x = 0\ cm$) and at the maximum scour hole depth in time along different transects. Figure 4.23 can explain the spatial variability of the scour development under lateral non-uniform flow as depicted in Figure 4.3. The horizontal Reynolds shear stress τ_{xy} could be associated with high turbulence.

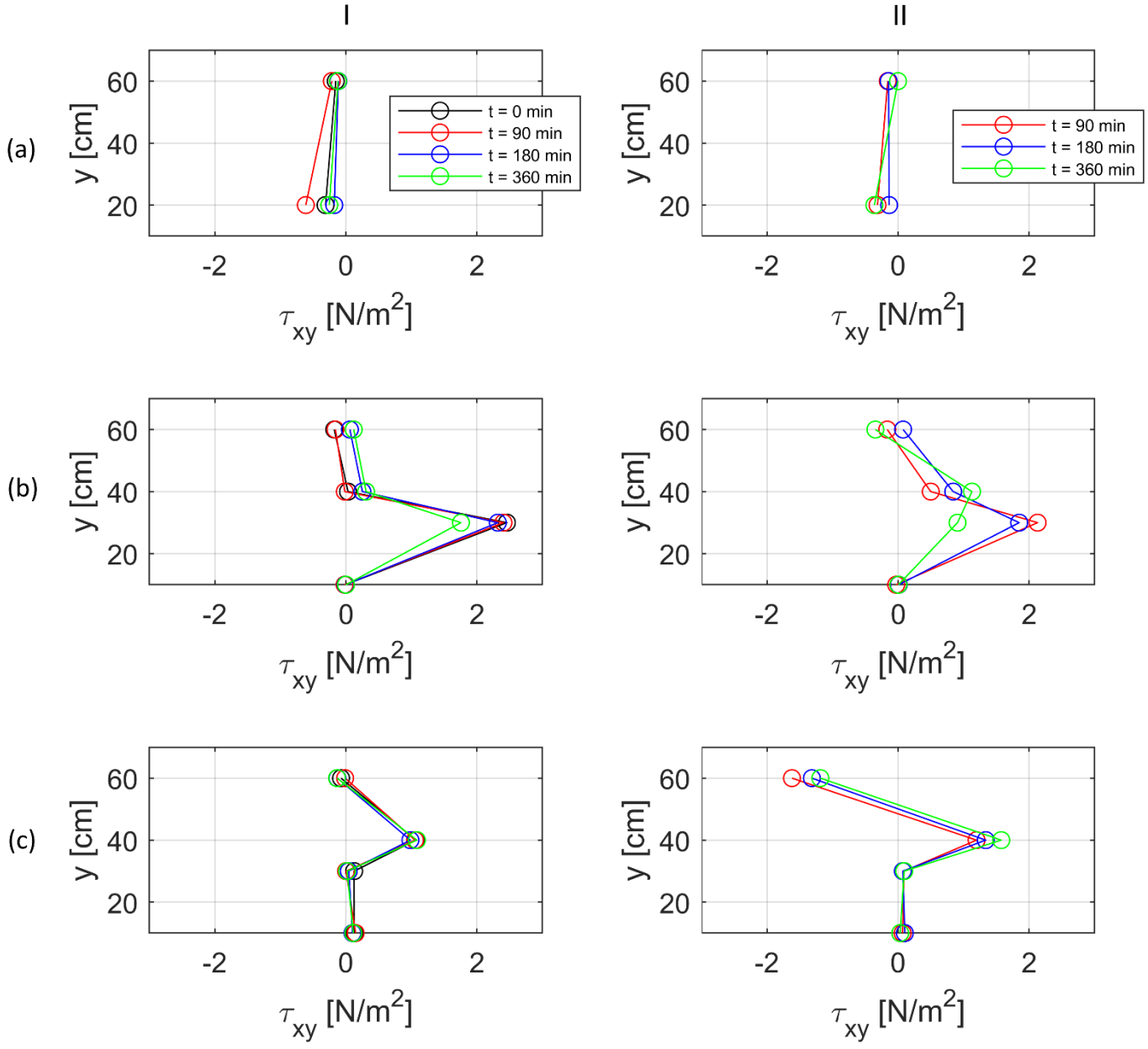

Figure 4.23: The Reynolds shear stress τ_{xy} for the different cases at two different streamwise coordinates. The letters on the left side of the subplots represent the different flow conditions: (a) laterally uniform flow. (b) laterally nonuniform flow $B_{jet} = 40\ cm$. (c) laterally nonuniform flow $B_{jet} = 20\ cm$. The numbers above the subplots represent the x-coordinates: (I) the Reynolds shear stress τ_{xy} at $x = 0$. (II) the Reynolds shear stress τ_{xy} near the deepest point of the scour at time t.

The following observations and are made from Figure 4.23:

1. There are nearly lateral velocity differences across the uniform flow. Therefore, the horizontal shear stresses under lateral uniform flow is about zero.

2. Figure 4.23 shows that the high values of τ_{xy} in laterally nonuniform flow are observed in the mixing layers.

For laterally nonuniform flow $B_{jet} = 40\ cm$ the highest values of τ_{xy} are on $y = 30\ cm$ at $x = 0$. The highest values of τ_{xy} is moved to the center to $y = 40\ cm$ near the deepest point of the scour hole for $t = 360\ min$. One observes that the horizontal Reynolds shear stress τ_{xy} on $y = 40\ cm$ increases in time, whereas τ_{xy} on $y = 30\ cm$ decreases in time at the deepest point in the scour hole.

For laterally nonuniform flow $B_{jet} = 20\ cm$ the highest values of τ_{xy} are on $y = 40\ cm$ at $x = 0$. The highest values of τ_{xy} near the deepest point of the scour hole does not move in lateral direction as for $B_{jet} = 40\ cm$. Contrary to the laterally nonuniform flow $B_{jet} = 40\ cm$, the horizontal Reynolds shear stress τ_{xy} in the scour hole on the transect with the highest values τ_{xy} at $x = 0$ $(y = 40\ cm)$ increases in time.

The observations concerning the high values of τ_{xy} might explain that the maximum scour depths are not observed in the main flow but in the mixing layers. To be more specific, the maximum scour depth for laterally nonuniform flow $B_{jet} = 40\ cm$ as well as the highest values of the horizontal Reynolds shear stress at $x = 0$ are observed on $y = 40\ cm$. For laterally nonuniform$B_{jet} = 20\ cm$, the maximum scour depth and the highest values of the horizontal Reynolds shear stress τ_{xy} at $x = 0$ are observed on $y = 30\ cm$.

The position of the highest values of the horizontal Reynolds shear stress τ_{xy} at $x = 0\ cm$ could be explained by the classical mixing layer theory over a flat bed as discussed in the literature study. A mixing layer develops between the high velocity zone and the low velocity zone. The mixing layer is characterized by a lateral shift of the center of the mixing layer to the low velocity zone. For laterally nonuniform flow $B_{jet} = 40\ cm$, the origin of the mixing layer is at $y = 40\ cm$ for $x = -100\ cm$. In this case, the center of the mixing layer has shifted towards $y = 30\ cm$ over a distance of 1 m. For laterally nonuniform flow $B_{jet} = 20\ cm$, the center of the mixing layer moves from the origin on $y = 50\ cm$ at $x = -100\ cm$ towards $y = 40\ cm$ at $x = 0\ cm$. However, the behavior of the lateral shift of the center of the mixing layer towards the high velocity zone above the scour hole for $B_{jet} = 40\ cm$ case is in contrast to the behavior of the classical mixing layer. The lateral shift towards the high velocity zone due to an increase in depth is not seen for the case $B_{jet} = 20\ cm$. The velocities are not measured on $y = 50\ cm$.

It should be noted that the deepest point of the scour hole in time for the different geometries are not the same. The time-averaged flow velocities and the horizontal Reynolds shear stress as depicted in Figure 4.22 and Figure 4.23 present values for different scour depths for the same time position.

4.2.3 Depth-averaged flow velocities

In this subsection, the depth-averaged flow velocities are considered. The depth-averaged flow velocities could give more insight in both the horizontal flow structure as the vertical flow structure. Figure 4.24 shows the positions of the ADV measurement of the lateral uniform case, whereas Figure 4.25 and Figure 4.26 shows the positions of the measurements for the two non-uniform cases. These figures show the positions of the measurements along the centerline ($y = 60\ cm$) for the final situation after 8 hours. The depth-averaged flow velocities are determined based on numerical integration of the measured flow velocities in the vertical.

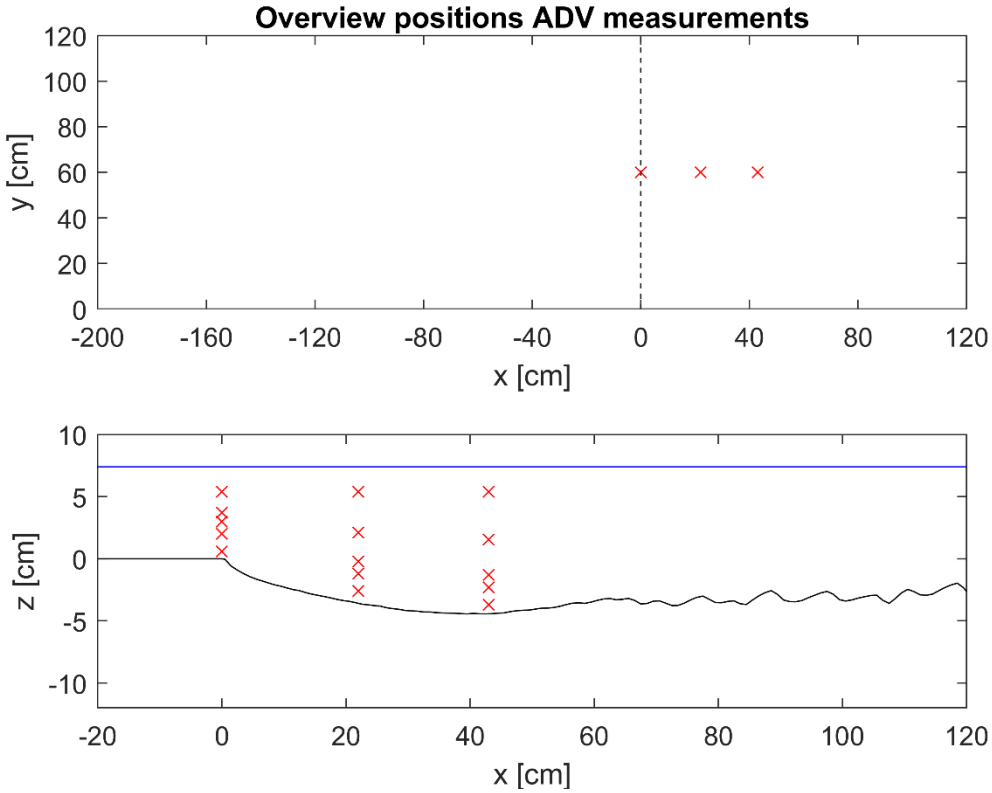

Figure 4.24: Overview of the positions ADV measurements lateral uniform flow.

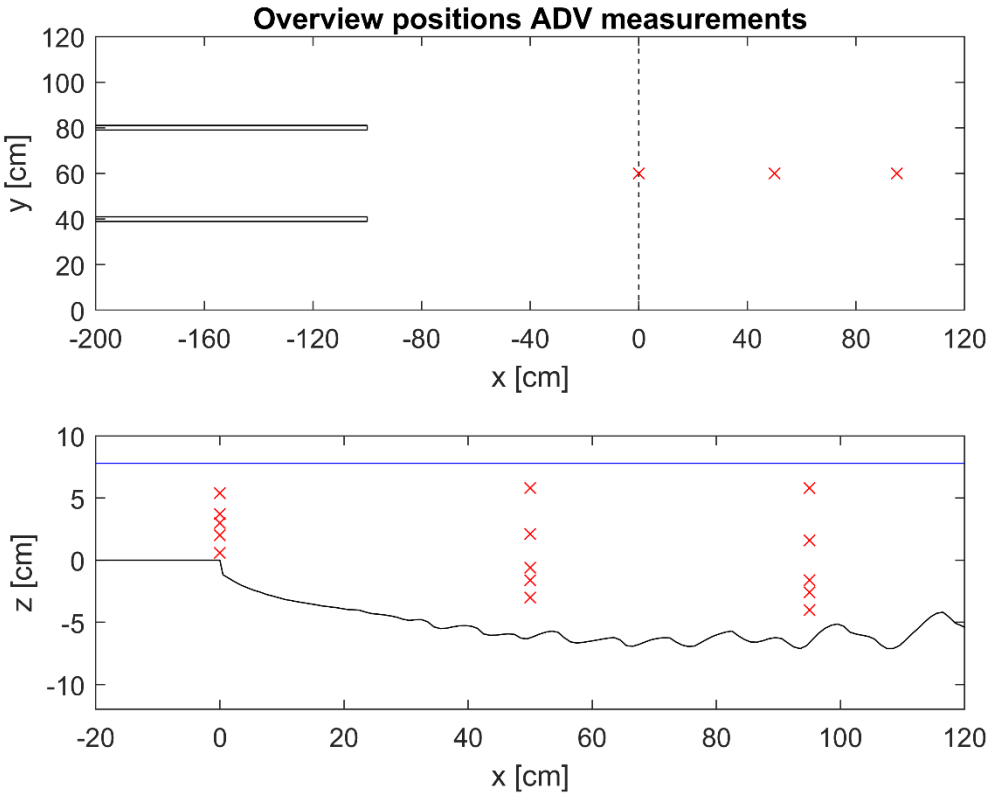

Figure 4.25: Overview of the positions ADV measurements non-uniform flow $B_{jet} = 40\ cm$.

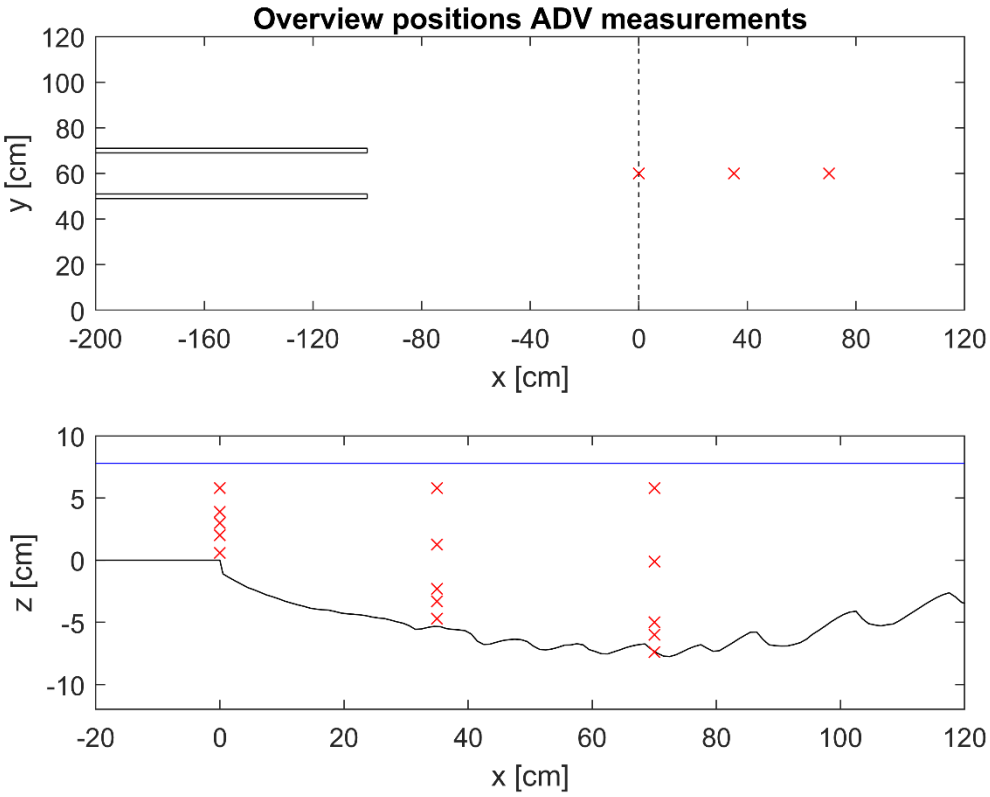

Figure 4.26: Overview of the positions ADV measurements non-uniform flow $B_{jet} = 20\ cm$.

The depth-averaged flow velocities for the different cases at the bed protection and at the deepest point in the scour hole are considered. Figure 4.27 shows the measurements of the depth-averaged flow velocities at the transition of fixed bed and mobile bed, near half-way the upstream scour slope and near the deepest point of the scour for all three cases. In addition, Figure 4.27 illustrates also the computations of the depth-averaged flow velocities at the maximum scour hole depth based on continuity. As the maximum scour hole depth is known, the decrease of the depth-average flow velocities based on continuity can be considered. Figure 4.28 presents the measured and the computed flow velocities as the ratio of the local depth-averaged flow velocity over the depth-averaged flow velocity at the end of the bed protection.

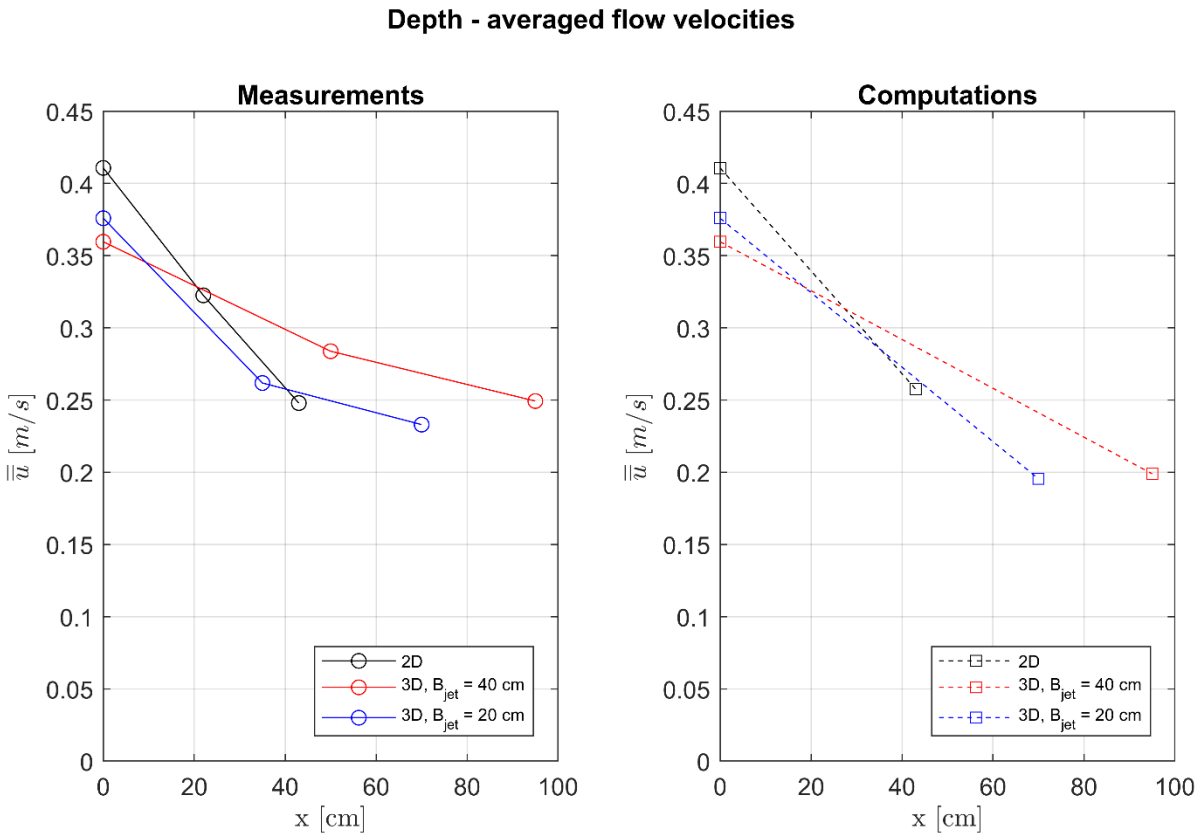

Figure 4.27: The depth-averaged flow velocities along the centerline. The left subplot presents the measurements, whereas the right subplot shows the computations of the decrease of the depth-averaged flow velocities due to an increase in depth based on continuity.

Table 4-3 presents the values of the velocity measurements:

	Depth-averaged flow velocity $\bar{\bar{u}}_0$ at the transition between fixed bed and erodible bed [measured]	**Depth-average relative turbulence intensity $\bar{r}_0$** [measured]
2D scour	$0.41\ m/s$	0.115
3D scour, $B_{jet} = 40\ cm$	$0.36\ m/s$	0.130
3D scour, $B_{jet} = 20\ cm$	$0.38\ m/s$	0.163

Table 4-3: Numerical values of the velocity measurements.

The depth-averaged relative turbulence intensity in Table 4-3 was approximated using (Schiereck, 1996):

$$\bar{r} = \frac{1}{\bar{\bar{u}}\, h} \cdot \int_0^h \sqrt{\overline{u'\, u'(z)}\, dz} \tag{4.1}$$

The depth-averaged relative intensity is actually calculated based on the measured local turbulence intentsities (Hoffmans, 1993b). For uniform flow, this expression for the depth-averaged fluctuation can be represented by (Hoffmans, 1993b):

$$\bar{r} = 1.2 \frac{\sqrt{g}}{C} \tag{4.2}$$

The measurement of the depth-averaged relative turbulence intensity for the two-dimensional scour under lateral uniform flow $\bar{r}_0 = 0.115$ as presented is in accordance with the calculated depth-averaged relative intensity by Equation 4.2 based on a Chezy value of $C = 33.1\ \sqrt{m}/s$, see subsection 3.2.1. In addition to Figure 4.27, the measurements of the depth-averaged flow velocities could be normalized with the depth-averaged flow velocity on top of the bed protection presented $\bar{\bar{u}}_0$. Figure 4.28 presents the normalized depth-averaged flow velocities.

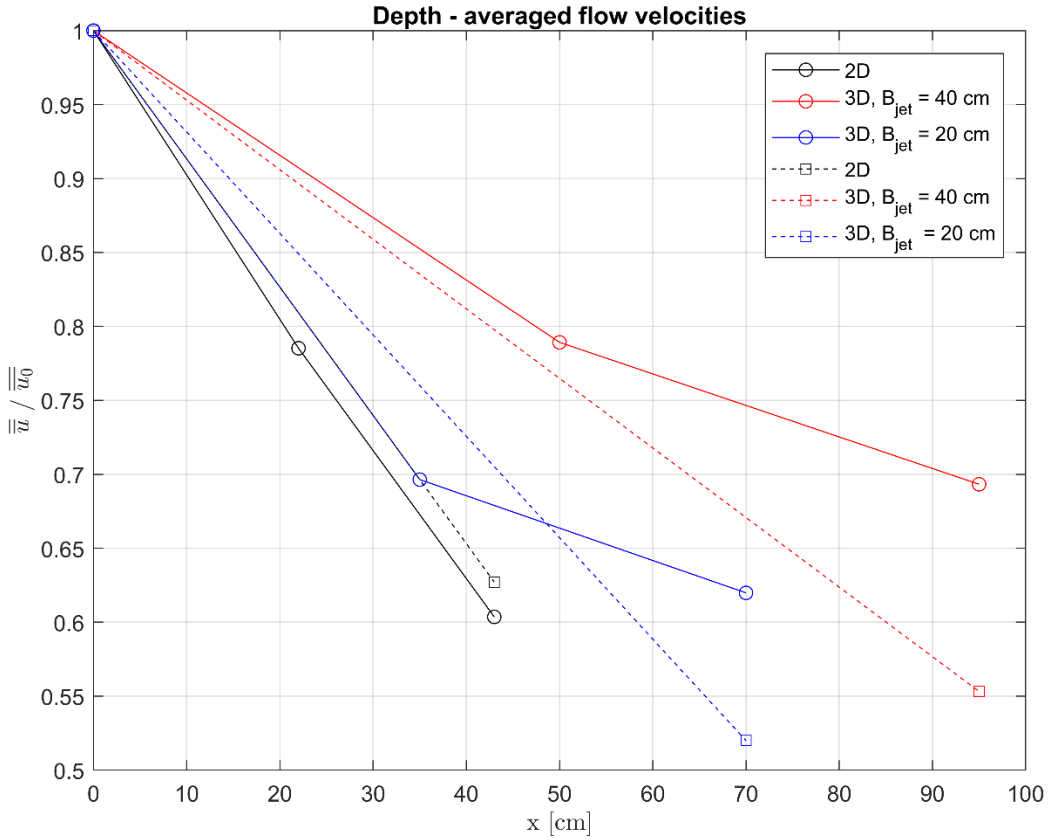

Figure 4.28: The normalized depth-averaged flow velocities along the centerline.

The following observations are made from Figure 4.27 and Figure 4.28:

It is clear that for laterally nonuniform flow the decrease of the depth-averaged flow velocities in the scour hole are not proportional to the depth increase. The depth-averaged flow velocities showed a reduced deceleration of the flow velocities in the scour hole for laterally nonuniform incoming flow. The depth-averaged flow velocities in the centerline on top of the bed protection ($x = 0$) should decrease proportional with the increase in flow depth at the location of the maximum scour depth ($x = h_s$) based on continuity. Due to lateral contraction of the flow, the depth-averaged streamwise velocities did not proportionally reduce to the depth increase. The observed high depth-averaged flow velocities are in agreement with the work of Broekema (2018). In addition, the depth-averaged flow velocities in the scour hole at the maximum scour hole depth are above the critical flow velocity $\bar{u}_c = 0.24\ m/s$.

4.3 Vertical flow structure

Here, the vertical flow structure of the flow in the scour hole is presented. First, the vertical distribution of the time-averaged velocity vectors in the scour hole under the lateral uniform is given. Second, the vertical distribution of the time-averaged velocity vectors in the scour hole under the two lateral non-uniform flow cases is shown. These time-averaged velocity vectors are determined on the centerline transect at the transition between fixed bed and erodible bed, approximately half-way the upstream scour slope and near the maximum scour depth. These velocity vectors are determined from the average values of the streamwise and vertical velocity components at the end of the experimental run. Furthermore, under each figure of the vertical distribution of the velocity vectors the numerical values of the depth-averaged velocities are presented in tables.

Figure 4.29 shows the distribution of the time-averaged velocity vectors under lateral uniform flow on the centerline longitudinal section, whereas Figure 4.30 and Figure 4.31 present the distribution of the time-averaged velocity vectors under lateral-non uniform flow. In Figure 4.29, it can be seen that the near-bed velocities are quite small at half-way the upstream scour slope and near the maximum scour depth. The small near-bed velocities in this zone might indicate the presence of a recirculation zone on the upstream scour slope despite the absence of clear return flows on the slope.

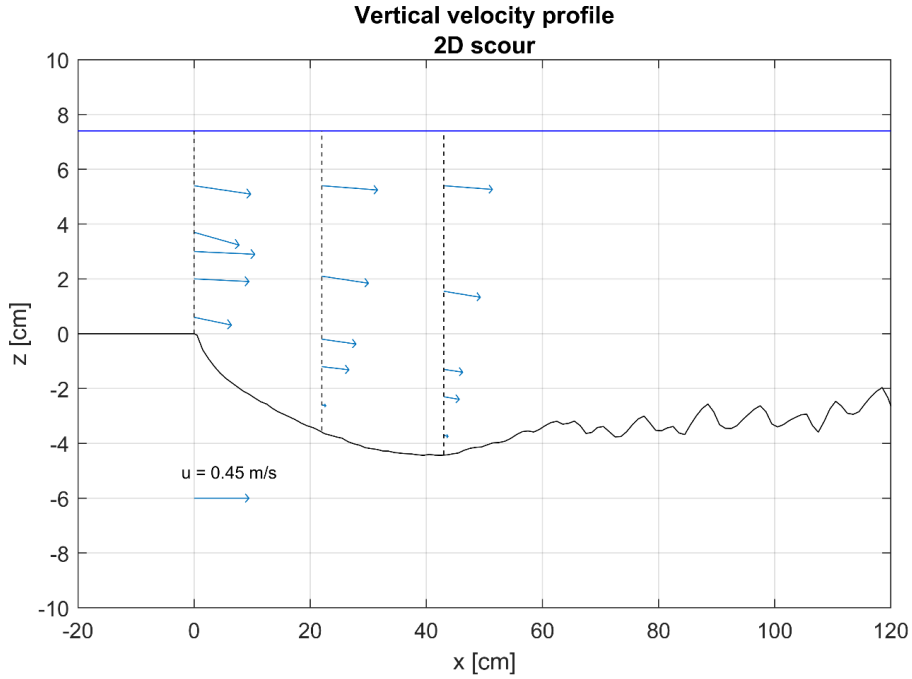

Figure 4.29: Time-averaged velocity vectors on the centerline transect at different x-locations ($x = 0, 22, 43\ cm$).

	$x = 0\ cm$	$x = 22\ cm$	$x = 43\ cm$
Depth-averaged flow velocity, $\bar{\bar{u}}$	$\bar{\bar{u}} = 0.41\ m/s$	$\bar{\bar{u}} = 0.32\ m/s$	$\bar{\bar{u}} = 0.25\ m/s$

Table 4-4: Numerical values of depth-averaged velocities

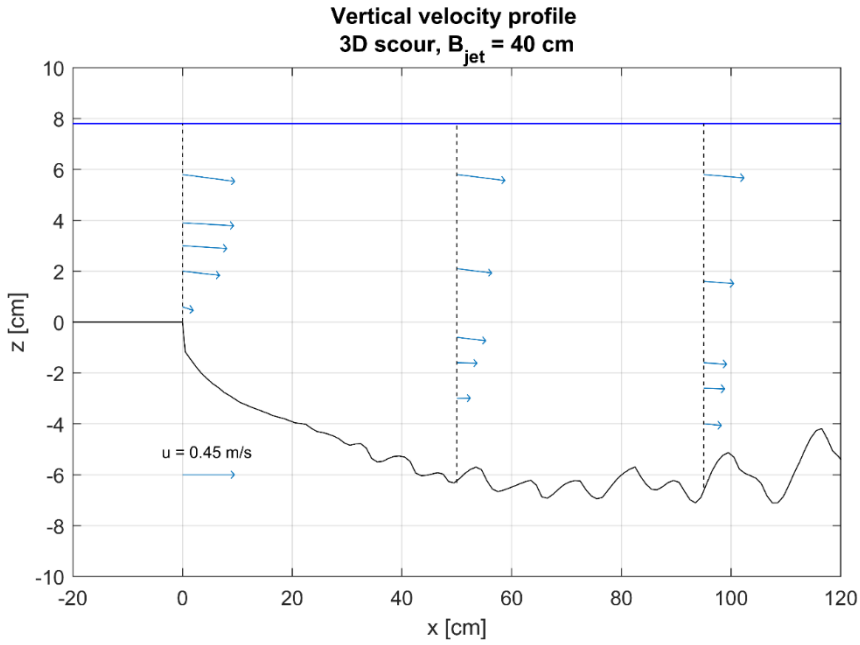

Figure 4.30: Time-averaged velocity vectors in the centerline transect at different x-locations ($x = 0{,}50{,}95\ cm$).

	$\boldsymbol{x = 0\ cm}$	$\boldsymbol{x = 50\ cm}$	$\boldsymbol{x = 95\ cm}$
Depth-averaged flow velocity, $\bar{\bar{u}}$	$\bar{\bar{u}} = 0.36\ m/s$	$\bar{\bar{u}} = 0.28\ m/s$	$\bar{\bar{u}} = 0.25\ m/s$

Table 4-5: Numerical values of depth-averaged velocities [2]

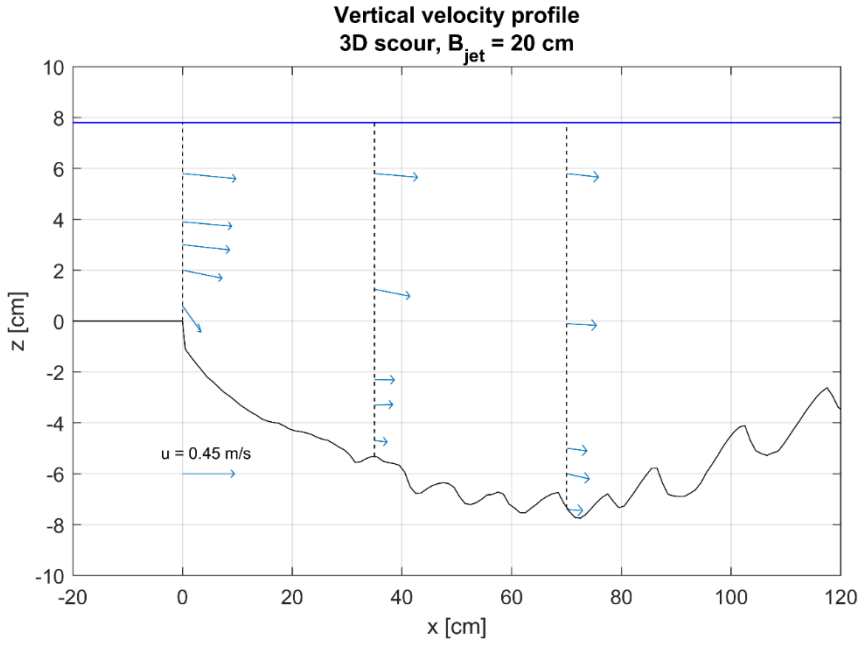

Figure 4.31: Time-averaged velocity vectors in the centerline transect at different x-locations ($x = 0{,}35{,}70\ cm$).

	$\boldsymbol{x = 0\ cm}$	$\boldsymbol{x = 35\ cm}$	$\boldsymbol{x = 70\ cm}$
Depth-averaged flow velocity, $\bar{\bar{u}}$	$\bar{\bar{u}} = 0.38\ m/s$	$\bar{\bar{u}} = 0.26\ m/s$	$\bar{\bar{u}} = 0.23\ m/s$

Table 4-6: Numerical values of depth-averaged velocities [3]

The vertical flow state in the scour hole under lateral non-uniform flow is different than the vertical flow structure observed under lateral uniform flow. The following observations are made concerning the vertical flow structure:

1. The near-bed velocities at half-way the upstream scour slope and near the maximum scour depth are not small for laterally nonuniform flow. The difference in the near-bed velocities can clearly be observed between Figure 4.29 and Figure 4.31. The near-bed velocities at half-way the upstream scour slope and near the deepest point of the scour hole for laterally nonuniform flow $B_{jet} = 20\ cm$ are relatively large compared to the near-bed velocities for lateral uniform flow. In addition, Figure 4.31 shows an obvious strong downward component of the near-bed velocity at the end of the bed protection compared to the near-bed velocity at the same location for lateral uniform flow depicted in Figure 4.29.

2. The vertical structure of the flow appears to become more depth uniform in the scour hole for laterally nonuniform flow (Figure 4.30 and Figure 4.31) compared to the vertical flow structure for lateral uniform flow (Figure 4.29).

3. The transition of the fixed bed to the erodible bed for laterally uniform and non-uniform flow is different. One can observe that the upstream scour slope is more or less continuous and results in a smooth transition of the fixed bed to the erodible bed, whereas no clear upstream scour slope can be observed for laterally nonuniform flow as depicted in Figure 4.30 and Figure 4.31. A probable explanation for the dis-continuous transition between fixed bed and erodible bed is the absence of a recirculation zone. The return flow in the recirculation zone transports some sediment against the main flow direction in the direction of the bed protection. A vertical recirculation zone is created as a result of flow separation. This flow separation might be suppressed by the presence of lateral non-uniformities in the flow and therefore sediment might not be transported in the direction of the bed protection by a return flow. Therefore, a discontinuous transition between the bed protection and scour hole might be observed as in Figure 4.30 and Figure 4.31.

4.4 Bed shear stress estimation

To gain more insight into the development of the scour holes under lateral non-uniform flow, the actual load on the bed should be considered. Therefore, the flow fluctuating components are also considered. In this present work, two methods were used to estimate the bed shear stress in the scour hole, namely the Reynolds shear stress τ_{xz} and the turbulent kinetic energy (TKE) E.

The turbulent kinetic energy is determined by (e.g., Cohen, 2012):

$$E = \frac{1}{2}\rho_w\left(\overline{u'^2} + \overline{v'^2} + \overline{w'^2}\right)$$

The Reynolds shear stresses are computed by (e.g., Cohen, 2012)

$$\tau_{xy} = \tau_{yx} = -\rho_w\overline{u'v'} \qquad \tau_{xz} = \tau_{zx} = -\rho_w\overline{u'w'} \qquad \tau_{yz} = \tau_{zy} = -\rho_w\overline{v'w'}$$

In the above expressions, the prime and the overbar denote the fluctuating component and the time average of the total velocity signal after Reynolds decomposition respectively. The reader is referred to Appendix B.1.3 for more detail about turbulence and Reynolds decomposition. The method using the turbulent kinetic energy E to estimate the bed shear stress assumes a linear relation between the TKE and the bed shear stress, namely: $\tau_0 = CE$ (Soulsby, 1981). The coefficient in the previous expression was found to be 0.19 for complex flow fields (Biron et al., 2004). Figure 4.32 presents the Reynolds shear stress τ_{xz} and the turbulent kinetic energy (TKE) for laterally uniform flow and laterally nonuniform flow. The laterally nonuniform flow $\mathrm{B_{jet}} = 40\ \mathrm{cm}$ is not considered in Figure 4.32, because of no suitable near-bed velocities measurements as discussed in subsection 3.5.

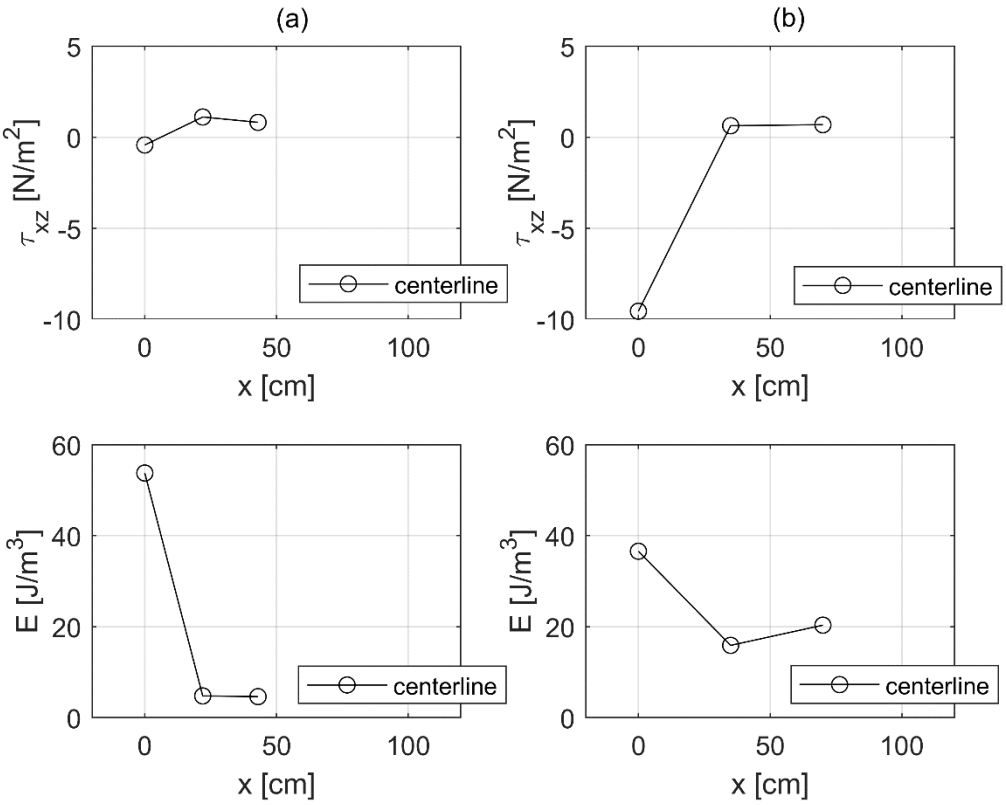

Figure 4.32: The Reynolds stress τ_{xz} and the TKE for the experimental runs under uniform flow and laterally nonuniform flow ($B_{jet} = 20\ cm$).

The following observations are made from Figure 4.32:

1. TKE subplots; Here, one can observe the high TKE values under non-uniform flow in the scour hole. Based on these high TKE values in the centerline under non-uniform flow, the bed shear stress under lateral non-uniform flow might be higher than for lateral uniform flow. One cannot observe higher τ_{xz} under lateral non-uniform flow.

2. One observes a very high negative value of the bed shear stress τ_{xz} at $x = 0$ for laterally nonuniform flow conditions. This high negative value of τ_{xz} cannot be explained.

The bed shear stress estimation results are further discussed in section 5.

5 Discussion

This chapter discusses the results that were obtained by the physical experiments. The results of the scour development, the horizontal flow structure and vertical flow structure are addressed. In addition, a review on the applicability of the results in the field is given.

5.1 Interpretation of the results

Scour

The scour development for lateral uniform and lateral non-uniform incoming flow were considered. The scour hole for laterally nonuniform flow were deeper and developed faster than the scour hole for uniform flow. The lateral non-uniform scour hole was characterized by two deep parts at the sides and a less deep part in the center of the scour hole. The scour depths were more significant in the mixing layers than in the main flow. The horizontal Reynolds shear stresses τ_{xy} were considered to explain the spatial variability of the scour hole in lateral direction. It was expected that the highest horizontal shear stresses τ_{xy} should be observed along the transect in which the significant scour depths developed. However, the highest horizontal Reynolds shear stresses τ_{xy} were not on the same transect as the significant scour depths. A possible explanation could be that the combination of flow velocity and turbulence intensity was more critical for the scour development along the observed transect than the transect in which the highest horizontal Reynolds shear stresses τ_{xy} were observed.

The maximum scour hole depths can be predicted by the Breusers empirical relation as discussed in section 2. The applicability of the Breusers formula on the scour measurements are considered. The three-dimensional scour hole development in time could be fitted reasonably to the time development of the Breusers relation provided the experimentally determined coefficients. The measured characteristic time scale for the three-dimensional scour hole development was significantly lower than the calculated characteristic time scale.

Horizontal flow structure

The experiments have shown a horizontal contraction of the flow at the scour hole for lateral non-uniform incoming flow. This horizontal contraction of the flow was expected based on the observations of a contraction of the flow at the location of a downward slope by Van de Zande (2018) and Broekema (2017). Dye visualization of the flow and the depth-averaged flow velocities were considered to give more insight into the horizontal flow structure. Inspection with dye revealed that the horizontal flow structure for flow with lateral velocity differences is affected by the scour hole, whereas no effects on the horizontal flow structure by the scour hole were observed for laterally uniform incoming flow. In addition, the depth-averaged flow velocities showed a reduced deceleration of the flow velocities in the scour hole for laterally nonuniform incoming flow. Due to the lateral contraction of the flow, the depth-averaged streamwise velocities did not proportionally reduce to the depth increase.

In this thesis, the results only shed more light on the possible complex interaction between the horizontal and vertical flow state. A possible explanation behind the horizontal convergence-vertical flow attachment behavior of the flow is missing. In Broekema (2017) and Broekema et al. (2018), it is hypothesized that laterally nonuniform flow may contract in the horizontal plan by a streamwise depth increase through conservation of potential vorticity. This additional acceleration may on his turn suppress vertical flow separation on a steep downstream slope. The results of this experiment could not give more insight into this hypothesis. In order to be complete though, the conservation of potential vorticity is considered as part of the literature study and it is taken in Appendix B.1.6.

Vertical flow structure

The vertical structure of the flow in the scour hole is considered in section 4.3. The experimental results indicated that for laterally nonuniform flow the vertical flow structure in the scour hole appears to become more depth uniform. In addition, the near-bed velocities in the scour hole for the laterally nonuniform flow case are large relative to the near-bed velocities of the reference case. These observations showed the importance of the lateral non-uniformities in the flow field on the vertical structure of the flow in the scour hole. The adverse pressure gradient that is responsible for separation of the boundary layer from the bed can be reduced due to contraction. As a result, boundary layer suppression on the upstream scour slope might be suppressed. These observations were in line with the experimental results of Broekema (2017) and Van de Zande (2018). Furthermore, the vertical structure of the flow might also be important for the sediment transport in the scour hole. Due to the absence of recirculation zone with return flows for vertically attached flows, sediment could not be transported towards the bed protection. It might be expected that no sediment supply from the scour hole toward the bed protection could result in the undermining of the edge of the bed protection.

As mentioned, the near-bed velocities in the scour hole for laterally nonuniform case were large. It was expected that these high near-bed velocities would result in high bed shear stresses. In both Broekema (2017) and Van de Zande (2018), estimations for the bed shear stresses between experiments with vertical flow attachment and separation showed higher bed shear stresses for attached flows. Therefore, the vertical flow attachment in the scour holes can enhance scour development as stated by Van de Zande (2018). However, high bed shear stresses near the deepest point of the scour hole could not be measured in the experiments. The bed shear stress estimation results were different than expected. For example, the large negative value of the Reynolds shear stress τ_{xz} at $x = 0$ in Figure 4.32b and the increase of the

Reynolds shear stresses τ_{xz} afterwards to positive values cannot be explained. No conclusions can be obtained based on the measurements concerning the bed shear stresses. Probably, mistakes were made unconsciously during measurements.

5.2 Applicability in the field

- The physical experiments have shown that scour holes in laterally nonuniform flow are deeper and develop faster. This might partly explain the more rapidly development of the scour hole behind the bottom protection than initially predicted in the field at the outlet structure.

- A very different scour pattern is observed between the scale model tests and in the field. The three-dimensional scour holes in the experiments were characterized by two distinct deep parts at the sides in the mixing layers, whereas in the field one maximum scour depth in the center of the outflow was observed. The widening of the of the mixing layers in the horizontal plane were taken into account in the experimental setup by considering the length of the bed protection over the inflow width in the prototype. The geometry of a jet inflow of $Bjet = 40\ cm$ with ratio $L_{b,m}/B_m = 2.5$ is in the same order of the ratio in the prototype of $L_{b,p}\ /W_p = 2.3$. However, the observed scour pattern in the experiment is different than in the field as mentioned.

- Horizontal recirculation regions are present in the field adjacent to the tidal jet ese recirculation cells probably influence the development of the mixing layers in the field. In the laboratory experiments, no horizontal recirculation cells are considered.

6 Conclusions and recommendations

In this thesis the scour development under laterally nonuniform flow is investigated. The research focused on the following research question:

How may lateral non-uniform flow affect the scour hole development and what are the effects of this nonuniformity on the flow conditions in and near a scour hole?

The research question is divided into three sub questions, namely:

1. How does the scour development in lateral non-uniform flow compare to the scour development in lateral uniform flow?

2. How does the presence of the scour hole affect the horizontal flow structure of the laterally nonuniform flow?

3. How does the presence of lateral nonuniformities in the flow field affect the vertical flow structure in the scour hole?

Section 6.1 focusses on the answering of the research questions of this thesis, whereas section 6.2 presents recommendations for further research.

6.1 Conclusions

1. How does the scour development in lateral non-uniform flow compare to the scour development in lateral uniform flow?

- The scour hole in laterally nonuniform flow is deeper and it develops faster compared to the scour development in laterally uniform flow under the same hydraulic conditions.

- Lateral non-uniform flow results in a lateral non-uniform scour hole profile. The spatial variability of this three-dimensional scour hole is important. The maximum scour depths are larger in the mixing layers than in the main flow.

- The scour hole development in the center of the three-dimensional scour hole can be fitted reasonably to the time-development given by Breusers (1966) provided that the experimentally determined characteristic time t_1 and coefficient γ are used. The characteristic time t_1 could not be predicted in advance.

2. How does the presence of the scour hole affect the horizontal flow structure of the laterally nonuniform flow?

- A horizontal contraction of the flow at the scour hole is observed for lateral non-uniform incoming flow. The horizontal contraction is observed by dye inspection and a lateral shift of the center of the mixing layer towards the high velocity zone in the scour hole indicates a contraction of the flow.

- The decrease of the depth-averaged flow velocities in the scour hole are not proportional to the depth increase by the scour hole. Based on the horizontal Reynolds shear stresses τ_{xy}, a lateral shift of the center of the mixing layer towards the high velocity zone in the scour hole is observed.

- The presence of the scour hole does not affect the horizontal structure of the flow for lateral uniform incoming flow.

3. How does the presence of lateral nonuniformities in the flow field affect the vertical flow structure in the scour hole?

- Relatively high near-bed velocities in the scour hole are observed for laterally nonuniform flow ($B_{jet} = 20\ cm$).

- The vertical structure of the flow appears to become more depth uniform in the scour hole for laterally nonuniform flow.

- A discontinuous transition between the upstream part of the scour hole and the adjacent fixed bed in is observed for laterally nonuniform flow. A clear upstream scour slope from the edge of the fixed bed to the maximum scour depth is absent.

- The velocity measurements could not prove vertical flow separation nor vertical flow attachment at the upstream part of the scour hole.

As the sub-question are answered, the main research question is answered as follows:

Main research question: How may lateral non-uniform flow affect the scour hole development and what are the effects of this nonuniformity on the flow conditions in and near a scour hole?

In this master thesis, the influence of the lateral non-uniformities in the flow on the scour hole development have been investigated. Physical experiments were conducted in order to investigate the influence of lateral non-uniformities in the flow field on the scour hole development and to obtain more fundamental understanding behind the scour processes. The scale experiments included lateral velocity difference by the confluence of two parallel streams with different velocities in shallow flow. Lateral non-uniform flow resulted in a three-dimensional scour hole behind the bed protection. The three-dimensional scour hole was deeper and developed faster than the two-dimensional scour hole for lateral uniform incoming flow. In addition, the three-dimensional scour holes were characterized by two distinct deep parts at the sides.

Although the highest flow velocities were observed in the main flow in the center, the maximum scour depths were the largest in the mixing layer region. In addition, visualization of the flow and velocity measurements for laterally nonuniform flow have indicated a horizontal contraction of the flow at the scour hole and a more depth uniform vertical flow structure in the scour hole.

6.2 Recommendations

In the following, recommendations are suggested for possible experiments and further research based on this thesis.

- Two different geometries are considered in the laboratory experiments to investigate the influence of lateral non-uniformities in the flow on scour development. The widening of the horizontal mixing layers in the horizontal plane is important. The mixing layers discerns the flow development region and the fully developed region of a jet flow. In this present work, a ratio of $L_{b,m}/B_m = 2.5$ and a ratio of $L_{b,m}/B_m = 5$ are regarded in the model tests. It is recommended to investigate the influence on the three-dimensional scour hole development under larger ratios by lengthening the bed protection or decreasing the width at inflow.

- In this experiment work, qualitative measurements of the surface flow with for example particle image velocimetry is missing. In order to obtain more insight in the horizontal structure of the flow at the scour hole, for example particle image velocimetry could help to describe the surface flow in more detail.

- The velocity measurements to identify flow attachment and flow separation are performed in the jet center only. It is recommended to conduct velocity measurements along different transects for the vertical flow structure. These velocity measurements could shed more light on the observations of Van de Zande (2018) for example in which flow attachment was observed in the horizontal mixing layers.

- In order to have a better understanding of the hydrodynamics in the scour hole, it is recommended to fix the scour hole in time. For example, in the experimental work of Stenfert (2018), the scour hole geometry was fixed with the help of sprayed car lacquer and hair coat. It is obvious that is it difficult to measure velocities while the scour process continues. One can measure in this way very accurately both the horizontal and vertical flow structure in a three-dimensional scour hole.

- It is stated that for a better understanding of the development of three-dimensional scour holes more insight is needed in the fundamental hydrodynamic processes in the scour hole. It is recommended to obtain also more detailed information on flow patterns in scour holes in the field.

- A practical recommendation would be the lengthening of the bed protection to reduce the scour hole downstream of the structure. Lateral velocity differences should be reduced as much as possible at the edge of the bottom protection. A long bed protection should be the most effective way to reduce scour depths.

Bibliography

Bailly, C. & Comte-Bellot, G. (2015). *Turbulence*. Switzerland: Springer International Publishing.

Battjes, J. A. (2002). Vloeistofmechanica CT2100. Delft, The Netherlands: TU Delft.

Bergsma, E. W. J., & Bogaard, T. (2011). *Turbulence in shallow jet flows* (Additional Master's thesis, Delft University of Technology).

Biron, P. M., Robson, C., Lapointe, M. F., & Gaskin, S. J. (2004). Comparing different methods of bed shear stress estimates in simple and complex flow fields. Earth Surface Processes and Landforms: *The Journal of the British Geomorphological Research Group, 29*(11), 1403–1415.

Blanckaert, K. (2010). Topographic steering, flow recirculation, velocity redistribution, and bed topography in sharp meander bends*. Water Resources Research, 46*, W09506, doi:10.1029/2009WR008303.

Blanckaert, K. (2011). Hydrodynamic processes in sharp meander bends and their morphological implications. *Journal of Geophysical Research, 116,* F01003, doi:10.1029/2010JF001806.

Bom, S. (2017). *Scour holes in heterogenous subsoil: A numerical study on hydrodynamic processes in the development of the scour holes* (Master's thesis, Delft University of Technology).

Booij, R. (1992). TURBULENTIE in de waterloopkunde CT5312. Delft, The Netherlands: TU Delft.

Breusers, H. N. C., & Raudkivi, A.J. (1991). *Scouring.* Rotterdam: Balkema.

Breusers, H. N. C. (1966). Conformity and time scale in two-dimensional local scour. *Proc. Symposium on model and prototype conformity,* 1-8, Hydraulic Research Laboratory, Poona (also Delft Hydraulics, Delft, Publication 40).

Broekema, Y. B. (2017). Experimental log. Technical report, Delft University of Technology.

Broekema, Y. B., Labeur, R. J., & Uijttewaal, W. S. J. (2018). Observations and analysis of the horizontal structure of a tidal jet at deep scour holes. *Journal of Geophysical Research: Earth Surface, 123,* doi.org/10.1029/2018JF004754.

Buchko, M. F., Kolkman, P. A., & Pilarczyk, K. W. (1987). Investigation of local scour in cohesionless sediments using a tunnel-model. *IAHR-congress, Lausanne; Topics in hydraulic modelling:* 223-239.

Buchko, M. F. (1986*). Investigation of local scour in cohesionless sediments by using a tunnel model* (Report Q239). Delft Hydraulics, Delft.

Cohen, C. (2012*). Shallow-Water Plane and Tidal Jets.* PhD thesis, University of Otago.

De Graauw, A. F. F. (1981). *Scour* (in Dutch) (Report M1001). Delft Hydraulics, Delft.

De Graauw, A. F. F., & Pilarczyk, K.W. (1981). Model-prototype conformity of local scour in noncohesive sediments beneath overflow-dam. *19th IAHR-congress*, New Delhi (also Delft Hydraulics, Delft Publication 242).

Delft Hydraulics (1969) Begin van beweging van bodemmateriaal, report S159-1

Delft Hydraulics (1976). *Systematic investigation of two and three-dimensional local scour* (in Dutch) (Investigation M648/M863/M847). Delft Hydraulics, Delft.

Delft Hydraulics (1979). *Prototype scour hole 'Brouwersdam'* (Investigation M1533, Parts 1, 2, 3 and 4). Delft Hydraulics, Delft.

de Vries, M. (1982). *Scale models in hydraulic engineering.* International Institute for Hydraulic and Environmental Engineering, Delft.

Dietz, J. W. (1969). *Kolkbildung in feinen oder leichten Sohlmaterialen bei strömendem Abfluss*. Theodor Rehbock Flussbaulaboratorium, Mitteilungen Heft 155, Karlsruhe.

Frostick, L. E., McLelland, S. J. & Mercer T.G. (Eds.). (2011). *Users Guide to Physical Modelling and Experimentation: Experience of the HYDRALAB Network.* Leiden: CRC Press/Balkema.

García, C. M., Cantero, M. I., Niño, Y., García, M. H. (2005). Turbulence Measurements with Acoustic Doppler Velocimeters. *Journal of Hydraulic Engineering, 131 (12),* 1062-1073, doi:10.1061/(ASCE)0733-9429(2005)131:12(1062).

Goring, D. G., Nikora, V. I. (2002). Despiking Acoustic Doppler Velocimeter Data. *Journal of Hydraulic Engineering, 128 (1),* 117-126, doi:10.1061/(ASCE)0733-9429(2002)128:1(117).

Guan, D., Melville, B. W., & Friedrich, H. (2014). Flow Patterns and Turbulence Structures in a Scour Hole Downstream of a Submerged Weir. *Journal of Hydraulic Engineering, 140,* 68-76, doi:10.1061/(ASCE)HY.1943-7900.0000803.

Hoffmans, G. J. C. M. (1990). *Concentration and flow velocity measurements in a local scour hole* (Report 4-90). Delft University of Technology.

Hoffmans, G. J. C. M. (1992). *Two-dimensional mathematical modelling of local scour holes.* Doctoral thesis, Delft University of Technology.

Hoffmans, G. J. C. M. (1993a). *A hydraulic and morphological criterion for upstream slopes in local-scour holes* (Report W-DWW-93-255). Ministry of Transport, Public Works and Water Management, Road and Hydraulic Engineering Division, Delft.

Hoffmans, G. J. C. M. (1993b). *A study concerning the influence of the relative turbulence intensity on local-scour holes* (Report W-DWW-93-251). Ministry of Transport, Public Works and Water Management, Road and Hydraulic Engineering Division, Delft.

Hoffmans, G. J. C. M., & Booij, R. (1993a). The influence of upstream turbulence on local-scour holes. *Proc. 25th IAHR-congress,* Tokyo.

Hoffmans, G. J. C. M., & Booij, R. (1993b). Two-dimensional mathematical modelling of local-scour holes. *Journal of Hydraulic Research, 31:5,* 615-634, doi:10.1080/00221689309498775.

Hoffmans, G. J. C. M., & Pilarczyk, K. W. (1995). Local scour downstream of hydraulic structures. *Journal of Hydraulic Engineering, ASCE, 121(4),* 326-340.

Hoffmans, G. J. C. M., & Verheij, H. J. (1997). *Scour manual.* Rotterdam: Balkema.

Hoffmans, G. J. C. M. (2012). *The influence of turbulence on soil erosion.* Delft: Eburon Academic Publishers.

Hoffmans, G. J. C. M., & Verheij, H. J. (2016). *Update Scour manual.* Unpublished, Deltares, Delft.

Jirka, G. (1994). Shallow jets. *Recent Research Advances in the Fluid Mechanics of Turbulent Jets and Plumes* of *Nato Advanced Science Institutes Series, 155-175.*

Jorrisen, R. E., & Vrijling, J. K. (1989). Local scour downstream hydraulic constructions. *IAHR-congress, Ottawa.*

Koopmans, H. (2017). *Scour holes in tidal rivers with heterogeneous subsoil under anthropogenic influence* (Master's thesis, Delft University of Technology).

Labeur, R. J. (Ed.). (2010). Vloeistofmechanica 2 CT2140. Delft, The Netherlands: TU Delft.

Pietrzak, J. (2017a). *An Introduction to Oceanography for Civil and Offshore Engineers CT5317*. Delft, The Netherlands: TU Delft.

Pietrzak, J. (2017b). *An Introduction to Stratified Flows for Civil and Offshore Engineers CIE5302*. Delft, The Netherlands: TU Delft.

Pritchard, P. J. (2011). *Fox and McDonald's Introduction to Fluid Mechanics* (8th ed.). United States of America: John Wiley & Sons, Inc.

Rajaratnam, N. (1976). *Turbulent jets.* Amsterdam: Elsevier.

Schiereck, G. J. (2012*). Introduction to Bed, bank and shore protection; updated by Verhagen, H.J.* Delft: VSSD.

Shiono, K., & Knight, D. W. (1991). Turbulent open-channel flows with variable depth across the channel. *Journal or Fluid Mechanics, 222*, 617-646.

Soulsby, R. L. (1981). Measurements of the Reynolds stress components close to a marine sand bank. *Marine Geology, 42*(1-4), 35–47.

Stenfert, J. G. (2017). *Scour holes in heterogenous subsoil: An experimental study to improve knowledge of the development of scour holes in heterogeneous subsoil* (Master's thesis, Delft University of Technology).

Stewart, R. H. (2008). *Introduction to Physical Oceanography*. Texas A & M University.

Talstra, H. (2011). *Large-scale turbulence structures in shallow separating flows*. PhD thesis, Delft University of Technology.

Termini, D., & Sammartano, V. (2012). Morphodynamic process downstream of man-made structural interventions: Experimental investigation of the role of turbulent flow structures in the prediction of scour downstream of a rigid bed. *Physics and Chemistry of the Earth, 49,* 18-31, doi: 10.1016/j.pce.2011.12.006.

Uijttewaal, W. (2017). *Turbulence in hydraulics CIE5312*. Delft, The Netherlands: TU Delft.

van der Meulen, T. & Vinje, J. J. (1975). Three-dimensional local scour in noncohesive sediments. *Proc. 16th IAHR-congress*, Sao Paulo, Brazil (also Delft Hydraulics, Delft, Publication 180).

van der Wal, M., (1991). *Onderzoek naar ontgrondingen bij een horizontale vernauwing* (Report Q935). Delft Hydraulics, Delft.

Van de Zande, B. J. (2018). *Jet behaviour in longitudinal deepening shallow flows* (Master's thesis, Delft University of Technology).

van Prooijen, B. C. (2004). *Shallow Mixing Layers*. PhD thesis, Delft University of Technology.

van Prooijen, B. C., Battjes, J. A., & Uijttewaal, W. S. J. (2005). Momentum Exchange in Straight Uniform Compound Channel Flow. *Journal of Hydraulic Engineering, 131*, 175-183, doi:10.1061/(ASCE)0733-9429(2005)131:3(175).

van Velzen, G., Raaijmakers, T. C., & Hoffmans, G. J. C. M. (2015). Scour development around the Eastern Scheldt storm surge barrier-field measurements and model predictions. *Proceedings of the 7th International Conference on Scour and Erosion,* 693-704.

van Zuylen, J. A. (2015). *Development of scour in non-cohesive sediment under a poorly erodible top layer* (Master's thesis, Delft University of Technology).

Vermeulen, B., Hoitink, A. J. F., & Labeur, R. J. (2015). Flow structure caused by a local cross-sectional area increase and curvature in a sharp river bend. *Journal of Geophysical Research: Earth Surface, 120,* 1771-1783, doi:10.1002/2014JF003334.

Zanke, U., 1978*, Zusammenhänge zwischen Strömung und Sedimenttransport.* Teil 1: Berechnung des Sedimentrasportes, -allgemeiner Fall-, Teil 2: Berechnung des Sedimenttransportes hinter befestigten Sohlenstrecken, -Sonderfall zweidimensionaler Kolk-. Mitteilungen des Franzius-Instituts der TU Hannover, Heft 47, 48.

A Figures of scour hole

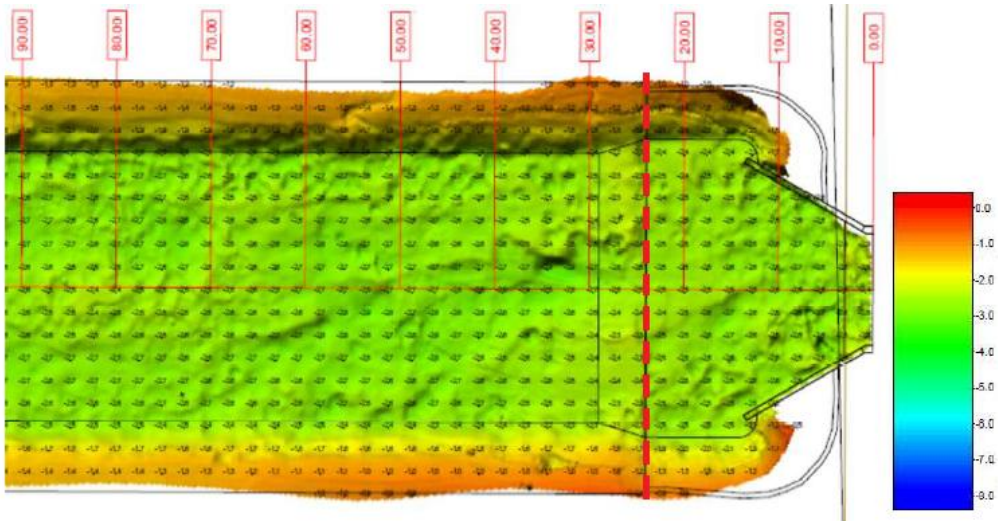

Figure A.1: Initial bathymetry. The red dotted line indicates the edge of the bottom protection.

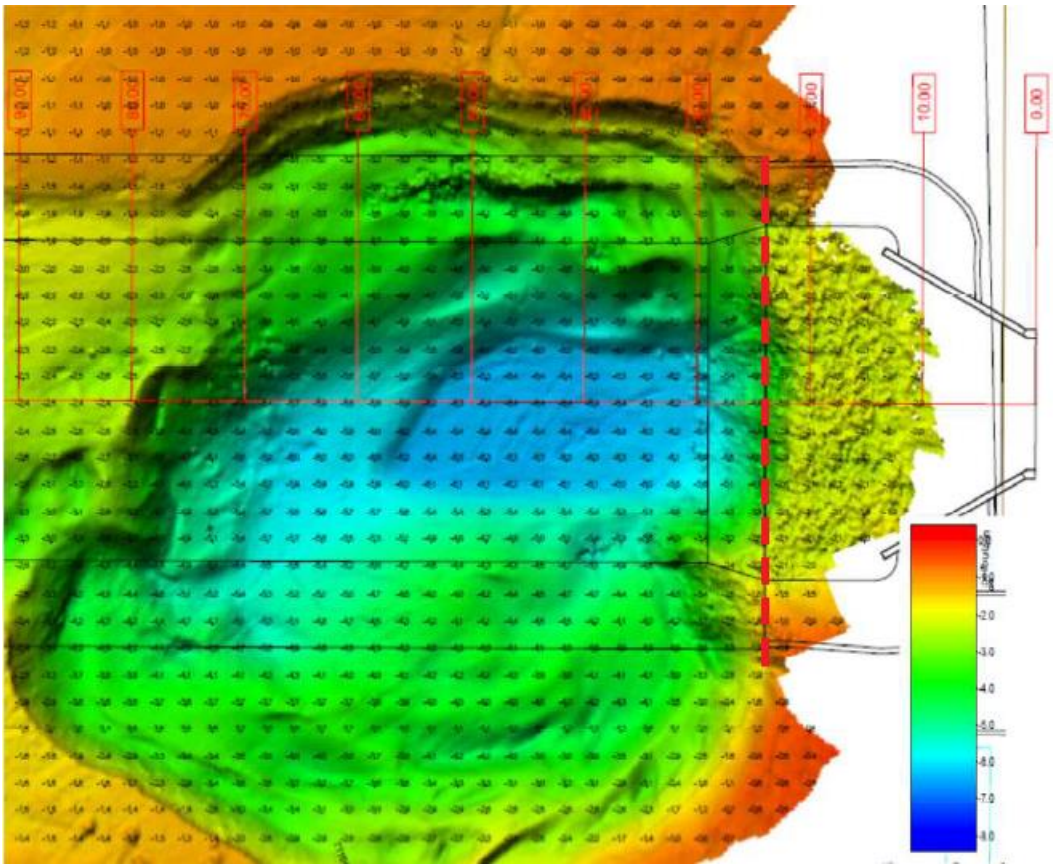

Figure A.2: The bathymetry after 6 days with scour hole. The red dotted line indicates the edge of the bottom protection.

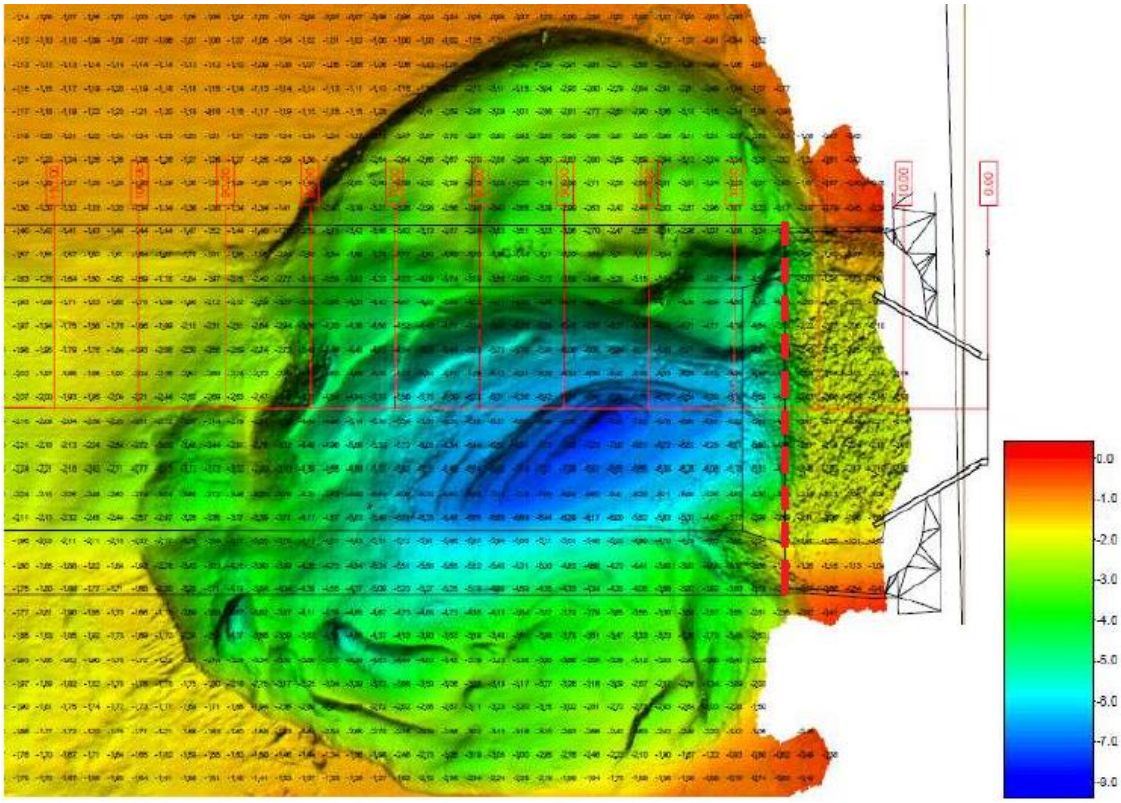

Figure A.3: The bathymetry after 12 days with scour hole. The red dotted line indicates the edge of the bottom protection.

B Additional literature

B.1 Flow

B.1.1 Characterization of flow

The most important dimensionless numbers for describing flow are the Froude number and the Reynolds numbers. The Froude number presents the ratio between inertia and gravitational forces of a fluid, see Equation A.1. The Froude number determines whether the flow is sub-critical ($Fr < 1$), critical ($Fr = 1$), or super-critical ($Fr > 1$).

$$Fr = \frac{U}{\sqrt{gL}} \tag{B.1}$$

where: $U = velocity\ scale\ [m/s]$

$g = gravitional\ acceleration\ [g = 9.81\, m/s^2]$

$L = length\ scale\ [m]$

The Reynolds number describes the ratio between inertia and viscous forces. It determines whether the flow is laminar of turbulent. The Reynolds number gives an indication of the amount of turbulence in the flow. Flow is called turbulent when $Re \gg 1000$.

$$Re = \frac{UL}{\nu} \tag{B.2}$$

where: $U = velocity\ scale\ [m/s]$

$L = length\ scale\ [m]$

$\nu = kinematic\ viscosity\ [m^2/s]$

B.1.2 Types of flow

Uniform flow

In uniform flow, an equilibrium exists between bottom shear stress and the component of the fluid pressure on the slope. Figure B.1 shows uniform flow in a channel. In a stationary, uniform flow, the boundary layer is fully developed and takes up the entire water depth. This results in a logarithmic velocity profile over the depth.

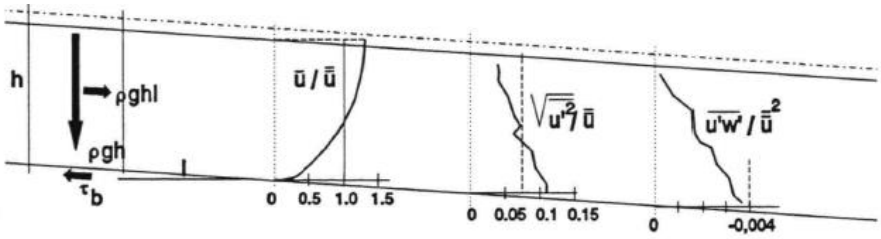

Figure B.1: Uniform flow (Schiereck, 2012)

Non-uniform flow

Flow is almost never uniform in practice. There are accelerations and decelerations in the flow influencing the boundary layer and the turbulence in the flow. The boundary layer is defined as the region which is influenced by the presence of the wall, in contrast to the region outside the boundary layer. Acceleration is due to a pressure gradient in the flow direction and an opposite gradient leads to deceleration. Both acceleration and deceleration cause a change in the boundary layer thickness. The change in δ is roughly given by:

$$\frac{d\delta}{dx} = \frac{-(4\ to\ 5)\delta}{u_0}\frac{du_0}{dx} \tag{B.3}$$

where: $\delta = boundary\ layer\ thickness\ [m]$

Equation A.3 shows that acceleration causes a reduction of the boundary layer thickness, whereas deceleration causes an increase in the boundary layer thickness. These changes of the boundary layer thickness are visible in the velocity profile, see Figure B.2.

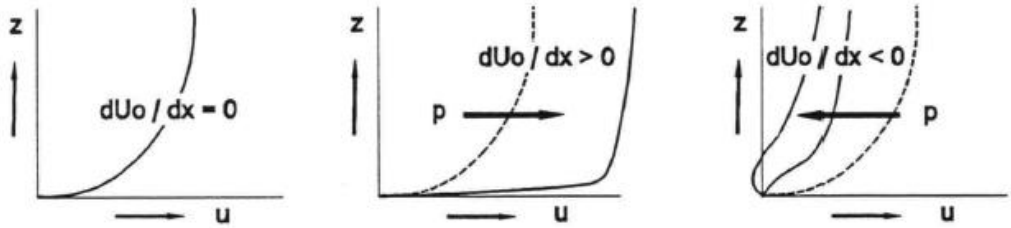

Figure B.2: Influence of pressure gradient on velocity profile (Schiereck, 2012)

B.1.3 Turbulence

The majority of the flows in nature, especially in hydraulic engineering for example the flow in rivers, channels and sea's, can be characterized as turbulent flow. Turbulent fluid motion is chaotic and fluctuates, whereas laminar flow is smooth and orderly. The Reynolds number gives the amount of turbulence. Turbulent fluid motion is an irregular motion in which the velocity and pressure show fluctuations. The velocity and the pressure can be written as follows:

$$u = \bar{u} + u' \qquad v = \bar{v} + v' \qquad w = \bar{w} + w' \qquad p = \bar{p} + p' \tag{B.4}$$

Turbulence can be expressed in various ways. Turbulent flow can be represented by the total kinetic energy (k) or by the relative fluctuation intensities (r) of u, v and w.

$$k = \frac{1}{2}(\overline{u'^2} + \overline{v'^2} + \overline{w'^2}) \tag{B.5}$$

$$r_u = \frac{\sqrt{\overline{u'^2}}}{\bar{u}} \qquad r_v = \frac{\sqrt{\overline{v'^2}}}{\bar{u}} \qquad r_w = \frac{\sqrt{\overline{w'^2}}}{\bar{u}} \tag{B.6}$$

For turbulent flow, the values of velocity and pressure can be split up in their time-average and fluctuation terms. The extra stress terms of the Reynolds-avearged Navier-Stokes (RANS) equations are the Reynolds stresses. These extra terms are given as (Pietrzak, 2017b):

Normal stresses: $\tau_{xx} = -\rho\overline{u'u'} \qquad \tau_{yy} = -\rho\overline{v'v'} \qquad \tau_{zz} = -\rho\overline{w'w'}$ (B.7)

Shear stresses: $\tau_{xy} = \tau_{yx} = -\rho\overline{u'v'} \qquad \tau_{xz} = \tau_{zx} = -\rho\overline{u'w'} \qquad \tau_{yz} = \tau_{yz} = -\rho\overline{v'w'}$ (B.8)

Turbulence will appear in flows were energy can be transferred from the mean motion to the turbulent fluctuations. The turbulent fluctuations are a result of velocity differences (velocity gradients), either between a flow and a wall (wall turbulence) or between two fluid bodies (free turbulence). Examples of wall turbulence are flows in open channels and pipes, whereas examples of free turbulence are jets, wakes, mixing layers in recirculation zones. Mixing layer and jet flow will be discussed hereafter. For more detail about turbulence, one is referred to Uijttewaal (2017).

B.1.4 Vertical and horizontal expansion

Figure B.3 shows the flow situation in a backward-facing step. One can observe uniform (wall) flow before the step, a free flow with a mixing layer immediately downstream of the step and eventually uniform wall flow with an increased depth. The depth increase will decelerate the flow, cause the flow to separate and result in the recirculation zone. Figure B.3 shows the deviations from hydrostatic pressure in the backward-facing step case. One can see the adverse pressure gradients as the result of the decelerated flow. These adverse pressure gradients cause flow separation.

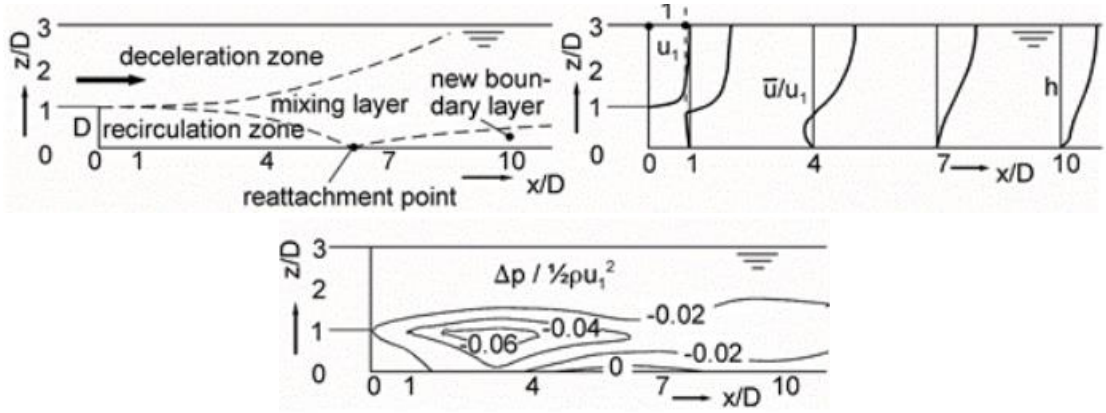

Figure B.3: Flow structure in backward-facing step (Schiereck, 2012)

Figure B.3 shows measurements of the flow structure around a sill. One observes a uniform flow (logarithmic velocity profile) before the sill, accelerating flow (rectangular velocity profile) on top of the sill, decelerating flow directly downstream and the recovery to a uniform flow (logarithmic velocity profile over the depth) downstream of the sill. There is no flow separation.

B.1.5 Free horizontal shear flows

Wakes, jets and mixing layers are the three important types of plane free shear flows (Van Prooijen, 2004). Free indicates that there is no influence of a wall and that turbulence arises from the mean-flow gradients (Van Prooijem 2004).

Figure B.4 presents some characteristics of a plane free jet flow. The jet can be divided into two distinct regions, the flow development region and the fully developed region. In the flow development region, the turbulence is penetrating inwards towards the centerline of the jet. There is a wedge-like region of undiminished mean velocity, equal to u_0. This wedge is also known as the potential core and it is surrounded by a free mixing layer on either side of the jet. Figure B.5 illustrates the flow-development region of plane free jets.

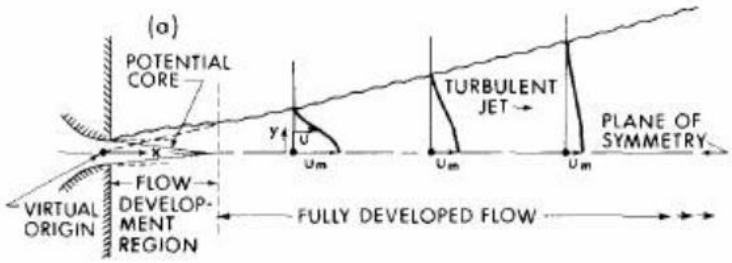

Figure B.4: Definition sketch of plane turbulent free jets (Rajaratnam, 1976)

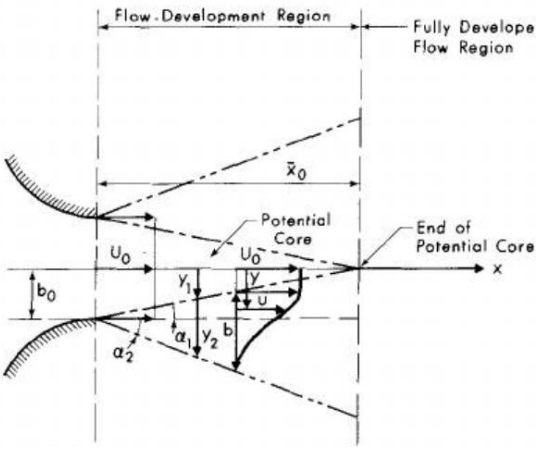

Figure B.5: Definition sketch of flow-development region of plane jets (Rajaratnam, 1976)

Where the two shear layers meet the potential core ends, the fully developed region starts (Cohen, 2012). After the flow has developed fully, the jet spreads and the velocity decreases. IFigure B.6 shows the flow and velocities in the jet in the fully developed region.

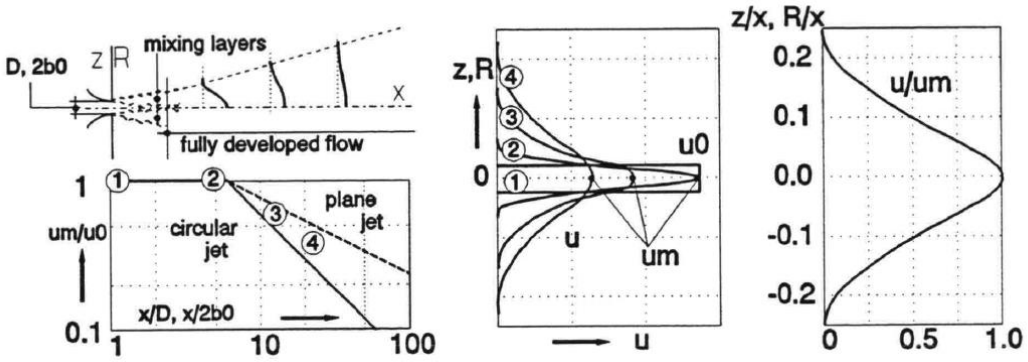

Figure B.6: Flow and velocities in jet (Schiereck, 2012)

A mixing layer or a free shear layer is a layer of flow where a gradient of shear or velocity exists. In case of two bodies of fluid move along each other with different velocities, a mixing layer will grow between them. The mixing layer growth is comparable with the growth of the boundary layer in wall flow. The fluid with high velocity will lose momentum, whereas fluid with low velocity (or stagnant fluid) will accelerate (exchange of momentum). Figure B.7 shows some characteristics of mixing layers. In the mixing layer the shear stress is intense, inducing turbulence (Schiereck, 2012).

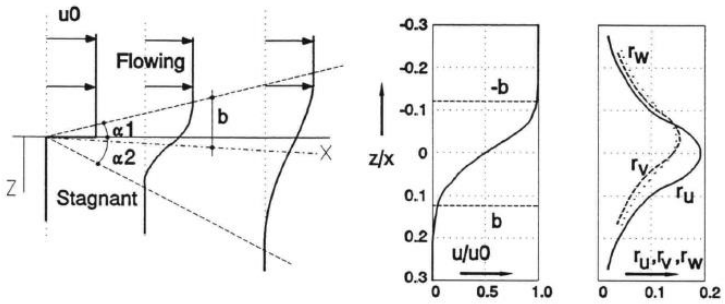

Figure B.7: Flow, velocities and turbulence in mixing layer (Schiereck, 2012)

B.1.6 Potential vorticity

The important features of flow with large lateral (y-direction) gradients experiencing a streamwise change in depth, the scour hole, may be understood through the conservation of potential vorticity. This appendix presents some information concerning potential vorticity. It is hypothesized that laterally nonuniform flow may contract in the horizontal plan by a streamwise depth increase through conservation of potential vorticity. This additional acceleration may on his turn suppress vertical flow separation on a steep downstream slope.

An expression for conservation of potential vorticity is shown in Equation (B.9):

$$\frac{D}{Dt}\left(\frac{\omega}{h}\right) = \frac{D}{Dt}\left(\Omega_p\right) = 0 \tag{B.9}$$

where: $\omega = vorticity[1/s]$

$h = height\ [m]$

$\Omega_p = scaled\ voriticty\ [-]$

Equation (B.9) shows that the ratio vorticity ω over the height (water depth) is conserved along a streamline. The vorticity ω is proportional to the water depth; when the depth increases, the vorticity increases. Figure B.8 shows the conservation of the potential vorticity. As the vertical fluid column moves from left to right, vertical stretching reduces the moment of inertia of column (causing it to spin faster) and reduces the diameter of the vortex tube (convergence of streamlines) (Pietrzak, 2017a).

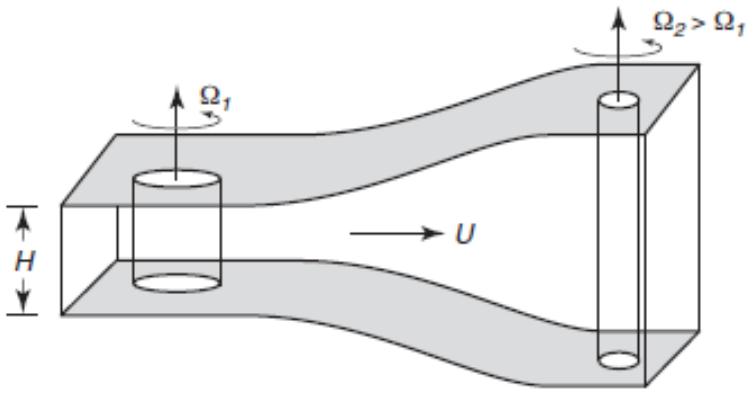

Figure B.8: Sketch of the production of vorticity (in this case defined as Ω) by changes in height of a fluid column (change in water depth) (Stewart, 2008)

B.2 Scour

B.2.1 Flow and turbulence coefficient

A value for the coefficient α depends on the definition of the flow velocity (Schiereck, 1996, p. 66). Figure B.9 illustrates the relation between the scour coefficient α and the geometry. For more information on the turbulence and flow coefficient α, the reader is referred to Jorissen & Vrijling (1989).

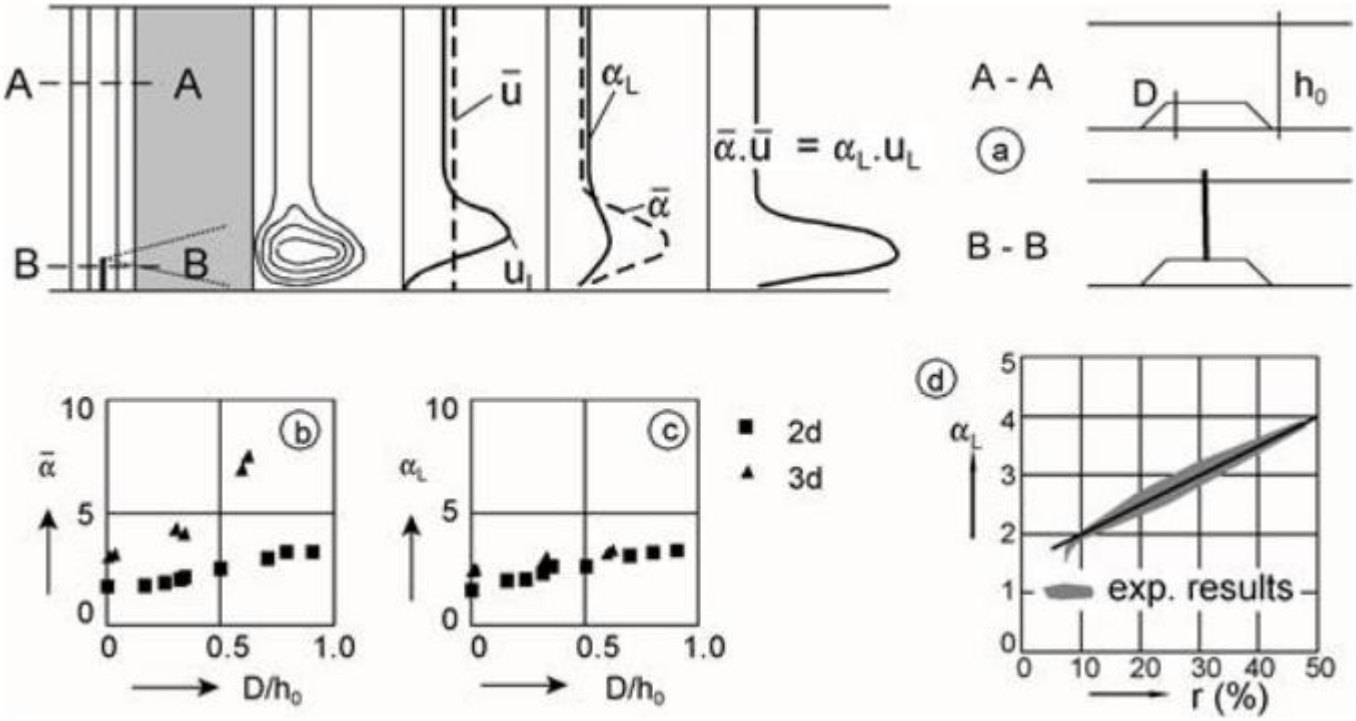

Figure B.9: Influence of definition of α on numerical values (Schiereck, 2012)

Figure B.9a shows the two ways to define the coefficient α and the flow velocity. The scour coefficient α can be linked with the mean velocity (averaged over the cross-section) $\bar{u} = Q/A$ or the coefficient α can be related to the local depth averaged velocity $\bar{u}_l$. When the flow velocity is defined as the mean velocity $\bar{u} = Q/A$, the coefficient α includes the velocity distribution. In the case the coefficient α is linked to the local depth averaged velocity, it represents only the magnifying factor due to turbulence. The product of the flow and turbulence coefficient and the mean velocity $(\alpha \cdot \bar{u})$ is the same as the product of the local flow and turbulence coefficient and the local depth averaged flow velocity $(\alpha_l \cdot \bar{u}_l)$.

Figure B.9b gives α as a function of the vertical constriction for two-dimensional scour and three-dimensional scour using the mean velocity $\bar{u} = Q/A$. One can see a significant difference in the value of α in three-dimensional scour. Figure B.9c gives α_l as a function of the vertical constriction by using the local depth averaged velocity. Figure B.9d illustrates the relation between local turbulence coefficient α_l and the turbulent fluctuations. Jorissen & Vrijling (1989) derived for hydraulic rough flow conditions the following expression:

$$\alpha_l = 1.5 + 5\, r_0 \tag{B.10}$$

where: $r_0 = relative\ depth - averaged\ turbulence\ intensity$

A more general relation for the local turbulence coefficient is given by Hoffmans & Booij (1993a) and it reads:

$$\alpha_l = 1.5 + 4.4\, r_0\, f_C; \tag{B.11}$$

where: $r_0 = relative\ turbulence\ intensity$

$f_C = friction\ coefficient;\ f_C = \dfrac{C}{40}$

The three-dimensional scour process can be determined at any cross-section, provided that the local turbulence coefficient α and the local depth-averaged velocity $\bar{\bar{u}}$ are known.

The scour process is determined on one hand by the flow characteristics and turbulence intensities and on the other hand by sediment characteristics (Hoffmans & Verheij, 1997). According to Breusers (1966, 1967), turbulence fully depends on the flow velocity and turbulence level at the transition between the fixed and the erodible bed. The flow and turbulence coefficient α is related to r_0 (relative turbulence coefficient) at the transition of the fixed to the erodible bed (Jorissen & Vrijling, 1989):

$$\alpha = 1.5 + 5\, r_0 \tag{B.12}$$

where: $r_0 = relative\ turbulence\ intensity$

The coefficient α is an amplification factor for the velocity, expressing the disturbance in the flow. The magnitude depends largely upon the upstream geometry, however the length and roughness of the bed protection downstream of the structure also play an important role (Hoffmans & Verheij, 1997). Equation A.20 and Figure B.10 show the influence of the length of the bed protection on α.

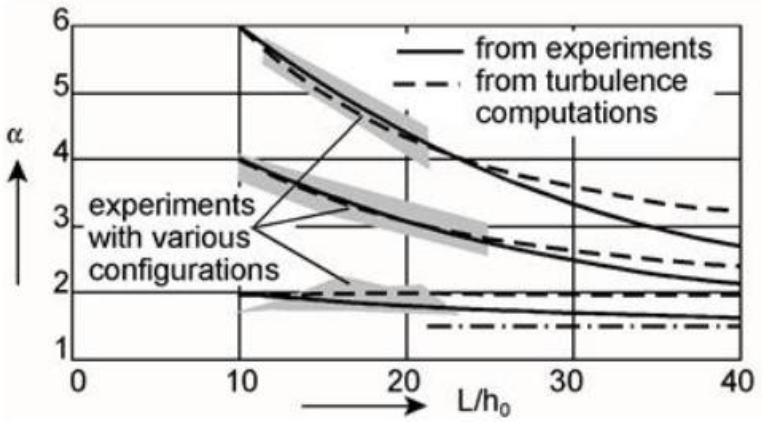

Figure B.10: Relation between α, turbulence and length of bed protection (Schiereck, 2012)

$$\alpha\,(L/h_0) = 1.5 + (1.57\alpha_{10} - 2.35)\,e^{(-0.0045\,L/h_0)} \tag{B.13}$$

where: $\alpha_{10} = \alpha$-value for L/h_0

$L = lenght\ of\ bed\ protection$

Equations A.21 and A.22 presents the relative turbulence intensities for respectively sills and jets (Hoffmans & Booij, 1993a).

Sills:

$$r_0 = \sqrt{0.0025\left(1 - \frac{D}{h_0}\right)^{-2}\left(\frac{L - 6D}{6.67\,h_0} + 1\right)^{-1.08} + 1.45\frac{g}{C^2}}\ for\ L > 6D \tag{B.14}$$

where: $C = Chezy\ coefficient\ related\ to\ bed\ protection\ [m^{1/2}/s]$

$D = height\ of\ sill\ [m]$

$g = acceleration\ of\ gravity\ [m/s^2]$

$L = length\ of\ bed\ protection\ [m]$

Jets:

$$r_0 = \sqrt{0.0025\left(\frac{b_u}{h_t}\right)^{-2}\left(\frac{L - 6(h_t - b_u)}{6.67\,h_t} + 1\right)^{-1.08} + 1.45\frac{g}{C^2}}\ for\ L > 6(h_t - b_u) \tag{B.15}$$

where: $b_u = thickness\ of\ jet\ at\ inflow\ [m]$

$C = Chezy\ coefficient\ related\ to\ bed\ protection\ [m^{1/2}/s]$

$h_t = tailwater\ depth\ [m]$

$L = length\ of\ the\ bed\ protection\ [m]$

Besides the maximum scour depth, the slope at the upstream end of the scouring hole is important for the stability of the structure and the bottom protection. In addition, empirical relations were found in order to predict the steepness of the upstream scour slope (Hoffmans, 1993):

$$\beta = sin^{-1}\left(2.9 \cdot 10^{-4} \cdot \frac{{U_0}^2}{\Delta g d_{50}} + (0.11 + 0.75 r_0) f_C\right) \tag{B.16}$$

where: $d_{50} = median\ grain\ diameter\ [m]$

$r_0 = relative\ turbulence\ intensity\ at\ the\ end\ of\ the\ protection\ [-]$

$U_0 = depth - averaged\ velocity\ at\ the\ end\ of\ the\ protection\ [m/s]$

This relation indicates that velocity, turbulence, a smooth bed protection and fine sand.

B.2.2 Non-steady flow

For a description of the scouring process many laboratory experiments have been performed. These tests generally considered steady flow. However, the scour pattern in practice is mainly caused by unsteady flow. In tidal areas, a scour hole will develop under tidal flow. The relationships that are valid for steady flow cannot simply be used. Some significant factors used in the calculations such as the flow velocity and the water depth are now a function of time. Therefore, the equations for steady flow conditions are extended to unsteady flow conditions. The reader is referred to for example Hoffmans & Verheij (1997) and De Graauw & Pilarczyk (1981) for more information about the scour under non-steady flow.

The calculation method for calculating the maximum scour depth can be adapted for unsteady flow conditions. The adjusted equations take into account the time-dependency of the flow velocity and the water depth and assume that the unsteady flow is a series of an infinite number of short-lasting steady situations. In situations where the equilibrium phase has not been reached, the maximum scour depth is given by Hoffmans & Verheij (1997):

$$\frac{y_m(t)}{h_0(0)} = \left(\frac{t}{t_{1,u}}\right)^{\gamma} \tag{B.17}$$

in which: $h_0(0) = tide - averaged\ flow\ depth\ [m]$

$t_{1,u} = characteritic\ time\ at\ which\ y_m = h_0(0)\ [s]$

Equation A.24 can be adjusted for tidal flow and the characteristic time can be represented by (Hoffmans & Verheij, 1997):

$$t_{1,u} = \frac{K \cdot h_0(0) \cdot \Delta^{1.7}}{\frac{1}{T}\int_{t_1}^{t_2} \frac{(\alpha \bar{u}_0(t) - \bar{u}_c)^{4.3}}{h_0(t)} \cdot dt} \tag{B.18}$$

in which: $T = t_2 - t_1, half\ tidal\ period\ where\ \alpha\bar{u}_0 > \bar{u}_c\ [s]$

$t_1 = time\ at\ which\ \alpha\bar{u}_0\ first\ exceeds\ \bar{u}_c\ during\ flood\ tide\ [s]$

$t_2 = time\ at\ which\ \alpha\bar{u}_0\ drops\ below\ \bar{u}_c\ during\ ebb\ tide\ [s]$

The scour process in tidal areas can be simulated reasonably with a characteristic constant mean velocity. When the mean velocity in a tidal area can be approximated by a sine function, the following relation is obtained for example by Hoffmans (1992):

$$\bar{u}_d = \eta \cdot \bar{u}_{m,t} \tag{B.19}$$

in which: $\bar{u}_d = characteristic\ mean\ velocity\ [m/s]$

$\bar{u}_{m,t} = maximum\ velocity\ during\ a\ tide\ [m/s]$

$\eta = 0.75 - 0.85\ [-]$

The characteristic time can then be approximated by (Hoffmans & Verheij, 1997):

$$t_{1,u} = \frac{K \cdot {h_0}^2(0) \cdot \Delta^{1.7}}{(\alpha \bar{u}_d - \bar{u}_c)^{4.3}} \qquad \text{(B.20)}$$

in which: $T = t_2 - t_1, half\ tidal\ period\ where\ \alpha\bar{u}_0 > \bar{u}_c\ [s]$

$t_1 = time\ at\ which\ \alpha\bar{u}_0\ first\ exceeds\ \bar{u}_c\ during\ flood\ tide\ [s]$

$t_2 = time\ at\ which\ \alpha\bar{u}_0\ drops\ below\ \bar{u}_c\ during\ ebb\ tide\ [s]$

B.2.3 Upstream supply of sediment

In practice, an upstream supply of sediment is often present. This influence of the upstream supply of sediment on the scour hole development can be taken into account with the additional computations as given here. The reader is referred to for example Hoffmans & Verheij (1997) for this approximate calculation method. The development of a scour hole is reduced in cases with an upstream supply, because the full transport capacity of the flow is not available for the transport of sediment from the scour hole. A part of the transport capacity of the flow is used to supply sediment from upstream. The volume of a scour hole can be given by (Hoffmans & Verheij, 1997):

$$V(t) = c_a \, {y_m}^2(t) \tag{B.21}$$

in which: $c_a = shape\ factor\ of\ scour\ hole\ [-]$

$V(t) = volume\ of\ scour\ hole\ per\ unit\ width\ [m^3/m]$

$y_m(t) = maximum\ scour\ depth\ [m]$

Mosonyi & Shoppmann (1968) reported different numerical values for the shape factor c_a. The volume of the reduced scour hole due to the upstream supply of sediment particles can be given by (Hoffmans & Verheij, 1997):

$$V_r(t) = V(t) - q_s t \tag{B.22}$$

in which: $V_r(t) = reduced\ volume\ of\ the\ scour\ hole\ per\ unit\ widht\ [m^3/m]$

$q_s = reduction\ transport\ per\ unit\ with\ (including\ porosity)\ [m^2/s]$

$t = time\ [s]$

The reduced maximum scour depth as function of time taking into account the upstream supply of sediment is given by Konter & van der Meulen (1986) and it reads (see also Figure B.11):

$$\frac{{y_{m,p}}^2\left(t_p + \Delta t_p\right) - {y_{m,p}}^2\left(t_p\right)}{\Delta t_p} = \frac{{y_{m,c}}^2\left(t_c + \Delta t_c\right) - {y_{m,c}}^2\left(t_c\right)}{\Delta t_c} - \frac{q_s}{c_a} \tag{B.23}$$

in which: $t_c = time\ referring\ to\ conditions\ where\ q_s = 0\ [s]$

$t_p = time\ referring\ to\ live\ bed\ conditions\ [s]$

$\Delta t = time\ step\ [s]$

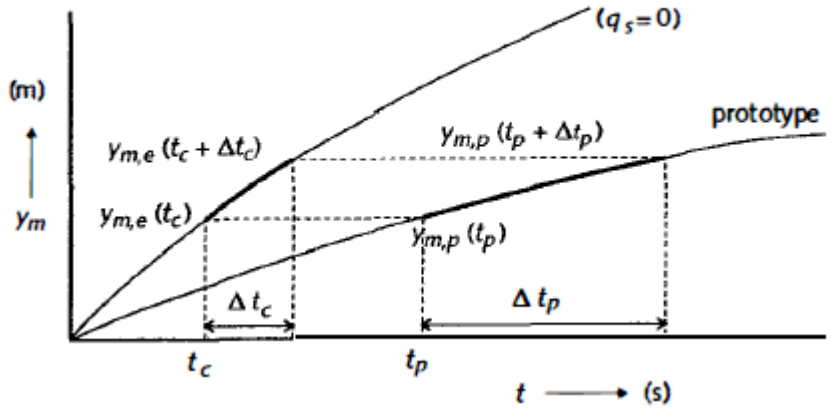

Figure B.11: Reduction method (Hoffmans & Verheij, 1997)

C Experimental setup

This appendix discusses and illustrates the experimental setup in more detail.

Figure C.1: Flow straightener

Figure C.3: Testing the flume

Figure C.2: The plates with roughness (glued gravel)

Figure C.4:Sieve at the end to collect the eroded sand

Figure C.5: The inlet section with asymmetrical pump and several meshes to smoothen the flow

Figure C.6: The inflow section partially blocked with brick elements in order to have lateral velocity differences. The floating foam boards to suppress the surface waves.

D Results

This appendix presents additional results of the experiments. First, the scour results under lateral uniform and non-uniform flow will be given.

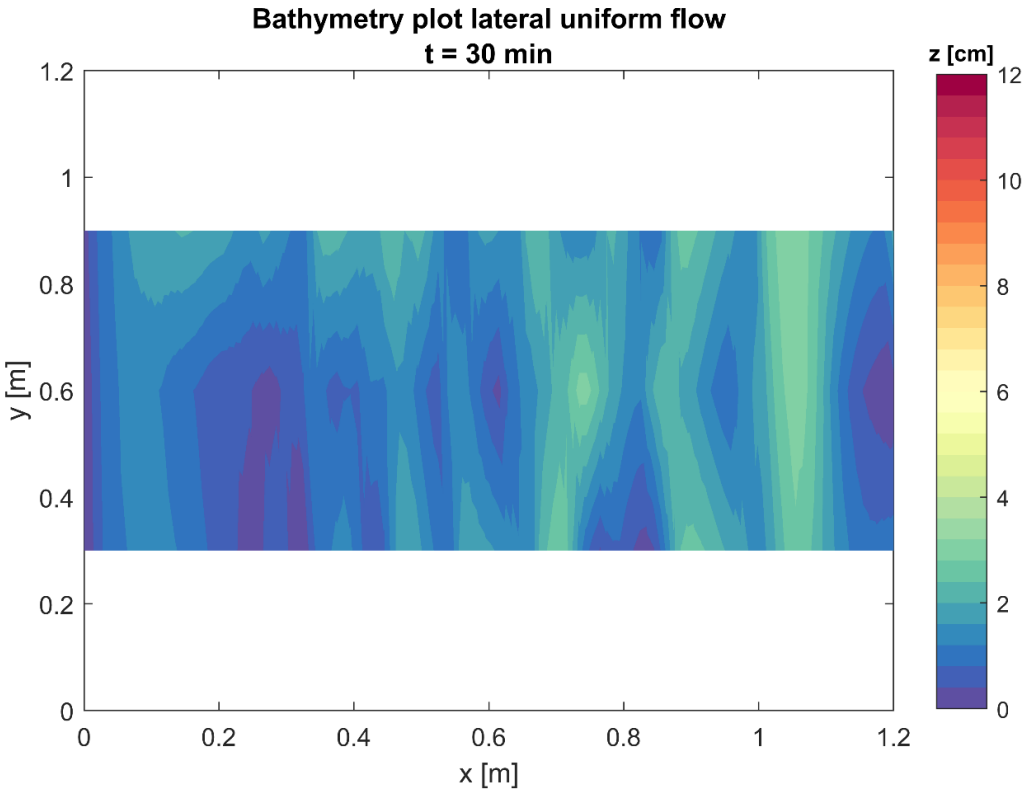

Figure D.1: Scour under lateral uniform flow $t = 30\ min$

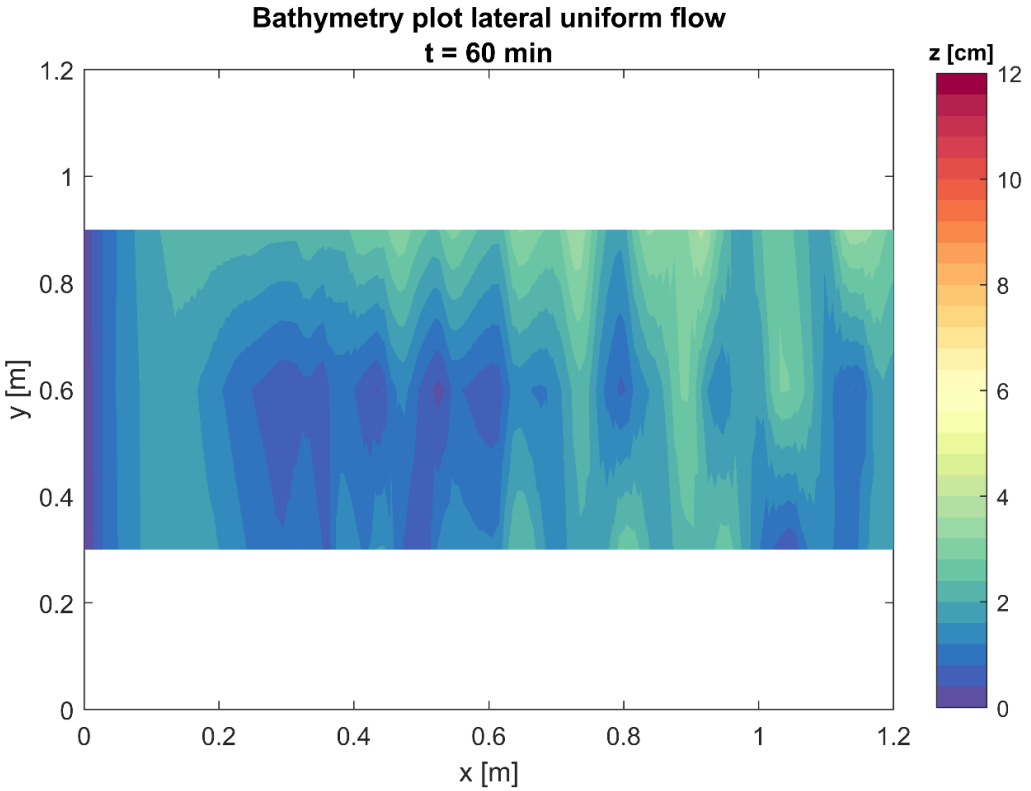

Figure D.2: Scour under lateral uniform flow $t = 60\,min$

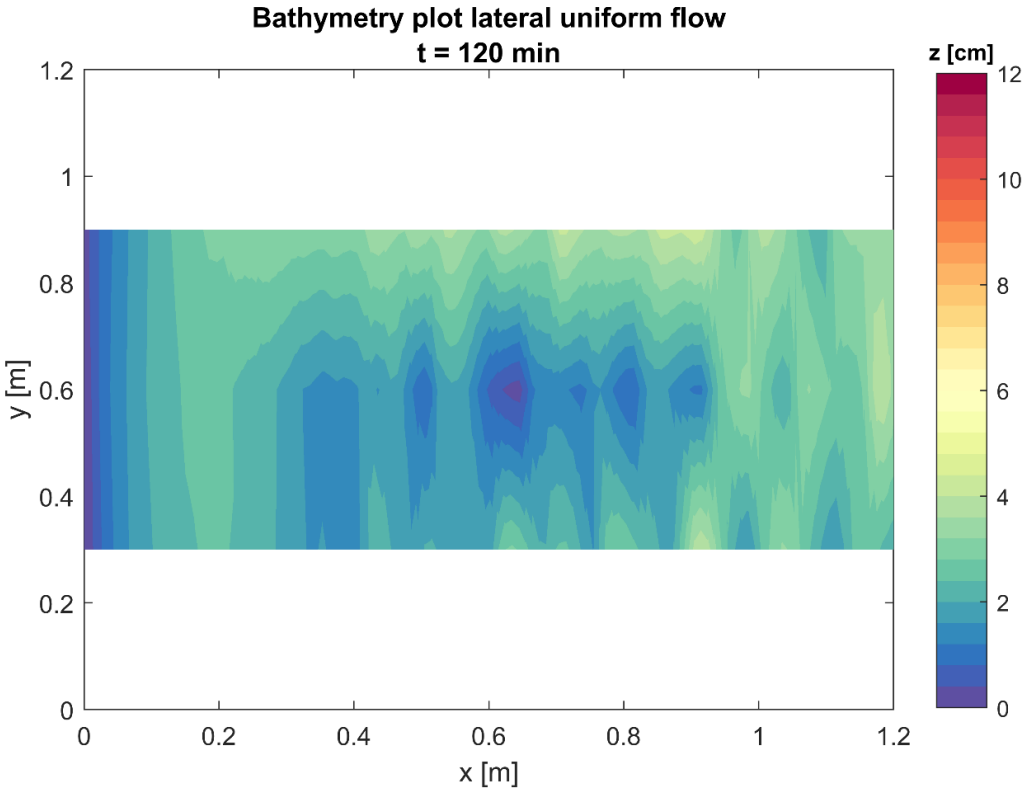

Figure D.3: Scour under lateral uniform flow $t = 120\,min$

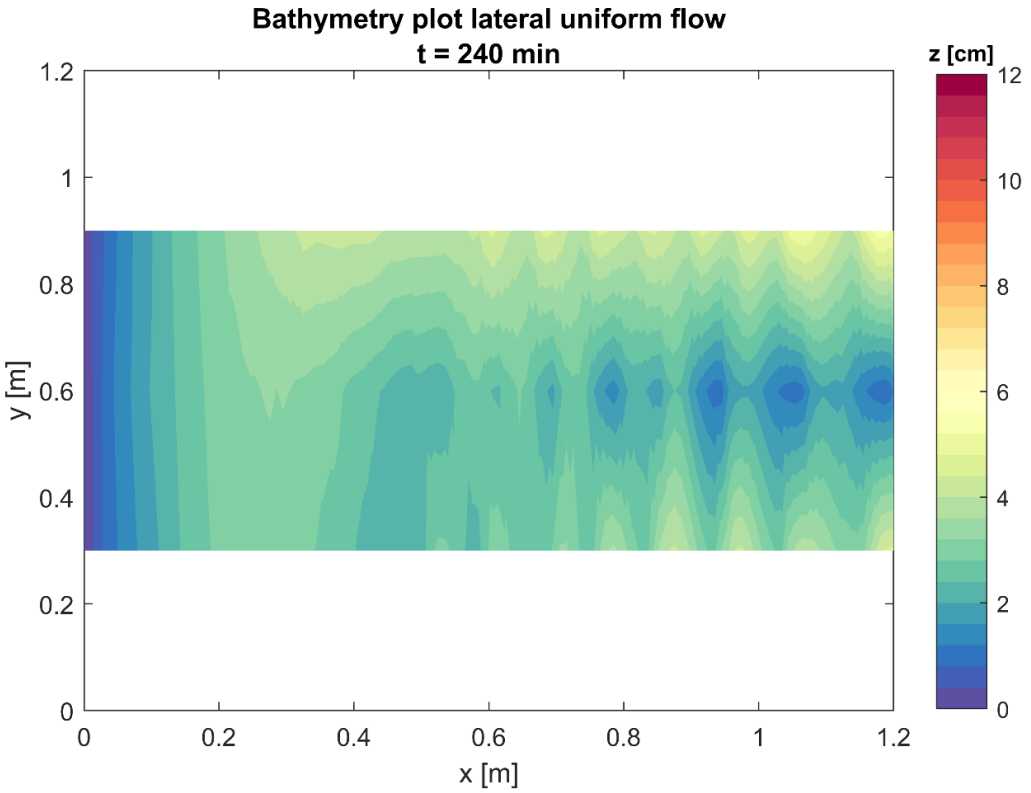

Figure D.4: Scour under lateral uniform flow $t = 240\,min$

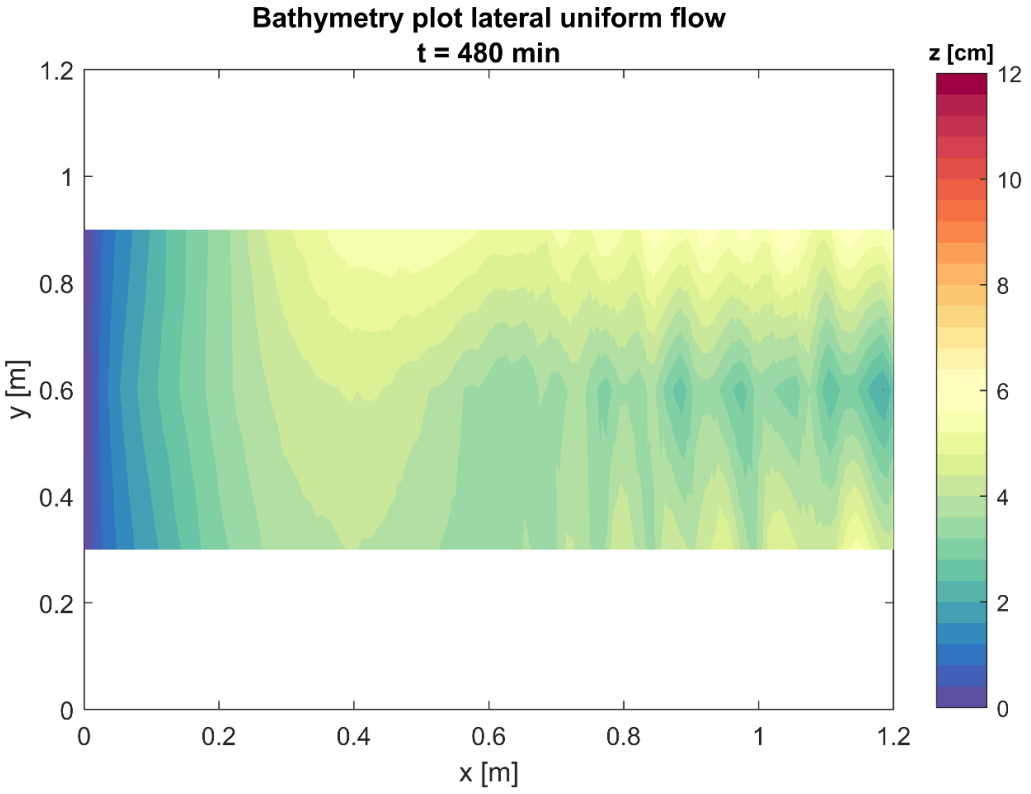

Figure D.5: Scour under lateral uniform flow t= $480\,min$

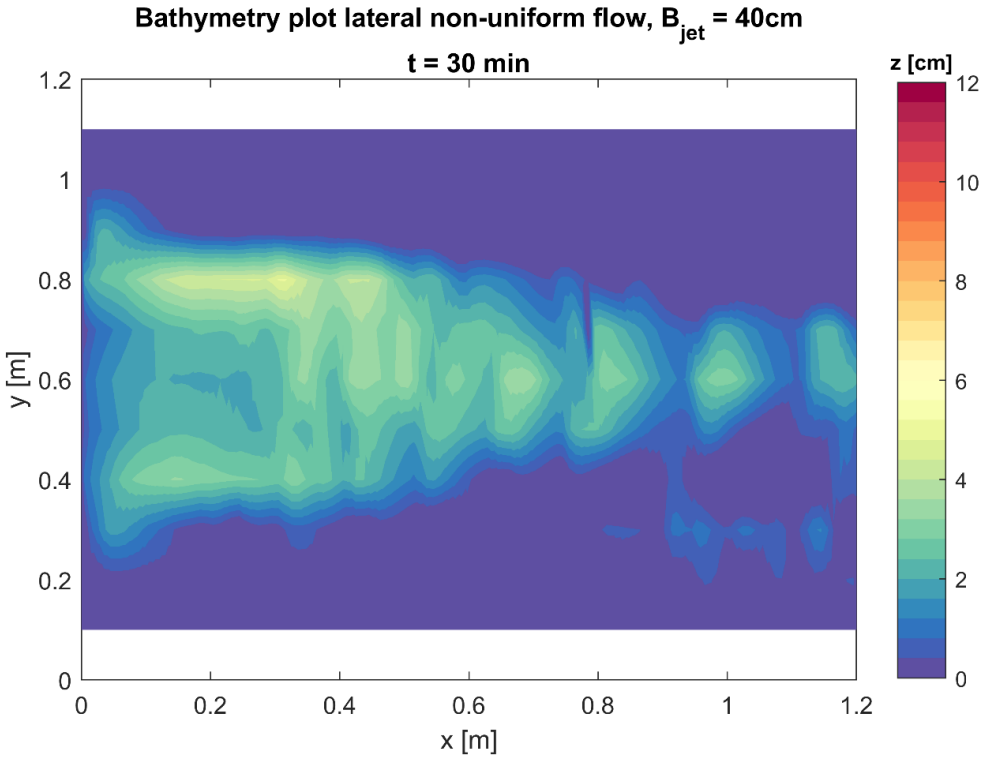

Figure D.6: Scour under lateral non-uniform flow $B_{jet} = 40\ cm$ for $t = 30\ min$

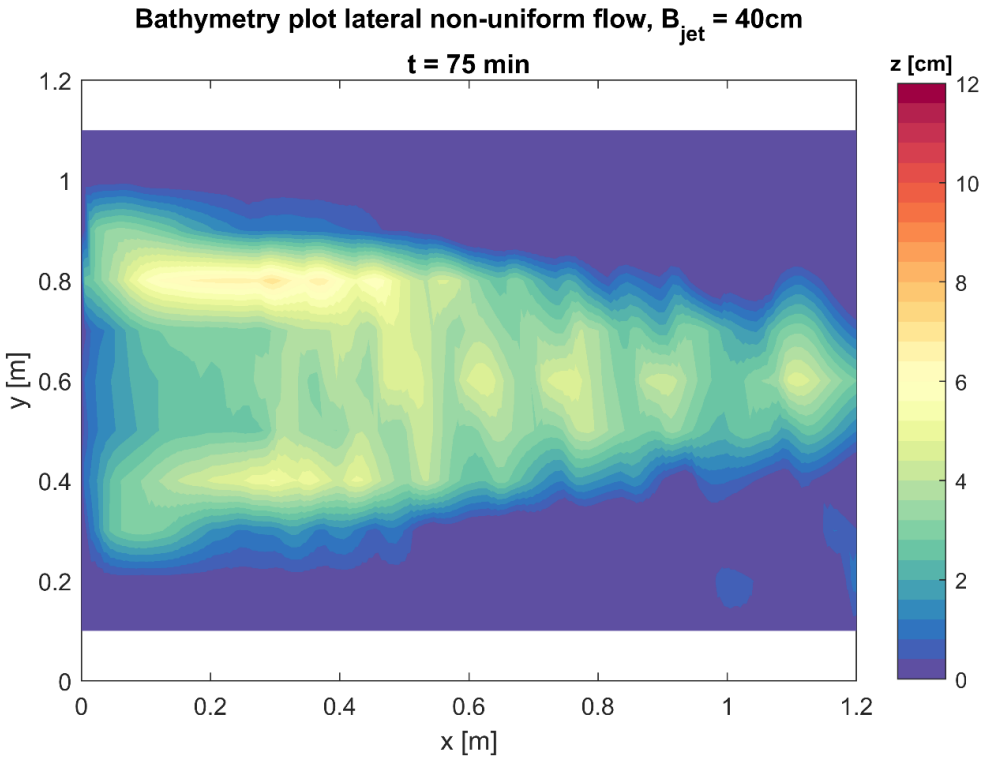

Figure D.7: Scour under lateral non-uniform flow $B_{jet} = 40\ cm$ for $t = 75\ min$

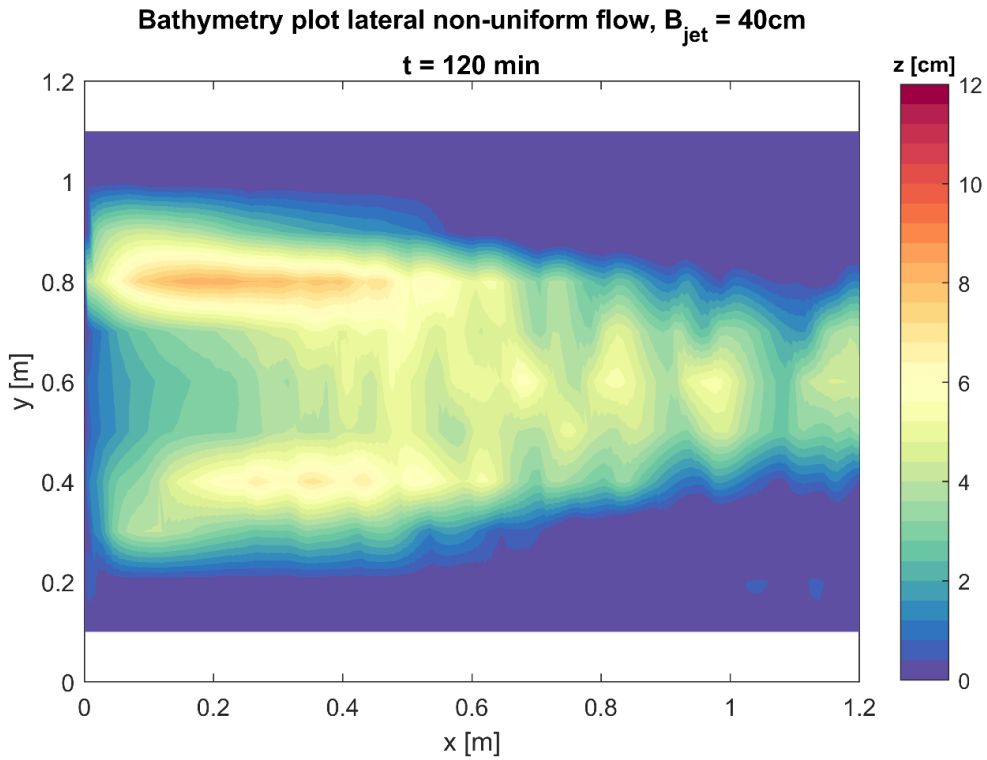

Figure D.8: Scour under lateral non-uniform flow $B_{jet} = 40\ cm$ for $t = 120\ min$

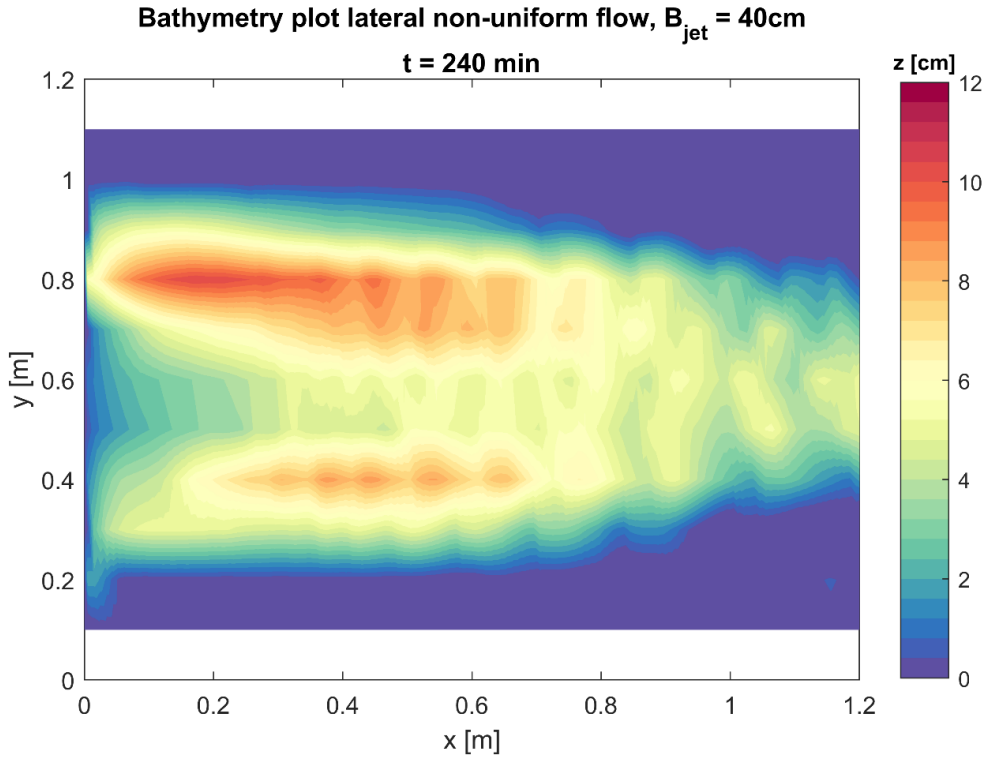

Figure D.9: Scour under lateral non-uniform flow $B_{jet} = 40\ cm$ for $t = 240\ min$

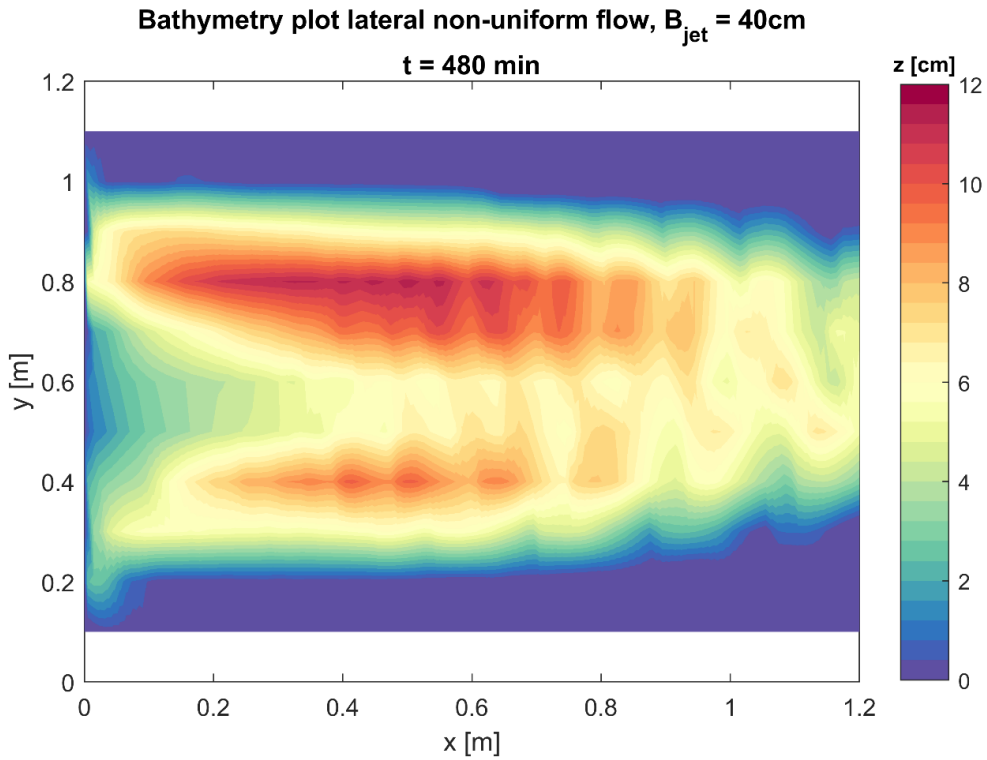

Figure D.10: Scour under lateral non-uniform flow $B_{jet} = 40\ cm$ for $t = 480\ min$

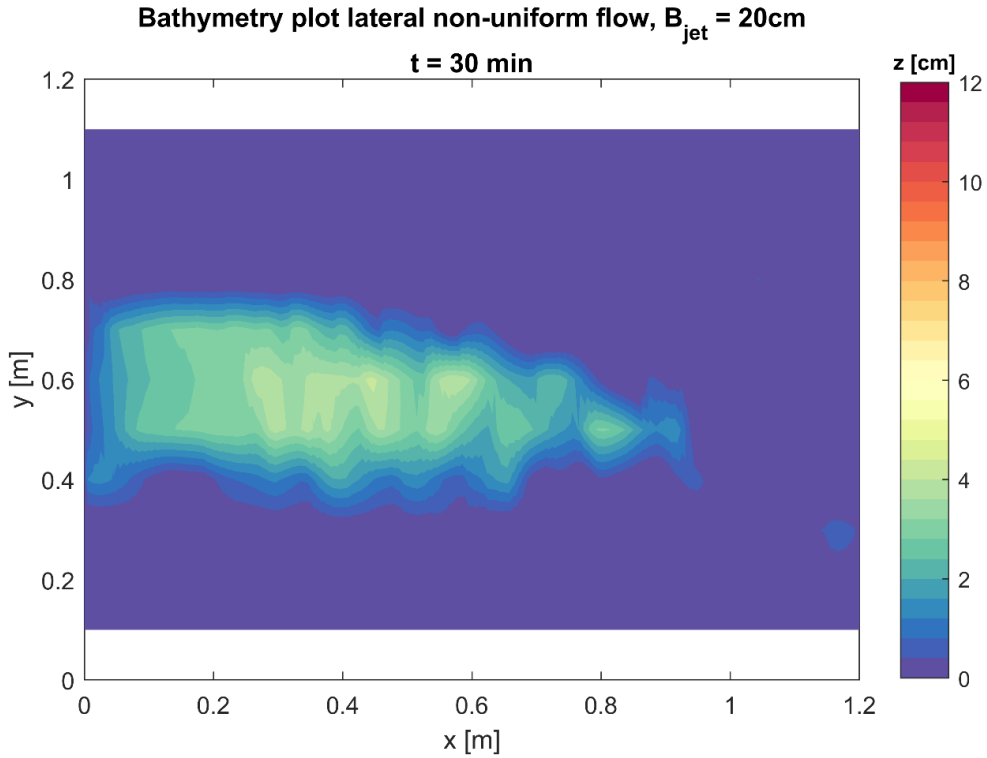

Figure D.11: Scour under lateral non-uniform flow $B_{jet} = 20\ cm$ for $t = 30\ min$

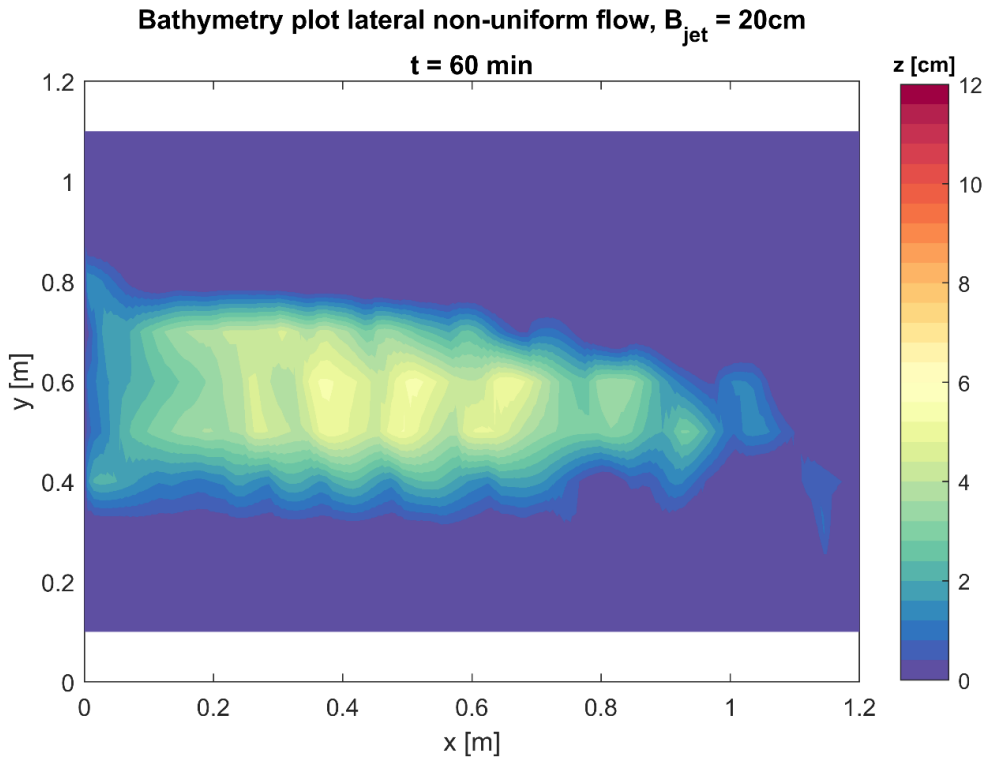

Figure D.12: Scour under lateral non-uniform flow $B_{jet} = 20\ cm$ for $t = 60\ min$

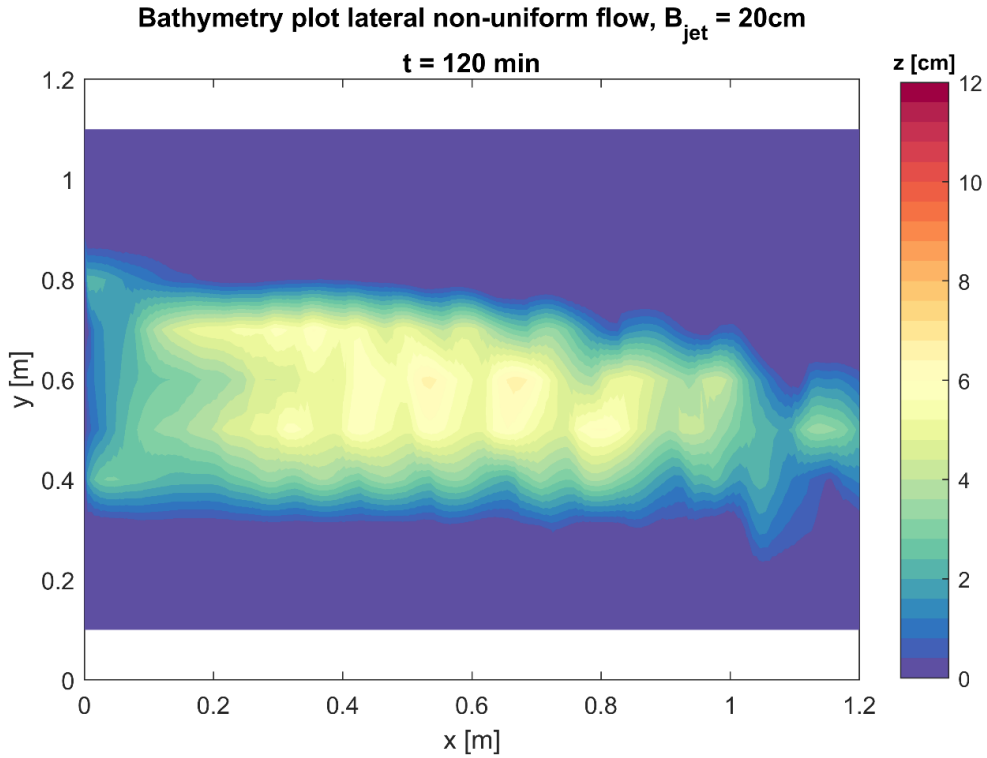

Figure D.13: Scour under lateral non-uniform flow $B_{jet} = 20\ cm$ for $t = 120\ min$

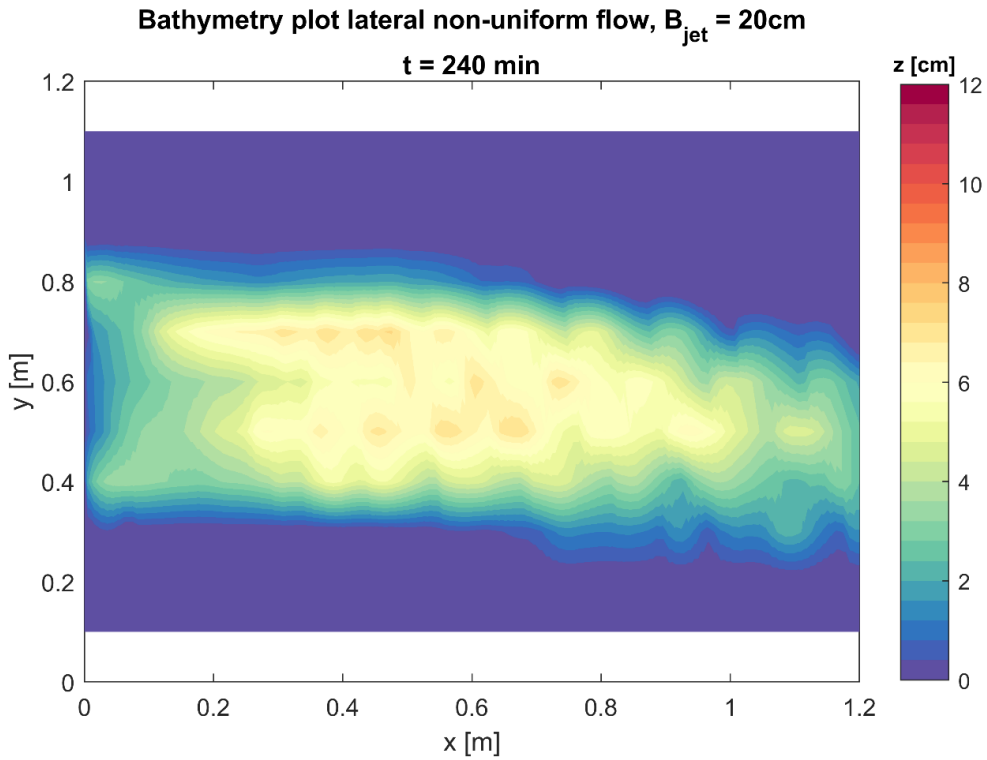

Figure D.14: Scour under lateral non-uniform flow $B_{jet} = 20\ cm$ for $t = 240\ min$

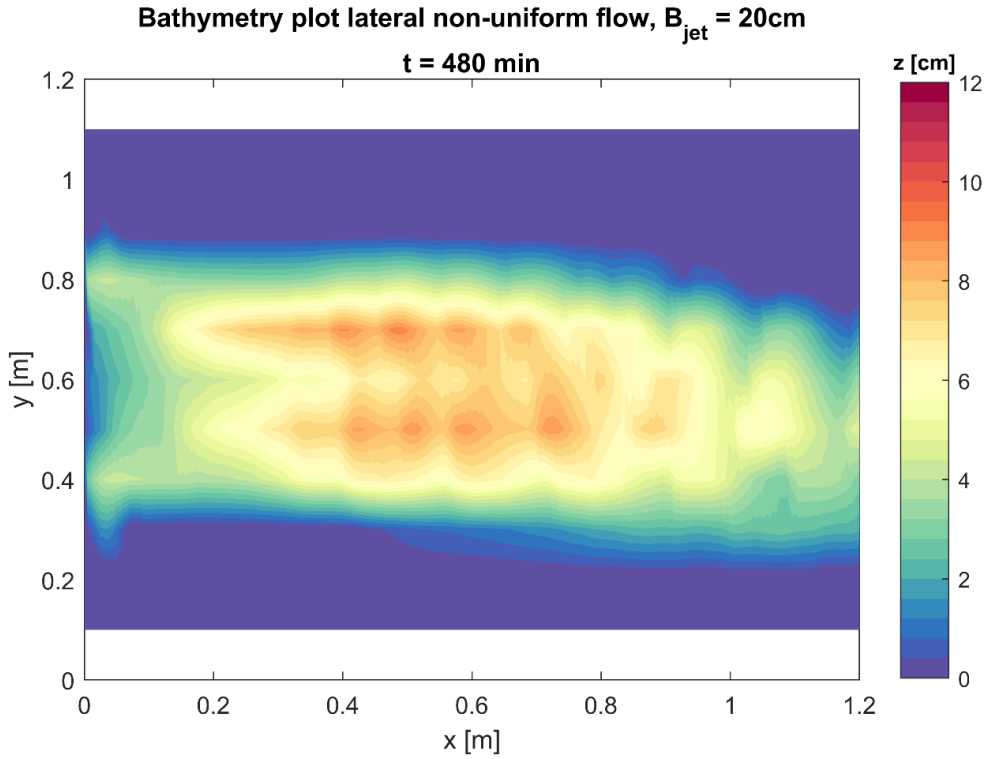

Figure D.15: Scour under lateral non-uniform flow $B_{jet} = 20\ cm$ for $t = 480\ min$